

MODIFICATION OF OPTICAL AND STRUCTURAL PROPERTIES OF GLASS CONTAINING SILVER NANOPARTICLES VIA DC ELECTRIC FIELD AND MODERATELY ELEVATED TEMPERATURES

Dissertation

zur Erlangung des akademischen Grades
doktor rerum naturalium (Dr. rer. nat.)



vorgelegt der

Mathematisch-Naturwissenschaftlich-Technischen Fakultät
(mathematisch-naturwissenschaftlicher Bereich)
der Martin-Luther-Universität Halle-Wittenberg

von

Amin Abdolvand
geb. am 14. April 1973 in Shiraz, Iran

Gutachter:

1. Professor Dr. Heinrich Graener (Martin-Luther-Universität Halle Wittenberg)
2. Professor Dr. Ralf Wehrspohn (Universität Paderborn)
3. Professor Dr. Anatoly V. Zayats (The Queen's University of Belfast, United Kingdom)

verteidigt am 12.01.2006

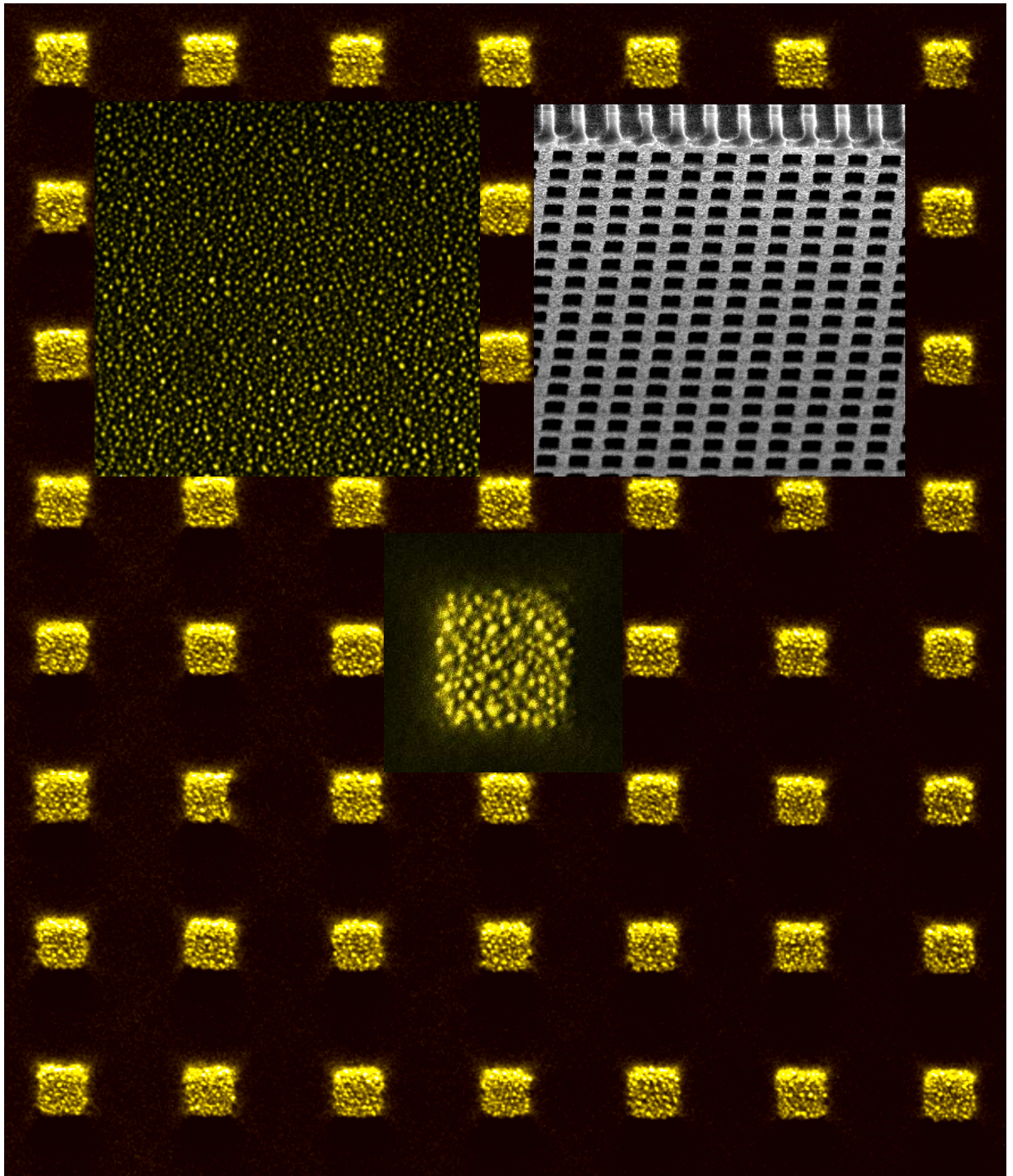
urn:nbn:de:gbv:3-000009671

[<http://nbn-resolving.de/urn/resolver.pl?urn=nbn%3Ade%3Agbv%3A3-000009671>]

Table of Contents

<u>Contents...</u>	<u>ii</u>
<u>1 Introduction and general aims...</u>	<u>1-3</u>
<u>2 Metals & metal-doped nanocomposite dielectrics...</u>	<u>4-15</u>
2.1 Introduction	4
2.2 Optical properties of Metals	4
2.2.1 Basics of interaction of light with metals...	4
2.2.2 Implications of Lorentz and Drude theories for metals...	5
2.2.3 Dispersion in metals...	7
2.2.4 Absorption, reflection and transmission of metals...	8
2.3 Metal-doped nanocomposite dielectrics	9
2.3.1 Surface plasmon resonance of metal nanoparticles...	11
2.4 Summary	15
<u>3 Glass containing embedded silver nanoparticles: Preparation, Characterization and Properties...</u>	<u>16-25</u>
3.1 Introduction	16
3.2 Brief review of the characterization tools	16
3.2 Preparation and characterisation of glass containing silver nanoparticles	17
3.2.1 Polydisperse samples...	18
3.2.2 Monodisperse samples...	21
3.3 Spectral properties	22
3.4 Summary	25
<u>4 DC electric field-assisted dissolution of silver nanoparticles in glass matrix: Observations & Processes...</u>	<u>26-43</u>
4.1 Observations	<u>26-35</u>
4.1.1 Introduction...	26
4.1.2 Experiments and results...	26
4.1.2.1 EFAD of silver nanoparticles in polydisperse-type II sample...	29
4.1.2.2 EFAD of silver nanoparticles in polydisperse-type I sample...	31
4.1.3 Synopsis of the observations...	33
4.2 Processes	<u>36-42</u>
4.2.1 Introduction...	36
4.2.2 Experimental...	36
4.2.3 Results and Evolution of EFAD...	37
4.3 Summary	<u>43</u>

<u>5 DC electric field-assisted formations of percolated silver anolayers inside glass: Observations & Characterizations...</u>	<u>44-62</u>
5.1: Observations	<u>44-51</u>
5.1.1 Introduction...	44
5.1.2 Experimental...	44
5.1.3 Results and synopsis of the observations...	44
5.2: Characterizations	<u>52-58</u>
5.2.1 Introduction...	52
5.2.2 Model...	52
5.2.3 Characterization of the large coloured areas...	53
5.2.4 Characterization of the border region...	57
5.3 Discussion	59
5.4 Summary	61
<u>6 Metallodielectric 2D structures made by DC electric field assisted microstructuring of nanocomposite glasses...</u>	<u>63-73</u>
6.1 Introduction	63
6.2 Experimental	64
6.3 Results and discussion	65
6.4 Summary	73
7 Conclusions and Future Directions...	74-77
References...	78-85
Appendices...	86-101
<u>A: Thermal poling of glass: a brief introduction</u>	<u>86</u>
<u>B: On the evolution of EFAD</u>	<u>93</u>
<u>C: Curriculum Vitae</u>	<u>95</u>
<u>D: List of publications and contributions</u>	<u>96</u>
<u>E: Acknowledgements</u>	<u>100</u>
<u>F: Erklärung</u>	<u>101</u>



Nanocomposite glasses containing silver nanoparticles can be microstructured by application of DC electric field and moderately elevated temperatures. This is based on the newly discovered phenomenon of field-assisted dissolution of metal nanoparticles embedded in glass. In chapters 4 and 5 of the thesis the physical interpretation of the dissolution phenomenon is presented. Afterwards, in chapter 6, it is shown that any pattern of the electrode – down to the nanoscale – can be transferred into the nanocomposite glass giving 2D metallodielectric microstructures.

The presented image here shows as background a regular array of squares with $2\mu\text{m}$ periodicity, which was produced using macroporous silicon as an electrode. The insets represent the base material (top left), electrode (top right), and an enlarged view of one of the structures showing the remaining silver nanoparticles.

Chapter 1: Introduction and general aims

Glasses and other dielectrics containing metal nanoparticles are very promising materials for photonics applications owing to their unique linear and nonlinear optical properties. These properties are dominated by the strong surface plasmon resonances (SPRs) of the metal nanoparticles. Surface plasmons (SPs) are waves that propagate along the surface of a conductor, usually metals due to their large but negative dielectric constant.* SPs are essentially light waves that are trapped on the surface because of their interaction with the free electrons of the conductor. In this interaction, the free electrons respond collectively by oscillating in resonance with the light wave. The spectral position of the SPRs in the compound materials can be designed within a wide spectral range covering the visible and near-infrared spectra by choice of the electronic properties of the metal and the dielectric matrix [1.1,1.2], or by manipulation of size [1.3], shape [1.4], and spatial distribution [1.5] of the metal clusters. This makes the compound materials very promising candidates for some applications in the field of photonics [1.6-1.8]. One of the main issues in this context is to structure the optical properties of such materials on a micro-, or even submicron scale. This aspect, in fact, occupies many researchers within the scientific community. The scientific interest covers from the study of optical subwavelength structures such as plasmonic waveguides based on metal nanoparticles [1.9, 1.10] to the much larger scale, micrometer scale, where the compound materials are appropriate for production of a number of standard and advanced optical elements such as: gratings, segmented filters, polarizers, etc.

One of the examples of a prototype of the compound materials, which in fact is the one used here, is a glass containing embedded spherical silver (Ag) nanoparticles of 30-40nm mean diameter prepared by Ag^+ - Na^+ ion exchange [1.11,1.12]. In this particular case the originally spherical silver nanoparticles can via a microscopic thermomechanical deformation process, be transformed into uniformly oriented ellipsoidal ones [1.20], accompanied by the formation of a strongly dichroitic optical extinction [1.13], which makes these materials well suitable as polarizers [1.21].

The interaction of laser beam with these materials has extensively been studied in the past. It has already shown that the interaction of ultrashort laser pulses with silver

* A medium with large but negative dielectric constant ϵ is a good host for surface plasmons. Most common metals such as Au, Ag and Al can exhibit resonant absorption by surface plasmon excitation, since in an isotropic medium having refractive index n and absorption k where $\epsilon = (n+ik)^2$, whenever $k \gg n$ the criterion of large but negative ϵ is satisfied.

nanoparticles in glass can lead to shape modification of the particles, depending on the polarization state of the laser beam. This was macroscopically observed as optical dichroism [1.8, 1.14-1.16]. As a particular example the work published by M. Kaempfe *et al.* [1.14] can be mentioned where a glass sample containing spherical silver nanoparticles was irradiated by intense femtosecond laser pulses. The irradiation resulted in permanent colour changes when the laser wavelength was in the region of the particles surface plasmon resonance.

In fact the main stream of interest in study of interaction of laser light with composite glasses is due to their spectral properties. It is not difficult to understand if one recalls that spectral, and hence optical properties of metal-doped composite glass is strongly depend on the volume filling factor of the metallic inclusions. This aspect is detailed in the following chapters, where it will be shown that the collective dipolar interactions between silver nanoparticles embedded in glass could cause a significant broadening and red shift of the absorption band as a result of increase in filling factor of the silver inclusions. Given a feature as such no one can fail to turn his thoughts towards exciting particles located in regions with different metal fill factor in composite glass using a laser with appropriate wavelength. An example of this approach can be found in our recent work [1.17].

Although in the past laser-based techniques proved to provide a flexible tool for structuring of the optical properties of these materials there are a number of short comings related to these techniques where one can not only rely on them. First of all these techniques are often costly. They require demanding maintenance and this could hamper mass production of many useful optical elements based on the nanocomposite glasses. The other short coming is the fundamental one. To the best of the author's knowledge in contrast to the supported nanoparticles, which can be selectively evaporated from the substrate surface directly by the absorbed laser energy [1.18, 1.19], glasses with embedded metal particles can not be made transparent by laser irradiation. This could put an upper limit on structural abilities of laser-based techniques.

Another alternative way for controlled nanodesign of metal nanoparticles is via electron beam lithography [1.22]. Although by this technique size and shape of the nanoparticles can be designed and nanoparticles can be arranged and oriented in any required pattern, the nanofabrication process itself is highly demanding and costly.

This thesis presents the results of an investigation into a new, physically very interesting and technologically simple, approach to structure optical properties of composite glass containing silver nanoparticles: applying a combination of an intense direct current (DC) electric field and moderately elevated temperatures, the particles can be destroyed and dissolved in the glass matrix in the form of silver ions, leaving a transparent area. This leads to a promising application of this technique, which is the bleaching of the optical absorption band that is associated with the surface plasmon resonance of silver in glass host. Throughout the thesis it will be shown that the underlying physical mechanism of this phenomenon is potentially promising for the control of structural and optical properties of silver-doped nanocomposite glasses.

In this thesis, for the sake of compactness, comprehensive reviews of optical properties of metals as well as metal clusters are intentionally avoided. Thus, next

chapter of the thesis (chapter 2) will only briefly review some of these properties. Also throughout the thesis, wherever it was required, the necessary background is provided. Excellent reviews of optical properties of nanostructured random media can be found in references 1.1 and 1.2.

Chapter 3 presents preparation technique as well as characterisation of silver-doped nanocomposite glasses which were used for the research as samples. This chapter also provides some valuable information and theoretical background on spectral properties of these materials.

The introduced phenomenon here is believed to be of general interest in the physics of nanocomposite materials. Given that chapter 4 is devoted to detail description of spatial features and dynamics of evolution of the DC electric field assisted bleaching of soda-lime glasses containing embedded spherical as well as elongated silver nanoparticles, with two different distribution profiles of the nanoparticles. This chapter provides the key information on the physical processes leading to the electric field-assisted dissolution (EFAD) of silver nanoparticles.

The fifth chapter is then report on DC electric field-assisted formation of percolated silver nanolayers inside the glass with embedded spherical silver nanoparticles. In this chapter the ability of the EFAD technique for gaining control over spatial distribution of the metallic inclusions is explored. A successful modelling of the results is also presented.

Afterwards chapter 6 will present results on production of optical structures in the glass containing silver nanoparticles using the EFAD technique. It is shown that this simple technique is capable of producing fine, micron as well as submicron size, embedded 2-D structures in the nanocomposite materials.

Chapter 7 then draws the thesis to its conclusions by giving a summary of the main achievements and by offering some suggestions as to possible future work.

Chapter 2: Metals and metal-doped nanocomposite dielectrics

2.1 Introduction

In this chapter the background to the optical properties of metals as well as dielectrics containing metallic nanoparticles are briefly discussed. It gives definitions of the terms used in the thesis and presents the basic theory.

It is, thus, divided into two main sections. Section 2.2 deals with the optical properties of metals and briefly discusses important subjects such as dispersion in metals and reflection from metals. Section 2.3 then describes some details of optical linear as well as nonlinear properties of metallic nanoparticles. In this section the important subject of interaction of ultrashort laser pulses with a dielectric containing metallic nanoparticles is also briefly touched. The chapter concludes with a short section on what was described here.

2.2 Optical properties of metals

The characteristic feature of a conducting media is the presence of free electric charges. For metals these charges are electrons, which motion constitutes a current.

The current per unit area resulting from the application of a field \vec{E} is related by means of the *Ohm's Law* to the conductivity of the medium σ . For a dielectric there are no free or conduction electrons and thus $\sigma=0$. However, for metals σ is nonzero and finite. In fact in real metals the conduction electrons undergo collisions with the thermally agitated lattice or with imperfections and in so doing irreversibly convert electromagnetic energy into joule heat. (Absorption of radiant energy by any material is a function of its conductivity.)

2.2.1 Basics of interaction of light with metals

Interaction between light and metals takes place between the optical electric field and the conduction band electrons of the metals. Some of the light energy can be transferred to the lattice in the form of heat via collisions. Hence, the optical properties of metals can be characterized by two optical constants: refractive index, n , and extinction coefficient, k , that result in the complex refractive index, \tilde{n} , where:

$$\tilde{n} = n + ik . \quad (2.1)$$

The refractive index is defined as the ratio of phase velocity of light in vacuum to the phase velocity of light in the given medium. The extinction coefficient is related to the exponential decay of the wave as it passes through the medium. Both of the constants vary with wavelength and temperature [2.1].

Hence, the expression for an electromagnetic wave in an absorbing medium contains both of these parameters and can be expressed as follow:

$$E = E_0 e^{-2\pi kx/\lambda_0} e^{-i(2\pi x/\lambda_0 - \omega t)} \quad (2.2)$$

where E_0 is the amplitude of the wave measured at the point $x=0$ in the medium, E is the instantaneous value of the electric vector measured at a distance x from the first point and at some time t , ω is the angular frequency of the source, and λ_0 is the wavelength in vacuum.

The absorption coefficient is related to the extinction coefficient by:

$$\alpha = 4k/\lambda_0 \quad (2.3)$$

The absorption coefficient also appears in the absorption equation in the following form (Beer's equation):

$$I = I_0 e^{-\alpha x} \quad (2.4)$$

where I_0 is the irradiance at $x=0$ (that is the interface). Thus the flux density will drop by a factor of e^{-1} after the wave has propagated a distance $y = 1/\alpha$, which is known as the penetration depth. For a transparent material the penetration depth is larger than its thickness. However, the penetration depth for metals is very small. For instance copper has a penetration depth of only 6nm for the light at 10 μ m and that drops to the penetration depth of only 0.6nm for ultraviolet light at 100nm [1.1]. (It has to be pointed out that the equation (2.4) implies that the intensities I and I_0 are measured within the absorbing medium.)

The complex dielectric constant ϵ_i for metals is given by:

$$\epsilon_i = \epsilon' + i\epsilon'' \quad (2.5)$$

where the dielectric constants are related to the optical constants by:

$$\epsilon' = n^2 - k^2 \quad (2.6a)$$

$$\epsilon'' = 2nk \quad (2.6b)$$

2.2.2 Implications of Lorentz and Drude theories for metals

The classical theory of absorption in dielectrics is due to H. A. Lorentz [2.55] and in metals to P. K. L. Drude [2.56]. Both models treat the optically active electrons in a material as classical oscillators. In the Lorentz model the electron is considered to be bound to the nucleus by a harmonic restoring force, just as for the nonconductive

dielectric. Drude, however, considered the electrons to be free, and thus set the restoring force in the Lorentz model to be zero. Both models include a damping term in the electron's equation of motion. (In a more modern view this term is recognized to be the result of electron-phonon collisions.)

The Lorentz model for dielectrics gives the relative real and imaginary parts of the dielectric constant, ϵ' , and ϵ'' , in terms of N , the number of dipoles per unit volume; e (in some text books shown as q_e - This form is adapted later on here) and m , the electron charge and mass; Γ (in some text books shown as γ - This form adapted later on here.), the damping constant; ω and ω_0 , the radian frequencies of the field and the harmonically bound electron; and ϵ_0 , the permittivity of free space. The results of the Lorentz theory are graphically shown in Fig. 2.1. The range of frequencies where ϵ' increases with frequency is referred to as the range of normal dispersion, and the region near $\omega = \omega_0$ where it decreases with frequency is called the range of anomalous dispersion.

In the Lorentz model for dielectrics, as far as the ionic polarizability is much smaller than the electronic polarizability at optical frequencies, only the electronic terms are considered when evaluating optical absorption.

The Drude model for metals assumes, however, that the electrons are free to move. This means that it is identical to the Lorentz model except that ω_0 is set equal to zero. The real and imaginary parts of the dielectric constant are then given by:

$$\epsilon' = 1 - (Nq_e^2 \epsilon_0 m) \frac{1}{\omega^2 + \Gamma^2}, \quad (2.7)$$

$$\epsilon'' = (Nq_e^2 \epsilon_0 m) \frac{\Gamma}{\omega(\omega^2 + \Gamma^2)}. \quad (2.8)$$

The quantity Γ is related to the mean time between electron collisions with lattice vibrations. At low electromagnetic field frequencies, it can be shown that $\epsilon_{2R} \gg \epsilon_{1R}$ and therefore one has [2.1]:

$$\alpha = (\omega \mu \sigma / 2)^{\frac{1}{2}}, \quad (2.9)$$

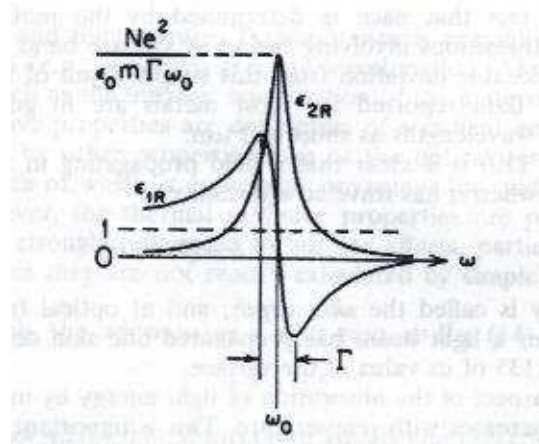


Figure 2.1: Frequency dependence of ϵ' and ϵ'' . The graph is adapted from [2.57]. ϵ' and ϵ'' are shown in the graph with indices 1R and 2R, respectively.

where μ is the magnetic susceptibility. Therefore, the optical properties and the conductivity of a perfect metal are related through the fact that each is determined by the motion of free electrons. At high frequencies, transitions involving bound or valence band electrons are possible and there will be a noticeable deviation from the simple result of the Drude model.

According to the Drude model only the plasma frequency (see section 2.2.3) should dictate the appearance of metals. This approach works for many metals, e.g. Zinc, however it does not explain why gold is yellow, copper is red and silver is colorless. These metals are known as the “Noble Metals”.

Gold, silver and copper all have filled d-shells and possess the electronic configuration of $[\text{Xe}].4f^{14}.5d^{10}.6s^1$, $[\text{Kr}].4d^{10}.5s^1$ and $[\text{Ar}].3d^{10}.4s^1$, respectively. The calculated values of plasma frequency for all three lie at about 9eV. This value is well outside the visible region, whereas, for instance, the reflectance spectrum of silver shows a drop at about 4eV (Fig. 2.2), well below the expected plasma frequency. In fact its reflectance rises again for frequencies just above 4eV. This behavior is because silver has a d-band resonance at about 4eV.

The d-electron bands lie below the Fermi energy of the conduction band. Thus transition from the d-band (with energy E_d) to the empty states above the Fermi level (with energy E_F) can occur over a narrow band of energies, namely $E_F - E_d$. Therefore it turns out that the reflectance properties of noble metals are influenced by the combined effects of the free electrons (Drude model) and the bound d-electrons (Lorentz model).

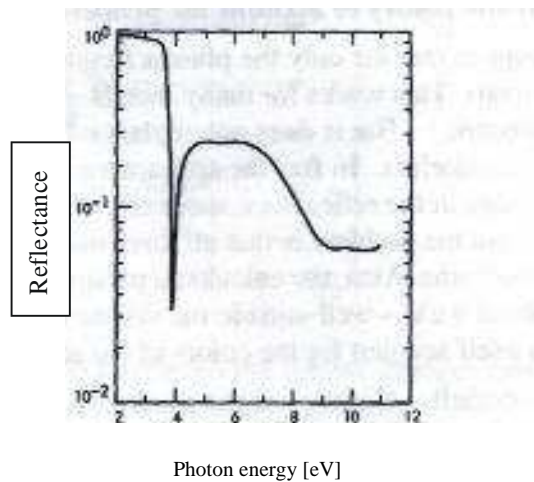


Figure 2.2: Reflectance versus photon energy for silver. The graph is adapted from [2.58].

It is customary to consider the effect of free-electrons via Drude model and the bound d-electrons via Lorentz model. It has to be pointed out that Drude theory of optical properties of metals is only an extension of the Lorentz model to metals, where the electrons are free (unbound), and hence they experience zero restoring force [2.51]. The Drude model will extensively be used throughout the thesis for review of spectral properties of embedded metallic nanoparticles in glass.

2.2.3 Dispersion in metals

In the previous sections it was discussed that the conduction electrons are the predominant contributors to the optical properties of metals. If a metal has a particular color, it indicates that the atoms are partaking of selective absorption by way of the bound electrons, in addition to the general absorption characteristic of the free electrons. A medium that is very strongly absorbing at a given frequency does

not actually absorb much of the incident light at that frequency but rather selectively reflects it.

Free electrons and positive ions within a metal can be considered as plasma whose density oscillates at a natural frequency of ω_p , known as the *free electron plasma frequency* given by [2.1]:

$$\omega_p = \left(\frac{Nq_e^2}{m\epsilon_0} \right)^{1/2}, \quad (2.10)$$

where N is the density of free electrons, m is the effective mass of an electron and ϵ_0 is the electric permeability of vacuum. Thus, the dispersion equation for metals can be expressed as [2.1]:

$$n^2(\omega) = 1 - (\omega_p / \omega)^2. \quad (2.11)$$

From 2.11, it can be seen that plasma frequency serves as a critical value below which the index is complex and the penetrating wave drops off exponentially from the boundary. However, at frequencies above the plasma frequency the n is real, and hence the absorption is small and the conductor is transparent. The refractive index for metals is complex and the propagating wave will suffer absorption in an amount that is frequency dependent.

2.2.4 Absorption, reflection and transmission of metals

From equation (2.9), it is evident that a field propagating in a metal will be attenuated by a factor of $1/e$ when it has traveled the penetration depth, y :

$$y = (2/\omega\mu\sigma)^{1/2}. \quad (2.12)$$

After a light beam has propagated one penetration depth into a metal, its intensity is reduced to 0.135 of its value at the surface. For most metals, all the light that gets into the metal is absorbed

Absorption of light energy by metals increases with temperature. For instance, during laser irradiation the absorption of metal increases due to the increase of temperature. If the Fresnel expression for the electric field reflectance is applied to the real and imaginary parts of the complex index for a metal-air interface, the field reflectivity can be obtained and from that the following expression for the intensity reflection coefficient can be driven [2.1]:

$$R_I = 1 - 2\mu\epsilon_0\omega/\sigma. \quad (2.13)$$

From this expression can be seen that since the conductivity σ decreases with increasing temperature, R_I decreases with increasing temperature, and at high temperatures more of the incident energy is absorbed.

The ratio of radiant flux reflected from a surface to the total incident radiant flux is called the reflectance r . Since r is a function of the optical constants, it varies with wavelength and temperature. The relationship between reflectance and optical constant is [2.1]:

$$r = \frac{(n-1)^2 + k^2}{(n+1)^2 + k^2}. \quad (2.14)$$

The reflectance is normally less than unity as far as some transmission and absorption are always present. The relationship between these three properties is:

$$r + t + a = 1. \quad (2.15)$$

Transmittance t is the ratio of radiant flux transmitted through a surface to the total incident radiant flux and absorptance a is the ratio of the radiant flux lost by absorption to the total incident radiant flux. Since both t and a are functions of the optical constants, hence vary with wavelength and temperature.

For opaque materials, the transmission is near zero and Eq. (2.15) takes the following form:

$$r + a = 1. \quad (2.16)$$

2.3 Metal-doped nanocomposite dielectrics

Nanoparticles in general exhibit a wide range of electrical and optical properties due to the quantum size effect and the surface effect of the nanostructures. In this context, materials doped with noble metal nanoparticles exhibit a large third-order nonlinear susceptibility and an ultrafast nonlinear response. Thus these materials, for example, are considered to be very promising for ultrafast all-optical switches in the terahertz region [2.2].

As early as in 1950s surface plasmons (SPs) associated with metals became widely recognized in the field of surface science [2.3], and since then are of interest to a very wide spectrum of scientists. So far, many studies were carried out on the fabrication of nanoparticles doped materials [2.4-2.7] as well as spatial and size distribution control of noble metal nanoparticles in dielectric matrices [2.8, 2.9] and also their interaction with laser pulses [2.10-2.15]. The surface enhanced optical processes is the very reason why the existence of metallic structures much smaller than the wavelength of light are vital for the massive signal enhancement achieved in surface-enhanced Raman spectroscopy (SERS)-a technique that can now detect a single molecule [2.22, 2.23]. The enhanced field associated with SPs makes them also suitable for sensors [2.24]. Enhanced local electromagnetic fields have a strong impact on higher harmonic generation of metal nanoparticles [2.48].

In literature for second and third harmonic generation (SHG and THG) measurements from metal nanoparticles the surface plasmon resonances (SPs) were always identified as the source of large optical nonlinear susceptibility enhancement [2.18, 2.19, 2.49]. Lamprecht *et. al.* measured the decay time of the electron-plasma

oscillation of silver nanoparticles, at a film consisting of regularly arranged, identically shaped and identically oriented particles [2.60]. Researchers found that by design of a nanocentrosymmetric particle shape, SHG in transmission at normal incidence of the fundamental beam can be obtained. Studies of SHG of metal nanoparticles have a relatively long tradition in our group. For instance Podlipensky *et. al.* have recently observed resonant second-order susceptibility (χ^2) in a thin layers of ellipsoidal silver nanoparticles embedded in glass upon femtosecond laser irradiation at 800nm [2.20, 2.21].

Another important topic in the context of optical properties of metal-doped nanocomposite material is their interaction with ultrashort laser pulses. Laser induced breakdown and damage in materials, particularly transparent materials, have been studied since the advent of high-power pulsed laser sources [2.33]. With the advent of femtosecond lasers study of ultrashort laser pulses with various materials became of great interest. This is due to the following distinct features of the femtosecond lasers as compared to CW and long-pulsed lasers:

- (1) Elimination of the thermal effect because of the very short interaction time (energy deposition time)
- (2) Participation of various nonlinear processes which made possible by high localization of photons not only in time domain but also in spatial domain.

Owing to the ultrashort light-matter interaction time and the high peak power offered by femtosecond lasers, material processing with these lasers generally characterized by an absent of heat diffusion, and hence, of molten layer [2.34]. Due to the nature of the ultrashort light-matter interaction, femtosecond lasers are capable of overcoming the diffraction limit [2.35, 2.50]. Femtosecond lasers are frequently used for production of three-dimensional microscopic modifications of transparent materials [2.36-2.44].

Studies of interaction of ultrashort laser pulses with dielectrics containing metallic nanoparticles have been extensively carried out in our group. Recently, it was discovered that a permanent transformation of initially spherical metal nanoparticles embedded in soda-lime glass into ellipsoidal (more general, non-spherical) shapes can be made by irradiation with intense fs laser pulses [2.10-2.13].

In order to determine the laser energy deposition in such systems one needs to consider theoretical model which describes thermoionic and photoelectric effects in the metallic inclusions, due to the strong electron excitation in the ultrashort regime [2.45]. At short time scales and intensities offered by fs lasers, a strong injection of electrons by metal nanoparticles in the surrounding dielectric matrix is inevitable, and this leads to the creation of plasma around the inclusions, and thus to an increase in the optical absorption of the medium. A great deal of information on the physical mechanism behind the deformation and destruction of nanoparticles as a result of laser irradiation as well as details on interaction of fs and ns laser pulses with metal-doped nanocomposite dielectrics can be found in Ref. 2.46 and 2.47.

2.3.1 Surface plasmon resonance of metal nanoparticles

Propagation of an electromagnetic wave in a medium containing spherical metallic nanoparticles would cause displacement of conduction electrons relative to the positively charged ionic cores. This in turn results in dipole oscillating with the same frequency as of the incident wave. If radiuses of the nanoparticles are much smaller than the wavelength of the incident wave, the electrostatic approximation is valid and the dipole moment of the nanoparticles can be given by [2.52]:

$$\vec{P}(\omega) = \alpha \epsilon_0 \vec{E}_0(\omega) = 4\pi \epsilon_0 R^3 \frac{\epsilon_i(\omega) - \epsilon_h}{\epsilon_i(\omega) + 2\epsilon_h} \vec{E}_0(\omega), \quad (2.17)$$

where α is the polarisability of the sphere, R is the radius of the nanoparticle, E_0 is the strength of the incident wave, ϵ_0 is the electric permittivity of vacuum, $\epsilon_i(\omega)$ is the relative complex electric permittivity of metal and ϵ_h is the relative complex electric permittivity of the host matrix.

Absorption cross section of a spherical metal inclusion placed in a transparent dielectric matrix, where the imaginary part of the relative complex electric permittivity approaches zero ($Im[\epsilon_h] \rightarrow 0$) is then given as:

$$\sigma(\omega) = 12\pi R^3 \frac{\omega \sqrt{\epsilon_h}}{c} \frac{\epsilon_i''(\omega)}{[\epsilon_i'(\omega) + 2\epsilon_h]^2 + \epsilon_i''(\omega)^2}, \quad (2.18)$$

where $\epsilon_i'(\omega)$ and $\epsilon_i''(\omega)$ are real and imaginary parts of electric permittivity of the metal, respectively, and can be described via the Drude-Sommerfeld formula as follows:

$$\epsilon_i(\omega) = \epsilon_b + 1 - \frac{\omega_p^2}{\omega^2 + i\gamma\omega}, \quad (2.19)$$

where ϵ_b is the complex electric permittivity associated with inter-band transitions of the core electrons in atom, ω_p is the free electron plasma frequency and γ is a damping constant of the electron oscillations.

As it was briefly discussed earlier, for the Noble Metals the calculated value for plasma frequency is about 9eV. However, each of the Noble Metals has its specific surface plasmon (SP) absorption band. For instance, silver nanoparticles embedded in glass matrix exhibit SP band at about 417nm, as can be seen from the extinction spectra presented in Fig. 2.3. As it can be seen, SP for Au and Cu nanoparticles is shifted in red spectral range and peaked at 528nm and 570nm, respectively. The broad absorption bands below 500nm for both Au and Cu containing nanocomposite glasses are associated with interband transitions, namely from d- to s-shell, of the core electrons in the metal atoms. However, for silver the interband resonance is peaked at 310nm (4eV) far way from the SP resonance [59].

This can be explained if one recalls that the well known Mie resonance should occur at a given surface plasmon frequency, ω_{SP} , if the following condition in the Eq. 2.18 is fulfilled:

$$[\epsilon'_i(\omega_{SP}) + 2\epsilon_h]^2 + \epsilon''_i(\omega_{SP})^2 \rightarrow Min. \quad (2.20)$$

If for the imaginary part of the metal electric permittivity, $\epsilon''_i(\omega_{SP})$, one has the following condition fulfilled: $\epsilon''_i(\omega_{SP}) < \epsilon'_i(\omega_{SP})$; or it has small frequency dependence, Eq. 2.20 gives:

$$\epsilon'_i(\omega_{SP}) = -2\epsilon_h. \quad (2.21)$$

If this condition complies, the dipole moment and local field in the vicinity of a given metallic nanosphere will grow resonantly to values that overcome the field of the incident wave by many orders of magnitudes. This phenomenon is responsible for the surface plasmon enhanced nonlinearity of the metal colloids, as was briefly discussed.

Thus, using Eq. 2.21 and by substituting for $\epsilon'_i(\omega_{SP})$ from Eq. 2.19, position of the SP resonance can be expressed as follows:

$$\omega_{SP}^2 = \frac{\omega_p^2}{\text{Re}(\epsilon_b) + 1 + 2\epsilon_h} - \gamma^2. \quad (2.22)$$

As it can be clearly seen, the core electrons have a significant influence on the surface plasmon and obviously define position of the SP resonance in the extinction spectra of a given noble metal particle. Equation 2.22 also qualitatively describes the dependence of the SP resonance on the dielectric properties of the host matrix; in fact, increase in the dielectric constant (refractive index) of the matrix causes red shift of the absorption maximum [2.16, 2.53]. This can be seen in Fig. 2.4.

This Fig. also shows that the position of the SP resonance also depends on the radius of the metallic nanoparticles. In fact, its position remains quasi-constant for the nanoparticles with radius smaller than 15nm, while the band halfwidth for these clusters differs by the factor of 4. On the other hand, for nanoparticles with radius larger than 15nm, red shift of the SP resonance occurs. According to the mean free-path model [2.16], this behaviour of the SP resonance maximum can be explained by an influence of the cluster radius on the damping constant and consequently on the electric permittivity of the metal inclusions (Eq. 2.19). (This aspect was used in chapter 4, where evolution of electric-field-assisted dissolution of silver -

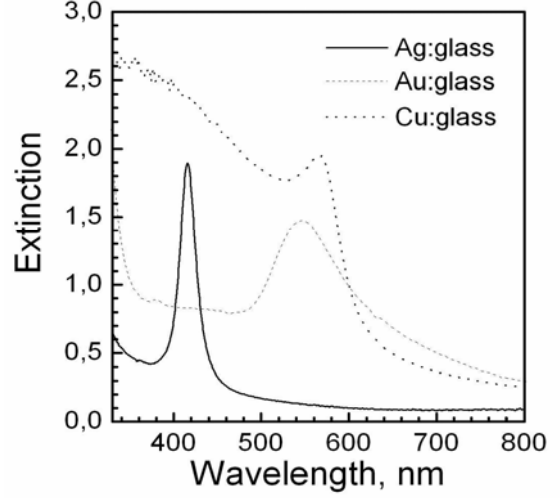


Figure 2.3: Extinction spectra of glasses containing spherical silver, gold and copper nanoparticles.

nanoparticles is considered, in order to achieve better theoretical fittings to the measured extinction spectra.)

Metal nanoparticles with nonspherical shape show several SP resonances in their absorption spectra. For example, ellipsoidal clusters with axis $a \neq b \neq c$ exhibit three SP modes corresponding to polarizabilities along principal axes given as [2.16]:

$$\alpha_k(\omega) = \frac{4\pi}{3} abc \frac{\epsilon_i(\omega) - \epsilon_h}{\epsilon_h + [\epsilon_i(\omega) + \epsilon_h]L_k}, \quad (2.23)$$

where L_k is the geometrical depolarisation factor for each axis ($\sum L_k = 1$), and increase in the axis length leads to the minimisation of the depolarisation factor. For spherical particles one has $L_a = L_b = L_c \cong 0.3$.

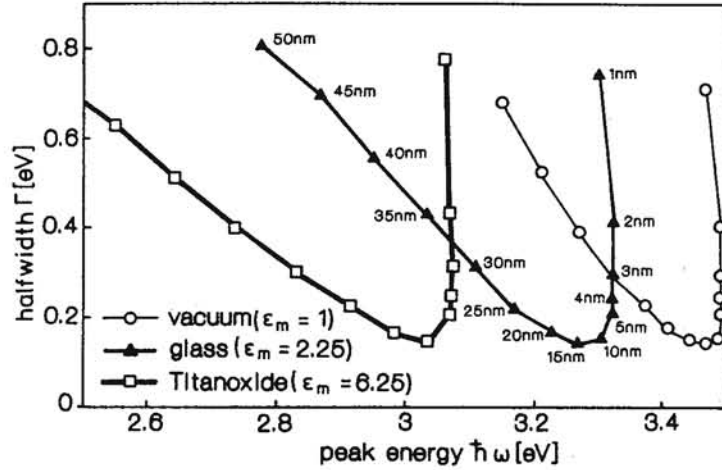


Figure 2.4: Plot of the halfwidth of the dipolar Mie resonance of silver nanoparticles versus the respective peak energy for several embedding media and particles size. Parameters with curves are the nanoparticles size. The figure is adopted from Ref. 16.

Thus, if the propagation direction and polarisation of the incident electromagnetic wave does not coincide with the axis of the ellipsoid, the extinction spectra can exhibit up to three SP bands [2.16]. For spheroids $a \neq b = c$ the spectra demonstrate two SP resonances with a spectral gap in between which rises with increase in the aspect ratio of the two axes of the spheroid (Fig. 2.5).

For many years now, the dichroic property of elongated metallic nanoparticles has been used for manufacturing of broad-band high-contrast polarizers [2.54]. This became possible owing to the fact that by appropriate choice of aspect ratio between the axes of the nanoparticles, the position of the SP resonance can be designed within a broad spectral range. This aspect will be discussed in more detail in the next chapter, however for now and as an example, typical excitation spectra of a soda-lime glass containing spheroidal silver nanoparticles for light polarised parallel and perpendicular to the major axis of the spheroids is show in Fig. 2.6.

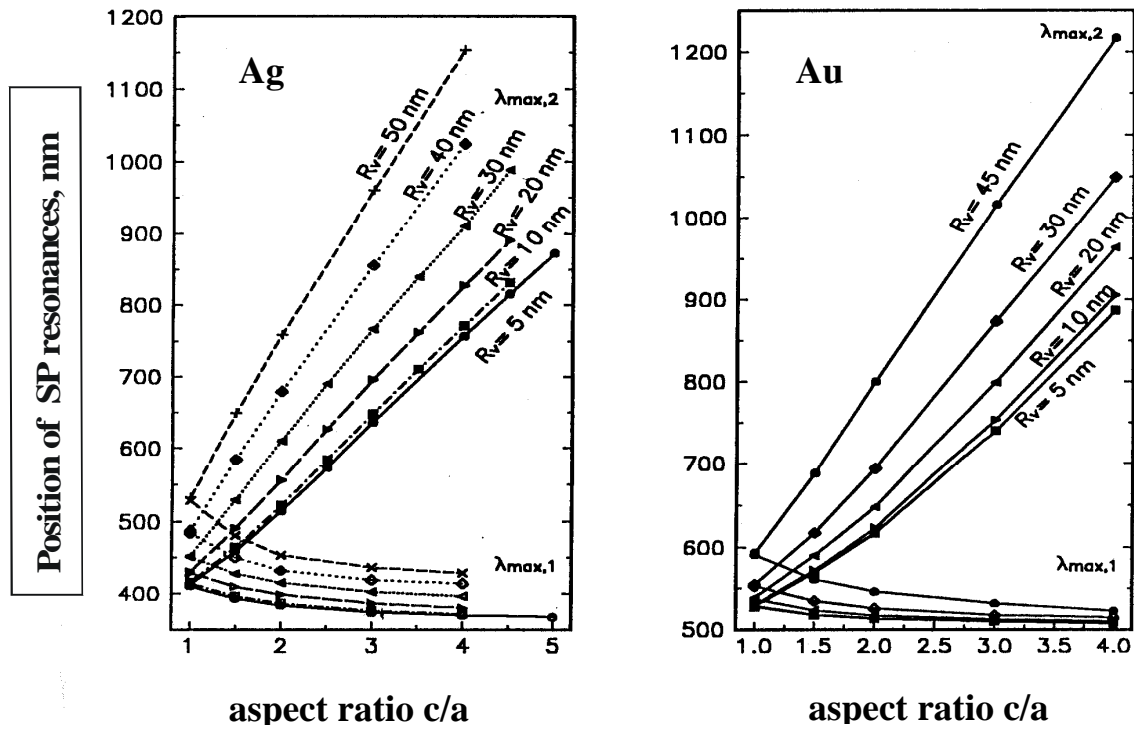


Figure 2.5: Position of SP resonances versus aspect ratio between axes of silver and gold spheroid nanoparticles. The figures are adopted from [2.16].

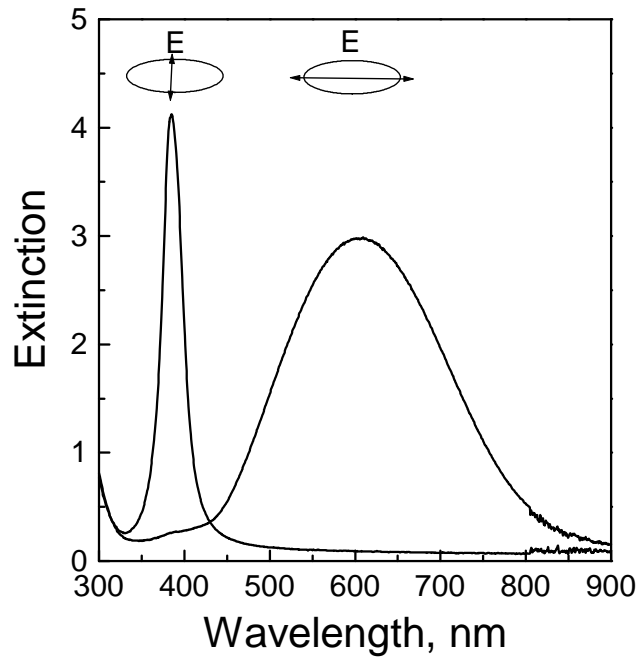


Figure 2.6: Polarised extinction spectra of soda-lime glass containing spheroidal silver nanoparticles.

2.4 Summary

In this chapter optical properties of metals and some of the properties of metallic nanoparticles have been discussed in brief. Efforts have been made to provide the necessary background for the rest of the thesis. The review of optical properties of metallic nanoparticles was restricted to those embedded in dielectric matrix and even though was limited to some of the key physical mechanisms behind their optical behaviour. The presented review is not intended to be comprehensive. Excellent reviews of optical properties of nanostructured random media can be found in Ref. 16 and 17.

The following chapters are mainly experimental and although it was intended to make them self consistent the information provided in this chapter will prove to be useful.

Chapter 3: Glass containing embedded silver nanoparticles: Preparation, Characterization & Properties

3.1 Introduction

This chapter is essentially devoted to detail description of preparation and characterisation of the samples used. I begin the chapter with a very brief review of the tools employed for characterization of the samples used during experiments presented throughout the thesis. The samples are glasses containing embedded silver nanoparticles. (Sometimes also referred to as silver-doped nanocomposite glass.)

This then followed by description of spectral properties of composite glass with considerable fraction of silver nanoparticles. To the material presented in the latter section is very frequently refereed throughout the thesis. The symbols and units used in the latter section are consistent with their usage in other sections of the thesis, Chap. 2 (2.3.1), although there are some unavoidable duplications in the usage of symbols.

3.2 Brief review of the characterization tools

As characterisation tools, along with the conventional tolls such as: confocal microscope, spectrophotometer, ext., the following tools were employed:

Scanning Electron Microscope (SEM). SEM is a microscope that uses electrons rather than light to form an image. There are many advantages to using the SEM instead of a light microscope. SEM has a large depth of field, which allows a large amount of the sample to be in focus at one time. SEM also produces images of high resolution, which means that closely spaced features can be examined at a high magnification. Preparation of the samples is relatively easy since most SEMs only require the sample to be conductive. The combination of higher magnification, larger depth of focus, greater resolution, and ease of sample observation makes the SEM one of the most heavily used instruments in research areas nowadays. All of the SEM pictures presented in this thesis were taken at IWZ Materialwissenschaft, MLU-Halle.

Transmission Electron Microscope (TEM). TEM works much like a slide projector. A projector shines a beam of light through a slide, as the light passes through it gets affected by the structures and objects on the slide. These effects result in only certain parts of the light beam being transmitted through certain parts of the slide. This

transmitted beam is then projected onto the viewing screen, forming an enlarged image of the slide. TEMs work in the same way except that they shine a beam of electrons through the specimen. Whatever part is transmitted is projected onto a phosphor screen for observation. All of the TEM pictures presented here were taken at Max Planck Institute of Microstructure Physics-Halle.

Scanning Near-field Optical Microscopy (SNOM). SNOM offers the use of a very small light source as the imaging mechanism. By using a quasipoint light source with a diameter much smaller than the wavelength of light, one can achieve resolutions better than the diffraction limit. The probe, however, must be very close to the surface; much closer than the wavelength of the light. This region is the "Near-Field" and thus the name of the technique. Typically, laser light is fed to the aperture via an optical fibre. The aperture can be a tapered fibre coated with a metal (such as Al), a microfabricated hollow AFM probe, or a tapered pipette. Normally, the size of the point light source determines the resolution obtainable. There are two types of feedback typically used to maintain the proper working distance of the probe to the sample. One method is quite similar to how feedback works with an AFM - by using a cantilevered probe, the normal force is monitored, typically by using a beam-deflection setup as in most AFMs. The second method uses a tuning fork. By attaching the fibre to a tuning fork, which oscillates at its resonant frequency, one can monitor changes in the amplitude as the tip moves over the surface. The tip is moved laterally, and this technique is normally referred to as "shear-force" feedback. Depending on the sample being imaged, there are multiple modes of operation for SNOM, such as: *Transmission:* Lightsource travels through the probe aperture, and transmits through sample. (This requires a transparent sample.) *Reflection:* Lightsource travels through the probe aperture, and reflects from the surface. Lower light intensity, and tip-dependent, but allows for opaque samples. *Collection:* Sample is illuminated from large outside light source, and the probe collects the reflected light. *Illumination/Collection:* The probe both illuminates the sample and collects the reflected light. Detection of the signal can be handled a number of different ways: Spectrometer, APD (Avalanche Photo Diode), Photomultiplier Tube, or a CCD. The SNOM pictures represented in the thesis (Chap. 6) were taken in-house using a α -SNOM in transmission mode.

3.3 Preparation and characterisation of glass containing silver nanoparticles

All of the samples used in the experiments were prepared from soda-lime float glass (72.5 SiO₂, 14.4 Na₂O, 0.7 K₂O, 6.1 CaO, 4.0 MgO, 1.5 Al₂O₃, 0.1 Fe₂O₃, 0.1 MnO, 0.4 SO₃ in wt%) by Ag⁺-Na⁺ ion exchange. For the ion exchange process glass substrate is placed in a mixed melt of AgNO₃ and KNO₃ at 400°C [3.1, 3.2]. The thickness of the glass substrate, time of the ion exchange process and weight concentration of AgNO₃ in the melt determine the concentration and distribution of Ag⁺ ions in the glass. Following thermal annealing of the ion exchanged glass in H₂ reduction atmosphere, typically at 400-450°C, results in the formation of spherical silver nanoparticles [3.1]. Depending on the ion-exchange conditions two types of silver-doped nanocomposite glasses can be produced, namely: polydisperse and monodisperse.

3.2.1 Polydisperse samples

The polydisperse samples contain spherical silver nanoparticles of 30-40nm mean diameter (Fig. 3.1A) which are distributed in a thin surface layer of $\sim 6\mu\text{m}$ thickness. (The polydisperse samples described here were prepared by CODIXX AG.) It has to be pointed out that size and distribution of the Ag nanoparticles in the depth of the glass sample depends strongly on temperature and time of $\text{Ag}^+\text{-Na}^+$ ion exchange as well as on the annealing time in the reduction atmosphere. Using SEM the volume filling factor ($f=V_{\text{Ag}}/V_{\text{total}}$) of silver nanoparticles was estimated to start at ~ 0.7 near the glass surface and decrease to zero within a few microns. This in fact defined as volume of the inclusions per unit volume of the composite material. Figure 3.1B

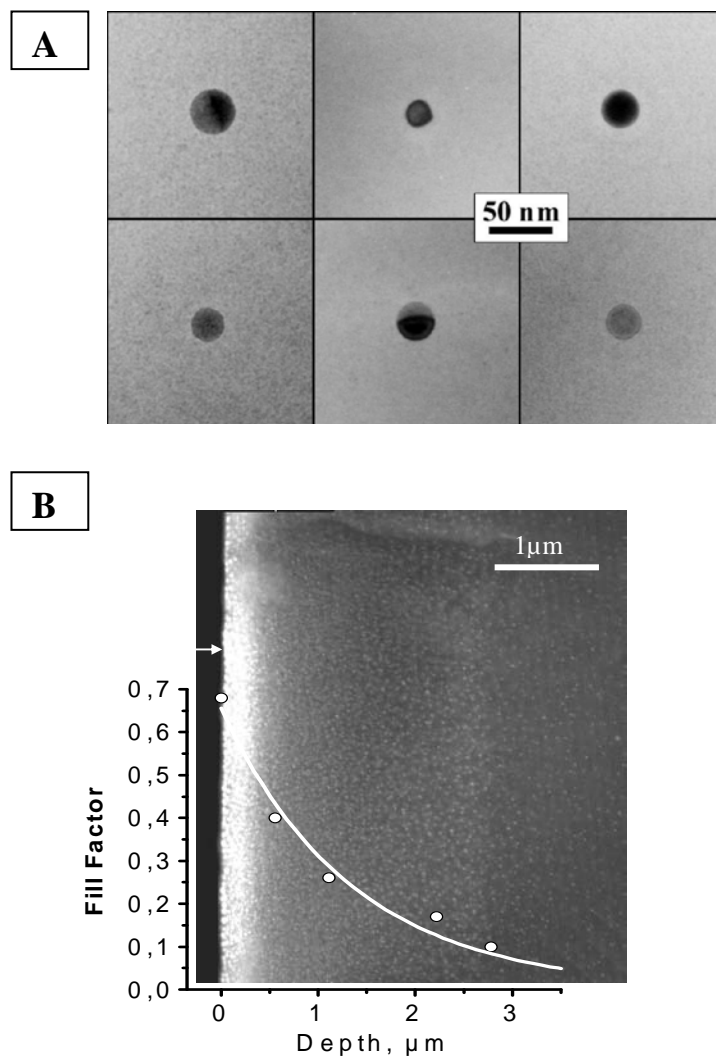


Figure 3.1: **A)** Transmission electron microscopy (TEM) picture of typical spherical silver nanoparticles in nanocomposite glass. **B)** Scanning electron microscopy (SEM) picture of the cross section of glass sample containing spherical silver nanoparticles (Ag particles are reproduced as white spots). The gradient of the volume filling factor of Ag nanoparticles is shown in superimposition (The x-axis was adjusted to the length scale of the picture).

shows the SEM picture of the cross section of the sample where silver particles are reproduced as white spots. In this figure the gradient of the volume filling factor of Ag nanoparticles is shown in superimposition. Hereafter and through out the thesis this type of samples where gradient of volume filling factor in the depth has an exponential profile are referred to as “*Polydisperse-Type I-Original*” samples.

The extinction spectrum of the sample is given in Fig. 3.2. As it can be seen the strength of the absorption band was so high that its peak, located between 412-420nm, could not be measured. The existence of gradient in this type of samples enabled us to produce samples with a very low silver filling factor by removing the upper particles layer of desired thickness, typically down to $\sim 3\text{-}5\mu\text{m}$. In fact experimentally the information on the distribution of silver clusters in the depth of the glass was obtained by removing surface layers of various thicknesses from the sample via etching in 12% HF acid for different retention times. After this procedure SEM was used to estimate the volume fill factor (f) of silver clusters in different distances from the original sample surface. Fig. 3.3 represents the typical results of the etching procedure. As is clearly seen in the SEM pictures of Fig. 3.3 (A) by increasing the etching time from left to right the silver content was decreased. The volume filling factor of the nanoparticles was then estimated to be $f \approx 0.08$ at the depth of $\sim 3\mu\text{m}$ and decreased to the lowest estimated value of $f \approx 0.006$ in the depth of $\sim 5\mu\text{m}$.

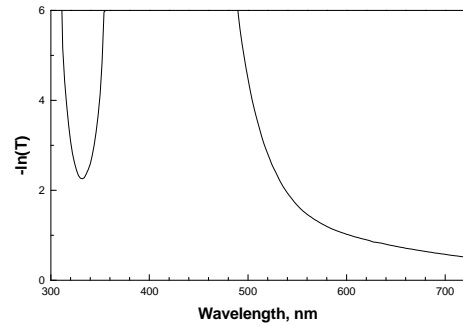
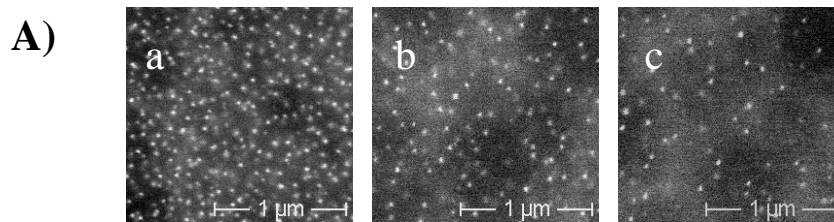


Figure 3.2: Extinction spectrum of the glass sample containing embedded spherical silver nanoparticles.



B)

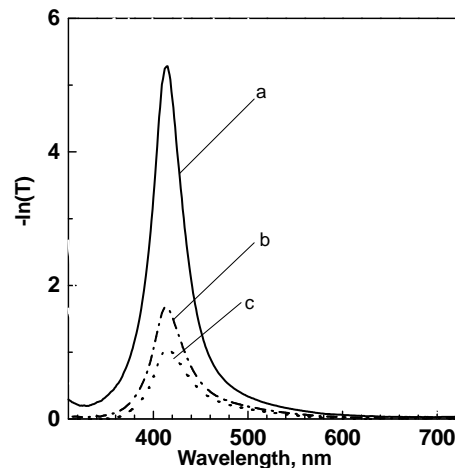


Figure 3.3: **A)** SEM pictures of samples with spherical silver nanoparticles etched in 12% HF acid. Pictures are ordered along with increase in etching time and hence decrease in estimated value for volume filling factor (f) of: 0.08 (a); 0.02 (b) and 0.006 (c). **B)** Experimentally measured extinction spectra of the same samples. Lettering of the spectra is according to the SEM pictures.

In Fig. 3.3 (B) the corresponding extinction spectra of the etched areas are presented, with the same lettering ((a) to (c)). By comparing spectra presented in Fig. 3.2 and Fig. 3.3 it can be clearly seen that while the original sample shows a strong and broad SP band corresponding to the spherical Ag nanoparticles incorporated in the glass matrix with high fill factor of up to 0.7 near to the surface of the matrix, etching of the sample in HF acid results in fading of the absorption band due to the decrease in thickness of the silver-containing layer as well as decrease of fill factor of nanoparticles in the sample. Through out the thesis the type-I samples with low volume filling factor of silver nanoparticles are referred to as “*Polydisperse-Type I-low filling factor*”.

Another type of the sample used here is a glass containing embedded elongated (elliptical) silver nanoparticles (Fig. 3.4A). These samples were made by applying tensile deformation and simultaneous heating to the *Polydisperse-Type I-Original* samples. This procedure resulted in production of samples containing strongly elongated (ellipsoidal) silver nanoparticles. Here the particle-containing layer was reduced in thickness to $\sim 1\mu\text{m}$. Figure 3.4B shows top view of the sample. The picture is taken using SEM. The penetration depth of the SEM signal was $\sim 100\text{nm}$. The elliptical shape of the nanoparticles can be recognized.

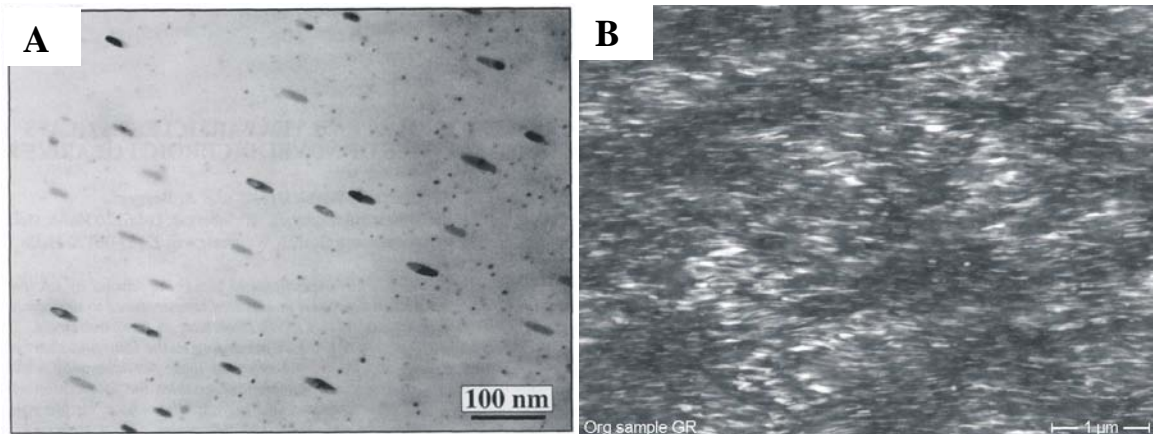


Figure 3.4: A) TEM picture of typical elliptical silver nanoparticles in nanocomposite glass. B) SEM picture taken from the surface of a sample containing embedded elliptical silver nanoparticles.

As a result of the macroscopic thermomechanical deformation process the final samples had a step profile of volume filling factor of silver nanoparticles in the depth. The overall thickness of the sample was also reduced from 1mm to $200\mu\text{m}$. Figure 3.5 shows a SEM picture take from the cross section of one of the samples of this type. This type of samples with embedded elliptical silver nanoparticles and step profile of filling factor are referred throughout the thesis to as “*Polydisperse-Type II*” samples.

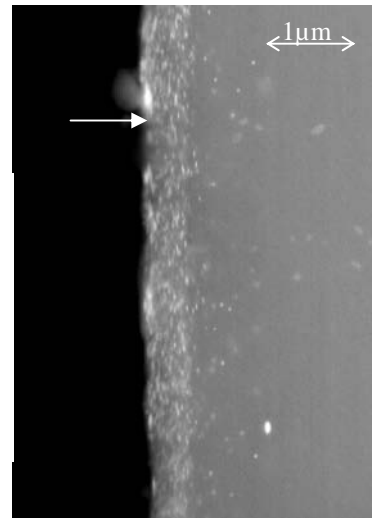


Figure 3.5: SEM picture of the cross section of glass sample containing elliptical silver nanoparticles (Ag particles are reproduced as white spots). The gradient of the volume filling factor of Ag nanoparticles is shown to have step profile.

Another important consequence of the deformation process is the uniform orientation of the elliptical nanoparticles in the final samples. This results in a strongly dichroitic optical extinction [3.3] and makes these materials very suitable as polarizers [3.4]. Figure 3.6 shows measured extinction spectra of the samples for two different polarizations of the incident light.

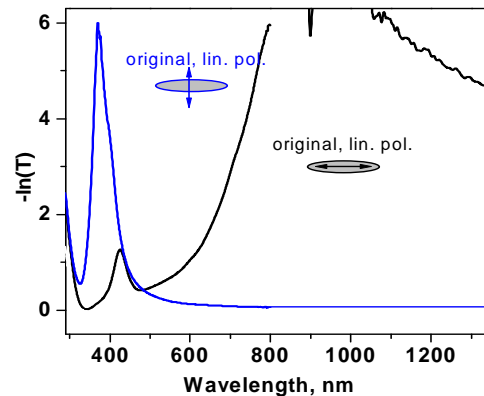


Figure 3.6: Extinction spectra of the sample containing elongated Ag nanoparticles (“Type II” samples) with light polarized parallel (black) and perpendicular (blue) to the long axis of the silver clusters.

3.2.2 Monodisperse samples

Homogenous distribution of silver cations in the glass substrate can be achieved depending on the duration of the ion-exchange process. The monodisperse samples used in this thesis contained silver nanoparticles with mean diameter of 30nm in a near surface layer of approximately 21μm.*

The nanoparticles were distributed with filling factor of $\sim 10^{-4}$. Extinction spectrum of the sample exhibited an absorption band which peaked at ~ 413 nm. This type of samples with embedded spherical silver nanoparticles and homogenous profile of filling factor are referred throughout the thesis to as “*Monodisperse-Original*” samples.

* The monodisperse samples were prepared by Dr. K.-J. Berg at MLU-Fachbereich Physik, Fachgruppe Experimentelle Physik I–Glasphysik.

3.3 Spectral properties of glass with high fraction of silver nanoparticles

Throughout study of spectral properties of any material could reveal its potential applications in photonics. In this context, silver-doped nanocomposite glass is not an exception and the spectral analyses are essential. For instance, the main stream of interest in study of interaction of laser light with composite glasses containing metal nanoparticles is due to their spectral properties. It is not difficult to understand if one recalls that spectral, and hence optical properties of composite glass are strongly depend on volume filling factor of the metallic inclusions. This can be explained if we remind from the last chapter that the absorption spectrum of a single metal particle is characterised by the well-known Mie resonance [3.5-3.7] occurring at the SP frequency ω_{sp} under the following condition:

$$\text{Re}[\varepsilon_i(\omega_{sp})] = -2\varepsilon_h, \quad (3.1)$$

where $\varepsilon_i(\omega)$ and ε_h are the complex dielectric constant of metal and surrounding matrix, respectively. This results in resonant enhancement of the dipole moment of the metal inclusion in a dielectric given as

$$\vec{p}(\omega) = 4\pi\varepsilon_0 R^3 \frac{\varepsilon_i(\omega) - \varepsilon_h}{\varepsilon_i(\omega) + 2\varepsilon_h} \vec{E}_0(\omega), \quad (3.2)$$

where R is the radius of the nanoparticle, E_0 is the electric field strength of an incident electromagnetic wave and ε_0 is the electric permeability of vacuum. With increasing metal content the average particle distances decrease, and thus also collective dipolar interactions between nanoparticles have to be considered, which strongly affect the linear and nonlinear optical properties of a nanocomposite material.

As a rough approach, it is sufficient to describe this effect in the approximation of the well known Maxwell-Garnett theory, which is widely applied to describe the optical properties of metal grains in dielectric matrices [3.7-3.10].* The Maxwell-Garnett theory does not correctly take into account the multipolar interactions between nanoparticles considered in other work [3.11-3.13]. However, yet it has widely used because it describes quite well the position and shape of the surface plasmon resonance and its dependence on the metal fill factor [3.8].*

* A widely explored approach for modelling the optical properties of a given composite media is via effective medium theories. These theories provide electromagnetically averaged optical constants for the medium, calculated in terms of the optical constants of the composing phases and their geometrical arrangement. The validity of these theories is typically limited by the size of the structures of the composing phases: large enough to locally preserve their own electromagnetic properties and sufficiently small for the composing media to appear as macroscopically homogenous [3.16]. Over the last century, a considerable number of such theories have been developed, being the two most successful approaches Maxwell-Garnett theory (MGT) [3.17] and Bruggeman effective medium approximation (BEMA) [3.18]. →

The effective dielectric constant $\epsilon_{eff}(\omega)$ of a composite material with spherical metal inclusions having a fill factor f is given then by the expression:

$$\epsilon_{eff}(\omega) = \epsilon_h \frac{(\epsilon_i + 2\epsilon_h) + 2f(\epsilon_i - \epsilon_h)}{(\epsilon_i + 2\epsilon_h) - f(\epsilon_i - \epsilon_h)}. \quad (3.3)$$

Using the Drude model for the dielectric constant of the metal we can then write:

$$\epsilon_i(\omega) = \epsilon_b + 1 - \frac{\omega_p^2}{\omega^2 + i\gamma\omega}, \quad (3.4)$$

where γ is the damping constant of the electron oscillations and ϵ_b is the core electron dielectric function. Here ω_p is the free electron plasma frequency given earlier (See Eq. 2.10).

It was previously been shown that based on this description, the absorption coefficient of a composite medium with dielectric constant $\epsilon_{eff}(\omega)$ can then be expressed as [3.15]:

$$\alpha_{ext}(\omega) = \frac{2\omega}{c} \text{Im} \sqrt{\epsilon_{eff}(\omega)}, \quad (3.5)$$

where c is the light velocity. It was also argued that the collective dipolar interactions between nanoparticles cause a significant broadening and red shift of the absorption band with increasing fill factor of silver inclusions in the glass matrix [3.15].

→

The MGT departs from the Clausius-Mossotti relation applied to a medium having a low filling factor of small homogeneous inclusions and takes into account their dipolar response. The effective dielectric function (ϵ_{eff}) of the composite medium can be calculated from:

$$\frac{\epsilon_{eff} - \epsilon_h}{\epsilon_{eff} + 2\epsilon_h} = f \frac{\epsilon_i - \epsilon_h}{\epsilon_i + 2\epsilon_h},$$

where ϵ_h is the dielectric function of the host, ϵ_i the one of the inclusions and f is the volume fraction (or filling factor) of the inclusions. This formula treats the matrix and the inclusions in an unsymmetrical fashion and it is in principle limited to low values of f since it neglects multipolar interactions among the inclusions. The MGT is able to describe qualitatively the surface plasmon resonances for metal-dielectric composites, but cannot account for percolation among the inclusions, except for the trivial case $f=1$.

In the BEMA the host and the inclusions are treated in a symmetrical way and both phases are considered to be embedded in the effective medium. In this case, the effective dielectric function can be determined from self-consistent calculations:

$$(1-f) \frac{\epsilon_h - \epsilon_{eff}}{\epsilon_h + 2\epsilon_{eff}} + f \frac{\epsilon_i - \epsilon_{eff}}{\epsilon_i + 2\epsilon_{eff}} = 0.$$

In contrast to the MGT, this model includes the percolation among the inclusions for filling factors $f \geq 1/3$. However, it is not able to represent appropriately the surface plasmon resonances for metal-dielectric mixtures [3.19].

Furthermore, using this feature particles located in regions with different metal fill factor in composite glass were excited using a laser with appropriate wavelength, and this led to the production of 3D structures in silver-doped nanocomposite glass via spatially selective nanoparticle deformation.

On the other hand, based on the description presented above, the refractive index of a composite medium with dielectric constant $\epsilon_{eff}(\omega)$ can be expressed as:

$$n_{eff}(\omega) = \text{Re} \sqrt{\epsilon_{eff}(\omega)} . \quad (3.6)$$

Using Eqs. (2.5), (3.3)-(3.4) and (3.6), the dispersion spectra (Fig. 3.7) of glass with spherical silver nanoparticles were calculated as a function of the volume filling factor of metal clusters in the glass matrix: $\epsilon_h=2.3$, $\omega_p=9.2$ eV, $\gamma=0.5$ eV [3.14], $\epsilon_b=4.2$ [3.10].

From Fig. 3.7 it is evident that varying the filling factor strongly affects the effective refractive index of composite glass. At filling factor as low as ($f \leq 10^{-4}$) the refractive index is equal to 1.54. Increasing of the filling factor results in dramatic increase of the refractive index, in fact from 0.5 to >3 in the visible spectral range.

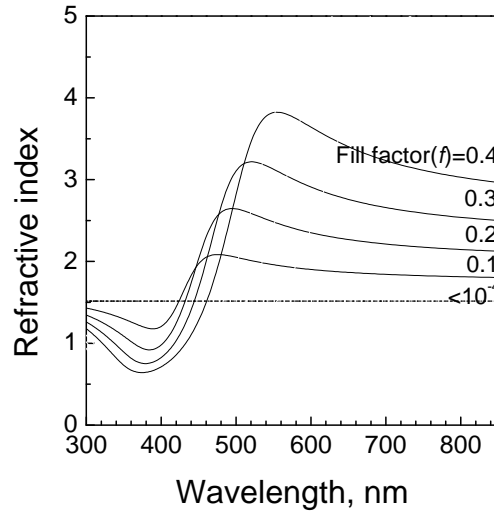


Figure 3.7: Calculated dispersion spectra of glass containing silver nanoparticles using Maxwell-Garnett theory.

Alterations in the absorption as well as dispersion spectra of the silver-doped nanocomposite glass could obviously result in variation of the reflection properties of the material with filling factor. This aspect will be considered in chapters 5 and 6. In fact it will be shown that growth of the metal content results in increase of the reflectivity from nanocomposite glass.

Thus the theory predicts that by controlling the filling factor of the metallic inclusions in metal-doped nanocomposite glass it should be possible to engineer the optical properties of these materials. Therefore, huge changes in refractive index as a result of increase and/or decrease in filling factor of the metallic inclusions can serve to produce various useful optical devices.

3.4 Summary

In this chapter, at first preparation and characterisation of the glass samples containing silver nanoparticles has been presented. These samples are used for the experiments described in the following chapters. This has then followed by description of spectral properties of glass containing considerably high fraction of silver nanoparticles.

Increasing of filling factor of silver inclusions in glass matrix leads to the broadening and red shift of the absorption band. This is believed to be due to the collective dipolar interaction between nanoparticles. Here it was shown that filling factor of the metallic inclusions also strongly affects the effective refractive index of the composite glasses as well.

Chapter 4: DC electric field-assisted dissolution (EFAD) of silver nanoparticles in glass matrix: Observations

4.1.1 Introduction

In this chapter result of the direct application of an electric field at moderately elevated temperatures towards glasses containing embedded silver nanoparticles is explored. It is shown that this procedure leads to the dissolution of the silver nanoparticles in the glass matrix.

The first part of the chapter is devoted to detail description of spatial features of DC electric field-assisted dissolution (EFAD) of silver nanoparticles in glass matrix. Here, some key information on the physical processes leading to the EFAD of silver nanoparticles in the glass matrix is provided. The extracted information is then used to discuss the proposed physical mechanism behind the dissolution process. This will then serve for better understanding of the following chapters.

4.1.2 Experiments and results

For the experiments performed here the following samples were used: Polydisperse-Type I-Original (glass containing spherical silver nanoparticles where the volume filling factor of the nanoparticles have an exponential profile); Polydisperse-Type I-low filling factor; Polydisperse-Type II (glass containing embedded elongated, ellipsoidal, silver nanoparticles where the volume filling factor of the nanoparticles have a step-like profile); Monodisperse-Original and Ag^+ - Na^+ ion exchange soda-lime glass. For all of the experiments described here and in fact throughout the thesis, only single sided samples were used, made by removing a sufficiently thick surface layer from one side of the samples by etching in 12% HF acid. The experiments were always performed inside a programmable furnace (Novodirect LABOROVEN-15L-1100°C, $\Delta\theta = \pm 0.2^\circ\text{C}$), designed for use in laboratories.

The experiments were carried out by equipping each sample with two pressed-contact steel electrodes (rectangular 6mm×9mm or circular with diameter of 10mm), and placing them in an air atmosphere inside the oven. The samples were equipped with electrodes so that the nanoparticles containing layer was facing the anode.

All of the samples were then heated to a temperature of ~280°C and then a DC voltage of 1kV across the thickness of the samples was applied using a high voltage source. (F.u.G. Elektronik HCE 7-3500 POS.)

Figure 4.1 shows a typical experimental arrangement for the samples.

Since soda-lime glasses possess high ionic conductivity [4.7], special procedure for the treatment of the samples employed. This procedure is consisted of applying the voltage in small amplitude steps, typically in steps of 0.2kV, in a way that during each step the current never exceeded a few hundred microamperes, typically $\leq 250\mu\text{A}$. The overall duration of the treatment was $\sim 50\text{min}$. The idea behind this procedure is generally aimed to avoid electric breakdown of the materials [4.8].*

At first this procedure was tested on a 1mm thick $\text{Ag}^+\text{-Na}^+$ ion-exchanged soda-lime glass. Evolution of the current flowing through the sample as a function of time during the procedure is given in Fig. 4.2.

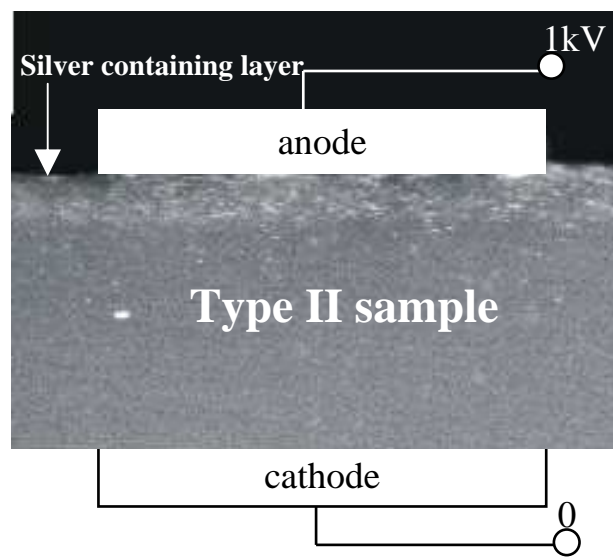


Figure 4.1: Typical experimental arrangement. The picture shows the cross section of a type II sample and as it can be seen the nanoparticles containing layer facing anode. The picture is not to scale.

* It has to be pointed out that a similar procedure has for years been using for the purpose of inducing second-order optical nonlinearity in various types of glass where the inversion symmetry of the glass matrix is broken by the internal electrostatic field which is frozen in the glass after treatment. As a result of this procedure second-order nonlinear response to intense light excitation is allowed. This technique is known in the field of optoelectronics as thermal poling of glass [4.5-4.7]. According to the generally accepted picture of the process the mechanism behind the localisation of the nonlinearity near the anodic surface as follows [4.7]: under the action of the voltage applied to the heated glass ($\sim 300^\circ\text{C}$) the alkali metal ions, in particular Na^+ because of its high mobility, and also H^+ will drift to the cathode where most of them are neutralised by incoming electrons, leaving behind a negatively charged region (so-called *ion depleted region*) near the anodic surface. It is believed that this results in appearance of a high electrostatic field in the depletion region, below the anode, and peaking at the surface. This procedure, however, to the best of the authors' knowledge has never been previously used towards glasses containing metallic nanoparticles.

One curious point which has to be pointed out here is that the common usage of the phrase electric-field poling refers to the direct application of an electric field with an external circuit [4.21]. However, in order to avoid any confusion with thermal poling of glass, I referred to the treatment presented here as DC electric field-assisted treatment.

A brief introduction to the thermal poling of glass is given in Appendix A.

Interestingly enough it was found that the ion-exchanged glass exhibited typical behaviour of soda-lime glass for the same parameters of treatment. (See for example Ref. 4.8.) From Fig. 4.2, it can be seen that at each step of treatment the current decreased with time (peak current remained below $\sim 200\mu\text{A}$) and the decay of current become slower from step to step, indicating that the resistivity of the ion-depleted region, beneath the anode, increased progressively.

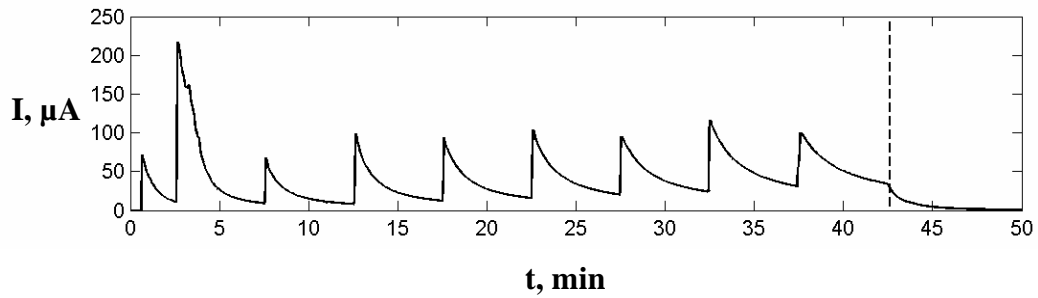


Figure 4.2: Evolution of current flowing through the ion-exchanged sample during the treatment at $\sim 280^\circ\text{C}$. Vertical dashed line indicates the beginning of cooling of the sample.

Samples containing silver nanoparticles, however, exhibited substantially different current dynamics in comparison with the ion-exchanged sample during the treatment. Figure 4.3 represents evolution of the current flowing through the samples during the treatment. In these samples the near surface layer is merely depleted of sodium ions and contains silver nanoclusters. Thus the *ionic conductivity* in the layer is expected to be low. This feature is consistent with the much smaller current which was observed in the first two or three steps of the treatment. (Fig. 4.3.)

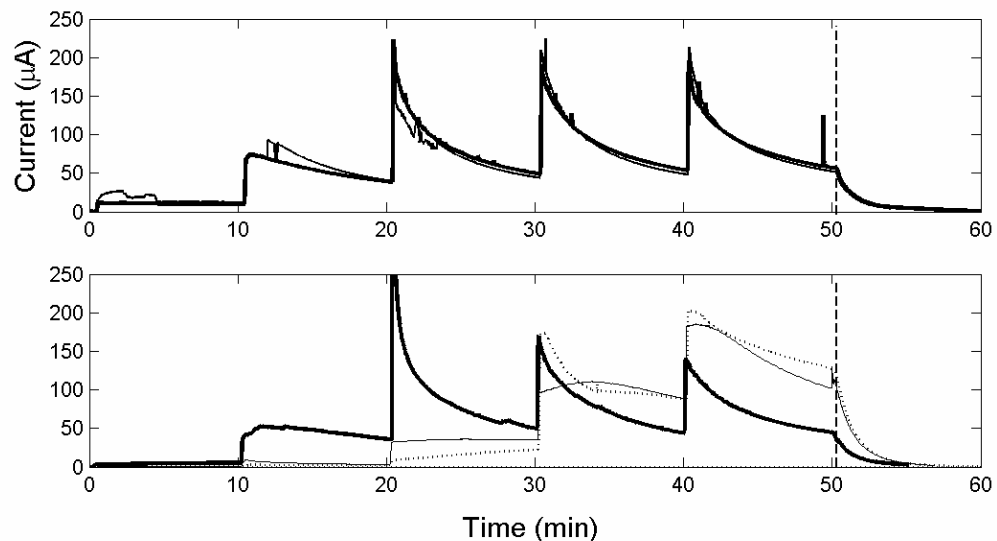


Figure 4.3: Evolution of current flowing through the sample as a function of time. Top chart: Current dynamics of three type II samples. Bottom chart: Current dynamics of the type I-original sample (Thin line), type I-low filling factor (Dotted line). The thick line in the bottom chart represents current dynamic of a type I-original sample which for comparison purposes was polished down to the same thickness as type II samples, i.e. $200\mu\text{m}$. Vertical dashed line indicate the beginning of cooling of the sample.

However, as it can be seen from the current dynamics, afterwards the conductivity increased dramatically and in fact the evolution of the current with time become somewhat, qualitatively, similar to that of the ion-exchanged glass (Fig.4.2.) This sudden change of behaviour is believed to be due to the onset of the dissolution of silver nanoparticles, as will be discussed next. However before going further and for better understanding of the processes it is important to mention some of the microscopic as well as macroscopic changes observed in the samples after treatment.

4.1.2.1 EFAD of silver nanoparticles in Polydisperse-Type II sample

Examination of the type II sample after treatment has revealed an interesting macroscopic effect. The glass region under the positive electrode (anode) has become completely transparent with sharp edges corresponding perfectly to the electrode size (Fig. 4.4). Since the original colour of the glass (green in the picture) is due to the presence of silver particles, the bleaching of the glass in the treated area is then obviously due to the absence of the nanoparticles, i.e. dissolution of the nanoparticles in the matrix. However, obviously further analyses were needed to prove this conclusion and also provide further hints towards understanding of the phenomena.

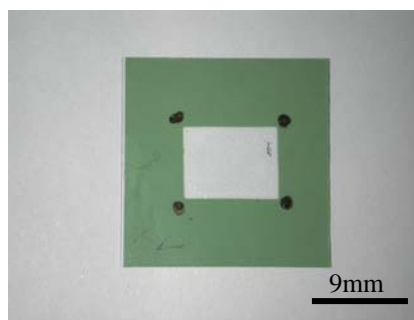


Figure 4.4: Photograph image of the type II sample after treatment. The glass became totally transparent under the anode after the treatment. The sharp edges of the bleached region correspond perfectly to the electrode size.

Figure 4.5 gives extinction spectra and SEM pictures of the sample before and after total bleaching. The spectra (fig. 4.5A) show that the strong surface plasmon resonance (SPR) bands of elongated silver nanoparticles in glass (dashed lines) have totally disappeared after the treatment (solid line). This effect is caused by dramatic changes in the sample nanostructure. In fact this can be easily seen in the SEM pictures presented in Fig. 4.5B and C, where the densely packed, uniformly oriented silver ellipsoids characterising the original sample (reproduced in white or light grey in Fig. 4.5B) are no longer present in the optically transparent region (Fig. 4.5C) after DC electric field treatment. In fact, a number of dark spots in figure 4.5C suggest the presence of hole-like structures (residual nanoholes) in the upper layer of the sample after treatment. (In Chap. 5 argument regarding the existence of nanoholes or nanopores will play an important role in discussion of modification of optical properties of samples after treatment.)

This once again suggests that the particles have been destroyed during the treatment without any (micro) damage of the glass matrix or surface, as was verified by optical microscopy.

After the modified sample was annealed at $\sim 600^\circ\text{C}$ for 6 hours in air atmosphere, an absorption band at a wavelength of $\sim 410\text{nm}$ occurred (red dashed line in Fig. 4.5 A), which is characteristic for spherical silver nanoparticles in glass. This indicates that while the silver nanoparticles have been destroyed during the treatment but silver ions are still present in the matrix and are in fact capable of re-aggregation upon the annealing procedure.

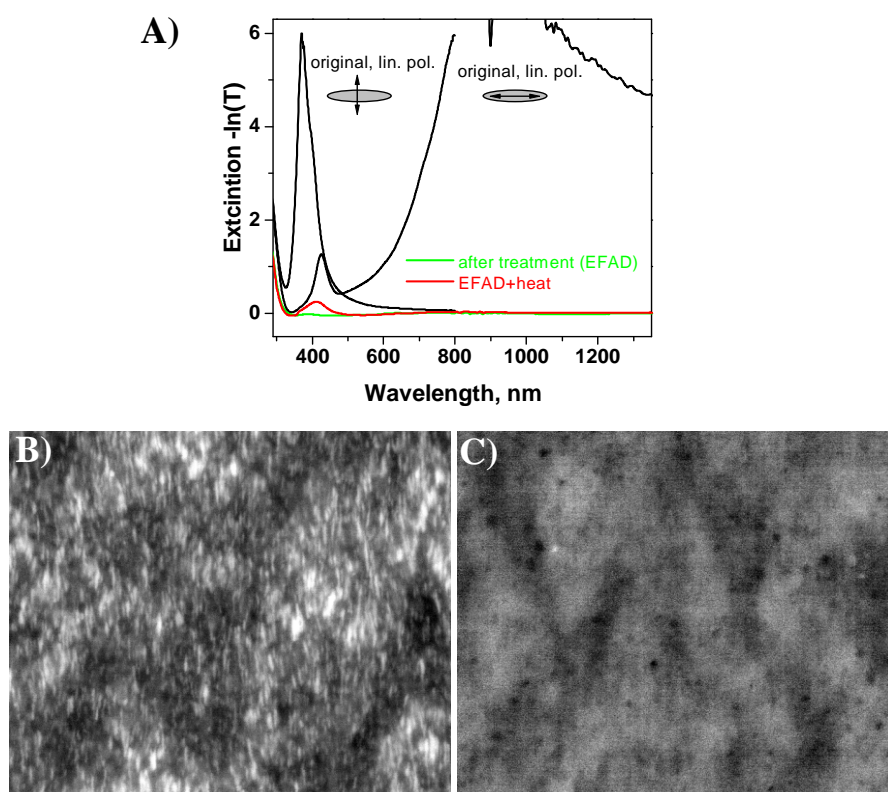


Figure 4.5: A) Extinction spectra of the Type II sample, before (black lines, observed with the light parallel and perpendicular to the long axis of the silver clusters) and after (green line, directly after the treatment; red line, after the treatment and additional heating) the treatment. B and C) SEM pictures of the surface of the sample before and after the treatment, respectively.

In another attempt towards better understanding of the processes a cross section of the sample was prepared and subjected to a SEM X-ray spectral analysis. The results are shown in figure 4.6 (left-hand side “A”, original sample; right-hand side “B”, modified sample). Taking the silica (Si) curve as the indicator for the position of the sample surface, it can be seen that both Ag and Na content have decreased close to the surface and increased in the depth of a few microns. The silver distribution after treatment has a maximum at a distance of approximately $2.5\mu\text{m}$ from the sample

surface. Since Ag atoms and ions as well as Na atoms and ions can not be distinguished in the X-ray signal, it is an obvious conclusion that these changes are due to a field-driven diffusion of Na and Ag ions. This confirms that the silver nanoparticles have been converted to silver ions.

These results are in fact in an excellent agreement with the previous observation where annealing of the sample after treatment resulted in appearance of SP band due to aggregation of silver ions in the matrix.

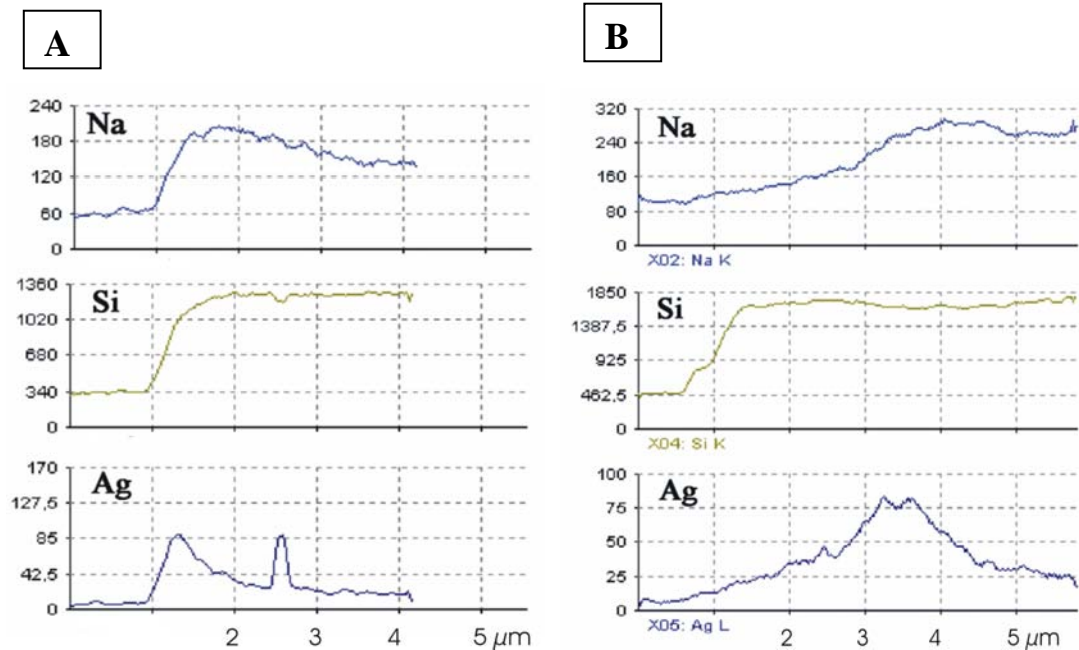


Figure 4.6: Na, Ag, and Si distributions as a function of sample depth by local X-ray element analysis of a cross sections of the sample (A) before and (B) after the electric field treatment; the horizontal length scales are identical. The Ag peak found in (A) at ~ 2.5 μm corresponds to a single, large silver nanoparticle, seen in the SEM picture (not shown).

4.1.2.2 EFAD of silver nanoparticles in Polydisperse-Type I samples

Unlike the type II samples, glasses containing embedded spherical silver nanoparticles with exponential gradient of filling factor (Polydisperse-Type I-Original) did only become partially transparent as a result of the identical treatment (application of 1kV over the thickness of the sample at ~280°C). Figure 4.7 shows photograph of the sample after treatment. This partial transparency also resulted in fading of the extinction spectrum of the sample (Fig. 4.8). The fading, however not disappearance, of the extinction spectrum clearly suggest that there are still some nanoparticles exist in the depth of the sample. These nanoparticles have obviously not been destroyed during the treatment.

For further investigation, one of the samples was polished down to ~0.2mm from the non-nanoparticles containing side. Thus, the sample had the same thickness as the Polydisperse Type II samples. Once again only partial bleaching of the glass beneath

the anode was observed. The current dynamics of this sample as a result of application of 1kV over its thickness at $\sim 280^\circ\text{C}$ is presented in Fig. 4.3 (thick line in the bottom chart). Hence, it was concluded that the extent to which the sample was bleached is not qualitatively depend on its thickness.

It was also found that in order to achieve complete transparency in the Polydisperse-Type I-Original samples a higher voltage of $\sim 3\text{kV}$ and hence longer time of treatment up to 180min was needed. Interestingly enough this was in fact the case for Polydisperse-Type I-low filling factor samples (with $f < 0.01$) as well.

On the other hand it was found that samples with a nearly homogeneous distribution of silver throughout their whole volume (Monodisperse-Original samples) could not be bleached even up to the electrical breakdown. This suggested that for the applied conditions EFAD of silver nanoparticles occurs when the particles have a considerable spatial gradient and/or in more general terms density, which in turn is restricted to only a thin layer (\sim a few μm) close to the surface.

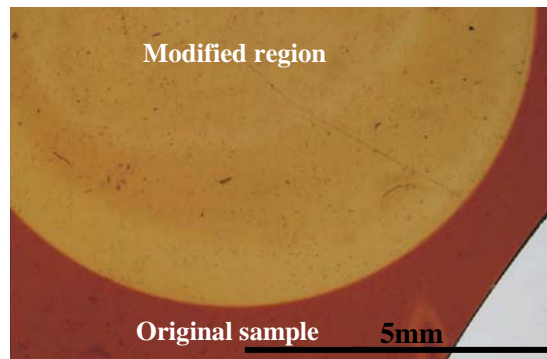


Figure 4.7: Photograph image of the type I-original sample after treatment. The glass, under the anode, became only partially transparent as a result of the treatment. The sharp edges of the bleached region correspond perfectly to the electrode size and shape.

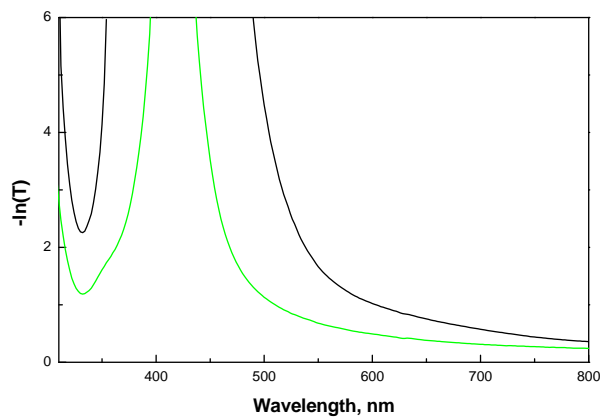


Figure 4.8: Extinction spectra of the Type I-original sample, before (dot line) and after (solid line) the treatment. Unlike the type-II samples only fading of the spectrum after treatment was observed. This was attributed to the existence of non-dissolved silver nanoparticles in the depth of the sample and will be explained in the next section.

It is beneficial to conclude the experimental part with two extra but very important observations regarding the EFAD of the samples;

- a) At room temperature ($\sim 25^{\circ}\text{C}$), high voltage of $\sim 4\text{kV}$ was applied to a 1mm thick Polydisperse-Type I-Original sample. No macroscopic change, including partial transparency or colour change of the treated area, was observed for 5min, 15min and 30min of treatment.
- b) A Polydisperse-Type I-Original and a Polydisperse-Type II samples were treated with the nanoparticles containing layer facing the cathode instead of the anode. After the treatment, 1kV at $\sim 280^{\circ}\text{C}$, no change at all was observed for 50min of treatment.

4.1.3 Synopsis of the observations

The given observations and analysis clearly made it possible to go one step further and set up the physical processes leading to the EFAD of silver nanoparticles in glass.

It is well-known that in contrast to the pure soda-lime glass, where the conductivity at $\approx 300^{\circ}\text{C}$ is dominated by the migration of Na^{+} cations in the matrix (see Appendix A), in composite materials containing metal nanoparticles the contribution of conduction electrons play the primary role for the electric current [4.9-4.15]. It has already been observed and confirmed by many researchers that the conductivity of these materials approaches that of a bulk metal with increasing fill factor of the metallic nanoparticles in a given dielectric matrix [4.11, 4.12, 4.15-4.17].

In fact the dependency of conductivity with filling factor and temperature for silver-doped nanocomposite glass can be qualitatively assessed by means of a simple experiment, namely by equipping a sample of a kind with two electrodes so that both of them are facing the nanoparticles containing layer. Here it was done by means of two electrodes, size of $10\text{mm}\times 10\text{mm}$, placing them $\sim 1\text{mm}$ apart. The experiment was performed for two polydisperse-type-I samples having a filling factors of $f=0.1$ and $f=0.001$. (The filling factors were assessed via SEM, and were intentionally chosen to be small in order to avoid the onset of modification processes during the measurements.) The samples were heated to different temperatures as a constant voltage of 0.2kV was applied and for each temperature the amount of the generated current was measured. Figure 4.9 shows the results, where it can be seen that while a measurable current for the sample with higher filling factor (left) can be registered at $\sim 170^{\circ}\text{C}$, for the sample with a very low filling factor (right) the threshold of the current registration is as high as 300°C . This simple experiment hence supports the idea of high electronic conductivity in the nanoparticles containing layer.

In fact the accustomed picture to describe generation of electric current in such systems is that of a heterojunction of metal and insulator [4.18], where the energy of conduction electrons in the metal clusters has to exceed the potential barrier formed by the interstitial insulator layer. If the volume filling factor of metallic inclusions is high enough, the potential barrier between two neighbouring metal clusters is so low that thermally activated electron tunnelling as well as hopping is possible. This in

turn leads to the repeatedly observed rise of conductivity in systems as such, upon increase of temperature, as was reported in [4.10-4.13].

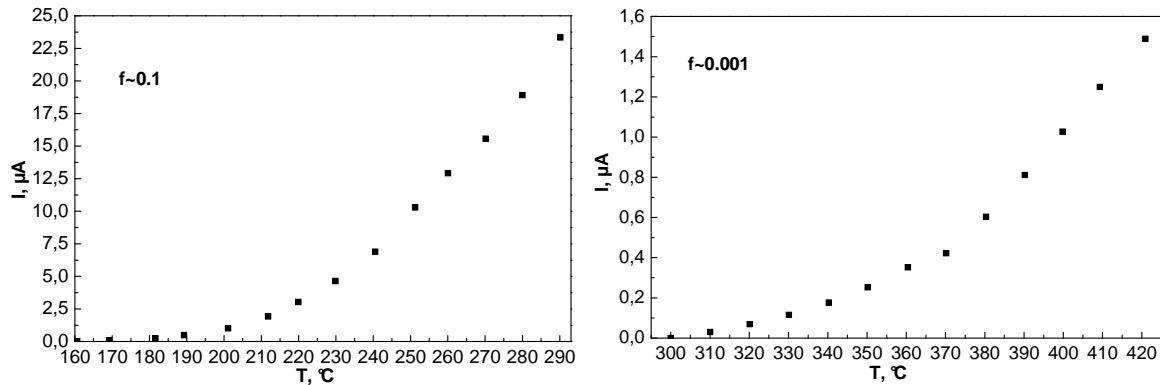


Figure 4.9: Current versus temperature characteristic of two samples with different filling factor, $f \sim 0.1$ (left) and $f \sim 0.001$ (right). For these measurements both electrodes were placed on the nanoparticles containing layer. See the difference in thresholds for registration of current.

An additional increase of conductivity in these systems can be expected in the presence of trapping centres in the glass in the form of interstitial cations or positively charged anion vacancies [4.19], via reduction of the height of the potential barrier for electron tunnelling.

Here glass with embedded silver nanoparticles in a near-surface region constitutes a composite material with high electronic conductivity in the cluster-containing layer, and (much lower) cationic conductivity throughout the remainder of the material (glass). When an electric field is applied to such a sample in a way that the anode is facing the particle-containing layer, there will be a current due to electrons tunnelling from the silver clusters towards the anode, and owing to the high electron mobility this process would leave the silver particles in a positively charged state. Since there is a considerable field enhancement in the vicinity of Ag nanoclusters [4.20], it is highly probable that they will be further ionized until, due to strong Coulomb forces, silver ions are being ejected from the metal clusters and then diffuse away from the anode. Fig. 4.10 shows a schematic diagram of the process.

At the same time, an additional field enhancement could be present due to a cation depletion zone, which plays an important role for thermal poling of glass (see Appendix A). This Ag^+ ejection increases the fading electronic conductivity, because now again there will be uncharged silver clusters having electrons of high mobility.

Here it is important to note that as long as the Ag ions have not yet diffused out of the particle-containing region, they may further increase the probability for electron emission by decreasing the height of the tunnelling potential barrier. These processes can go on until the Ag nanoparticles are completely destructed and the produced silver cations have been dissolved in the glass matrix.

The central point of this line is the electronic current and thus the height of the potential barrier for tunnelling of electrons, which decreases strongly with the

average distance from cluster to cluster. This explains easily the experimental observation that samples with a low silver fill factor are not being modified by an applied electric field of $\sim 1\text{kV}$ across their thickness at $\sim 280^\circ\text{C}$, and suggest much higher threshold of modification for these samples, typically $\sim 3\text{kV}$. The presented picture of the physical processes also explains that no changes were observed with exchanged electrodes (i.e., cathode placed on the layer with Ag nanoparticles), because then a thick layer of insulating glass (with respect to electrons) between the anode and the layer containing silver nanoparticles prevents the electronic current and ionization of the clusters.

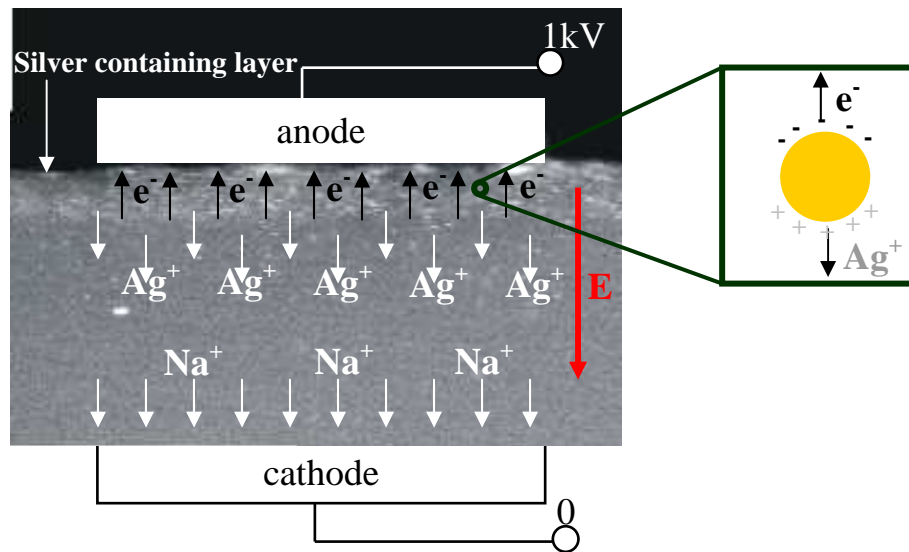


Figure 4.10: Schematic diagram of the process. Under the combined action of the applied DC electric field across the sample and moderately elevated temperatures silver nanoparticles are being dissolved in the glass matrix.

However, while the present discussion in principle explain most of the observations, it is crucial to have a closer look on the evolution of the modification processes in order to seek better understanding of the phenomenon. This aspect is discussed in the next section.

4.2 DC electric field-assisted dissolution (EFAD) of silver nanoparticles in glass matrix: Processes

4.2.1 Introduction

Thus far, it was shown that application of a DC electric field at elevated temperature is capable of bleaching silver-doped nanocomposite glass up to a complete transparency. In fact, depending on the nanocomposite characteristics, e.g. volume filling factor of the nanoparticles, and experimental conditions (applied DC voltage of 1kV across the samples at elevated temperatures of $\sim 280^{\circ}\text{C}$) either complete or partial bleaching of the glass was demonstrated with sharp edges corresponding to the electrode size. The underlying physical mechanism has been identified as electric-field assisted dissolution (EFAD) of embedded silver nanoparticles.

However, some of the questions regarding dynamics of the bleaching remain unanswered. For instance, while during the treatment voltage was increased step by step up to 1kV there is no indication that at which voltage step the bleaching appeared and how long it took to complete. Moreover, experiments were performed at a fix temperature of $\sim 280^{\circ}\text{C}$. The goal now is to address these issues. In the following, glasses containing silver nanoparticles are treated using various combinations of voltage, time and temperature.

4.2.1 Experimental

For the experiments presented samples of 1-mm thick from soda-lime float glass containing embedded spherical silver nanoparticles with exponential profile of filling factor (Polydisperse-type I-original samples) were used.

First experiment is performed by equipping one of the samples with two flat press contact steel electrodes ($6\times 9\text{mm}^2$) so that the positive electrode was facing the nanoparticles containing layer, then placed in air inside the oven, and was subjected to eight successive treatment steps at $\sim 280^{\circ}\text{C}$ in the following sequence: 0.2kV-10min, 0.2kV-20min, 0.2kV-40min, 0.4kV-10min, 0.6kV-10min, 0.8kV-10min and 1kV-15min.

Between each step of treatment, using an UV-visible-NIR spectrometer (with 2-mm diameter aperture) transmission spectra from the uniformly bleached region of the sample were recorded.

Besides, six additional samples (identical to the one used earlier) were treated at various temperatures: 150°C, 190°C, 220°C, 250°C, 280°C and 300°C. In the latter case, the voltage was increased by steps of 0.2kV (10min each) and up to 1kV. This was done for the sake of comparison with the experimental results previously presented.

4.2.2 Results and Evolution of EFAD

The experimentally measured extinction spectra of the sample treated at the constant temperature of ~280°C, however at various time-voltage steps is presented as solid curves in Fig. 4.11. As it can be seen, while at this temperature bleaching occurred for the applied voltages lower than 1kV (namely, at 0.2kV and at 0.6kV as can be seen from Fig. 4.11-b and -c, respectively), however yet the strength of the surface plasmon resonance (SPR) band was so high that its peak could not be measured, as in the pristine sample (Fig. 4.11-a). After treatment of up to 1kV, however, the entire band could be measured, revealing SPR band at approximately 420nm (4.11-d).

Within the surface plasmon resonance (SPR) range for spherical silver nanoparticles in soda-lime glass in the visible spectral region [4.22], the extinction spectrum of metal-doped nanocomposite glass can be calculated from the Maxwell-Garnett theory via the following expression:

$$E = \frac{2\omega}{c} \int_0^L \left[\text{Im} \left(\sqrt{\epsilon_h \frac{(\epsilon_i + 2\epsilon_h) + 2f(x)(\epsilon_i - \epsilon_h)}{(\epsilon_i + 2\epsilon_h) - f(x)(\epsilon_i - \epsilon_h)}} \right) \right] dx, \quad (4.1)$$

where the expression under the square root is the familiar effective (complex) dielectric function, $\epsilon_{eff}(\omega)$, (see chapter 3), L in the sample thickness, c is the speed of light, ω is the angular frequency, ϵ_i and ϵ_h ($\epsilon_h = 2.23$) are the dielectric constants of the metal and host material, respectively. The complex function ϵ_i was calculated using the Drude model of a metal (see Eq. 2.19). In the case of silver, $\hbar\omega_p$ is equal to 9.2eV and the function $\epsilon_i(\omega)$ is well approximated, within the wavelength range of interest, by taking $\epsilon_b = 4.0$ and $h\gamma = 0.5$ eV [4.23].

Assuming that bleaching proceeded “layer-by-layer” from top surface one can defined d as the thickness of the layer where $f(x)=0$ as a result of bleaching ($0 < x < d$). In unbleached layers ($d \leq x \leq L$), on the other hand, one can take:

$$f(x) = f_0 \exp(-x/w_f). \quad (4.2)$$

The values of f_0 and w_f were determined by fitting the extinction spectrum of pristine sample using Eq. (4.1) and $d = 0$. The value of d after treatment was determined by fitting the extinction spectrum of bleached sample using Eq. (4.1) and d as free parameter. By fitting the measured extinction spectra, the evolution of d with time and voltage was estimated (Fig. 4.12).

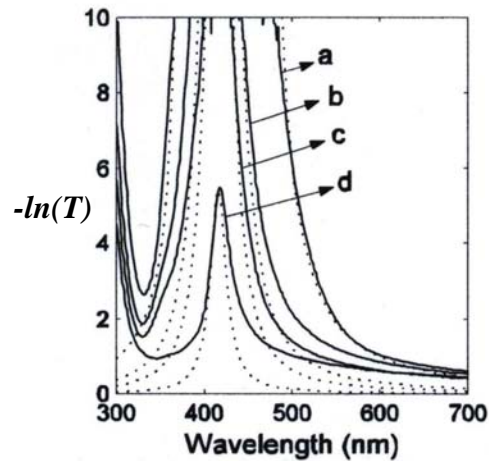


Figure 4.11: Extinction spectra of glass containing spherical silver nanoparticles with exponential gradient of filling factor (solid curves): as-received sample (a); sample treated at 280°C with successive time-voltage steps (see text): after 40min-0.2kV step (b), after 10min-0.6kV step (c), after 15min-1kV step (d). Dotted curves are best fits to Eq. (4.1).

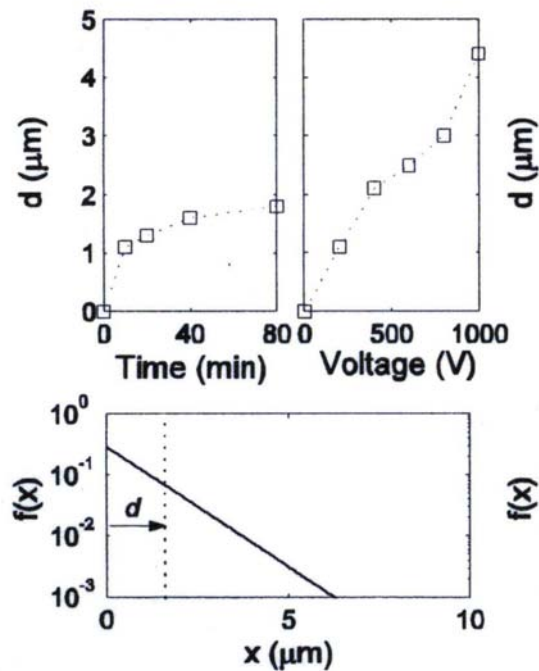


Figure 4.12: Top charts: Thickness of bleached layer as a function of time and voltage. Bottom chart: Depth gradient of particle's volume filling factor in pristine sample. The values of d were obtained by fitting extinction spectra. Knowing the value d , the filling factor at depths $x \geq d$ can be calculated.

Current measurements of the EFAD process showed that the current dynamics changed as bleaching developed. This is an interesting feature of the EFAD process. The current dynamics are presented in Fig. 4.13. From the current dynamics, it can be seen that due to the mixed mobile ion effect [4.26], the conductivity is expected to change with the fraction of dissolved particles in the host (denoted for simplicity x).

When $x \ll 1$, the current is mainly due to the migration of ions originally present in the host (e.g. Na^+). This situation is likely to prevail during the first step where the current dynamics (Fig. 4.13 – a) is more similar to that in soda-lime host glass (Fig. 4.13 – s) than in Ag^+ - Na^+ ion-exchanged host glass (Fig. 4.13 – i). As x increases, the current dynamics changes in a quite complicated way (Fig. 4.13– b to g).

Accurate description of the current dynamics would require taking into account mixed motion of Ag^+ and Na^+ , evolution of relative ion concentrations, and electron contribution. This is obviously is not a trivial task and was only qualitatively explained in section 4.1.2. What can, however, be said here in that increase of the contact area is expected to increase the current (particle dissolution extends to new regions of the glass). Bumps and jumps in the current evolutions – either during the treatment stage at 280 °C (Fig. 4.13 – e, g) and/or the cooling stage (Fig. 4.13 – f, g) – are attributed to gradual and sudden changes of the contact, respectively. The contact issue is further investigated in Appendix B.

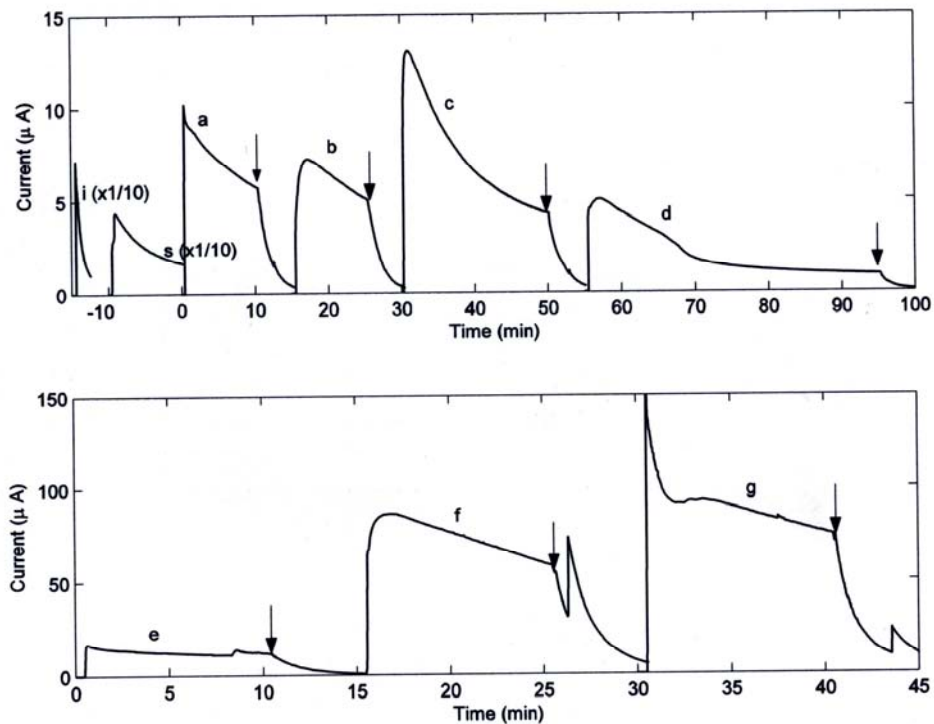


Figure 4.13: Evolutions of the current in Ag-doped nanocomposite glass during the first seven steps. Voltage: 200 V (a-d), 400 V (e), 600 V (f) and 800 V (g). Curves were shifted along time axis for clarity. Vertical arrows indicate the beginning of cooling. Evolutions of the current during the treatment (280 °C, 200 V) of soda-lime host glass (s) and Ag^+ - Na^+ ion-exchanged host glass (i) are shown for comparison (current values were divided by 10).

From what was said up to now, the results presented here show that applying a voltage as low as 200 V across the sample is sufficient to initiate the dissolution of spherical Ag nanoparticles. Re-heating of the sample before each next treatment step obviously caused redistribution of mobile ions (Na^+ , Ag^+) in the host. However, it is

unlikely that re-aggregation of silver clusters occurred during this heating because the temperature (280 °C) is not sufficient. The results also showed that bleaching increased for longer times of the treatment (at 200 V) until saturation took place and that higher voltages were required to increase it further. Incomplete bleaching is due to the presence of silver nanoparticles which are located deeper in the depth with smaller filling factor, where the electric field strength is not high enough to cause their dissolution. The filling factor plays a critical role here as the uppermost layers (with larger filling factor) are expected to be dissolved first. As the voltage is increased, the electric field gradient which results from ion depletion increases in strength and extends deeper in the host. Both the higher local field strength and the extension of the depletion layer contribute to dissolve those silver particles which remain deeper in the glass.

On the other hand, temperature dependence dynamics of the EFAD process revealed that by applying a voltage of 1kV across the sample, bleaching occurs in the temperature range from 150°C to 300°C (Fig. 4.14, f and g). However, SPR peak decreases considerably and in fact can be recorder by the spectrophotometer, only for treatments at temperatures above 280°C (Fig. 4.14, g). It is important to point out that samples could not be treated above 300°C because of current runaway due to high ionic conductivity of the host glass. (This is due to the fact that the current flow locally increases the temperature and this leads to even more current flow and consequently more heat. Eventually current tends to diverge. This process is known as “thermal run away”.) Once again by fitting measured extinction spectra, the evolution of d , however this time with temperature was determined (Fig. 4.15).

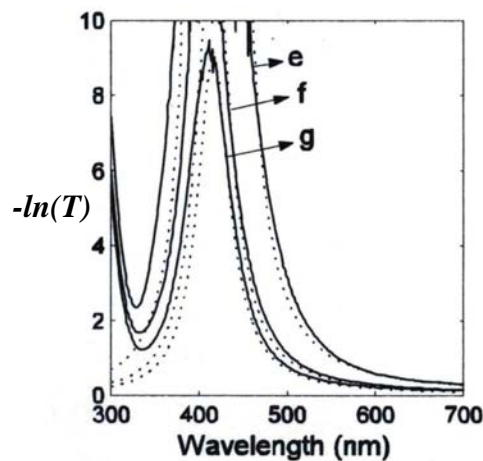


Figure 4.14: Extinction spectra of glass containing spherical silver nanoparticles with exponential gradient of filling factor (solid curves): as-received sample (e); samples treated up to 1kV at various temperatures: 220°C (f) and 280°C (g). Dotted curves are best fits to Eq. (4.1).

A remark concerns the fitting of the extinction spectra. For pristine samples, best fits were obtained by taking $h\gamma=0.5$ eV whereas, for the treated samples, the following values were taken: $h\gamma=1.0$ eV (Fig. 4.11) and 2.0 eV (Fig. 4.14), in order to improve the fit quality. The resulting broader SPR band can be interpreted, in terms

of the Mie's scattering theory [4.26], as a decrease of particle's (mean) diameter, here from 30~40 nm to less than 10 nm [4.27]. For those particles subsisting in glass after treatment, it could mean that only a fraction of silver ions was ejected from the cluster.

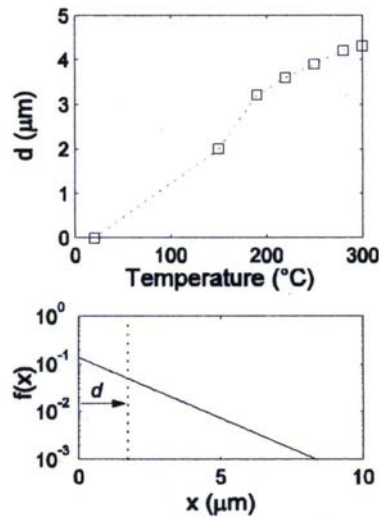


Figure 4.15: Top charts: Thickness of bleached layer as a function of temperature. Bottom chart: Depth gradient of particle's volume filling factor in pristine sample. The values of d were obtained by fitting extinction spectra. Knowing the value d , the filling factor at depths $x \geq d$ can be calculated.

Current dynamics as a function of time for different temperatures are presented in Fig. 4.16. For the experiments six identical polydisperse-type I-original samples were equipped with two electrodes with anode facing the nanoparticles containing side, placed inside the oven, heated to different temperatures ranging from 150°C to 300°C , and each was subjected to the applied voltages from 0.2kV to 1kV with steps of 0.2kV. The duration of each step was 10min.

As it can be seen from the figure, dynamics of dissolution is different for treatment at temperatures lower than 280°C (see circles). An important feature of the treatments is the slow rise in current after increasing the voltage, which then reaches a steady state level with time. This is indeed in contrast with the dynamics of the samples treated at higher temperatures (280°C and 300°C), where a sudden jump in current just after increasing the voltage is observed.

It is plausible that here owing to the slower dynamics, at some depth the electrons moving towards anode may neutralize the Ag cations on their way, thereby increasing the silver concentration at a certain depth. This can lead to production of a layer containing "percolated" silver clusters, at a certain depth, depending, presumably, on the experimental conditions such as: applied voltage, temperature or both simultaneously.

This aspect of the work is further explored in the next chapter, where slower dynamics for treatment at lower temperatures than 280°C , namely $\sim < 250^{\circ}\text{C}$, is used for production of percolated silver nanolayers inside glass.

From what was said so far the evolution of bleaching with treatment conditions can be explained in terms of the underlying electric field-assisted dissolution of embedded metal nanoparticles. Both ionic and electronic conduction must be taken into account here. While in the glass matrix, thermally activated migration of mobile ions (such as Na^+) leads to the formation of ion depleted layer underneath the anode where a high electric field builds up [4.24, see also Appendix A], in our case this field is further enhanced in the vicinity of silver nanoparticles.

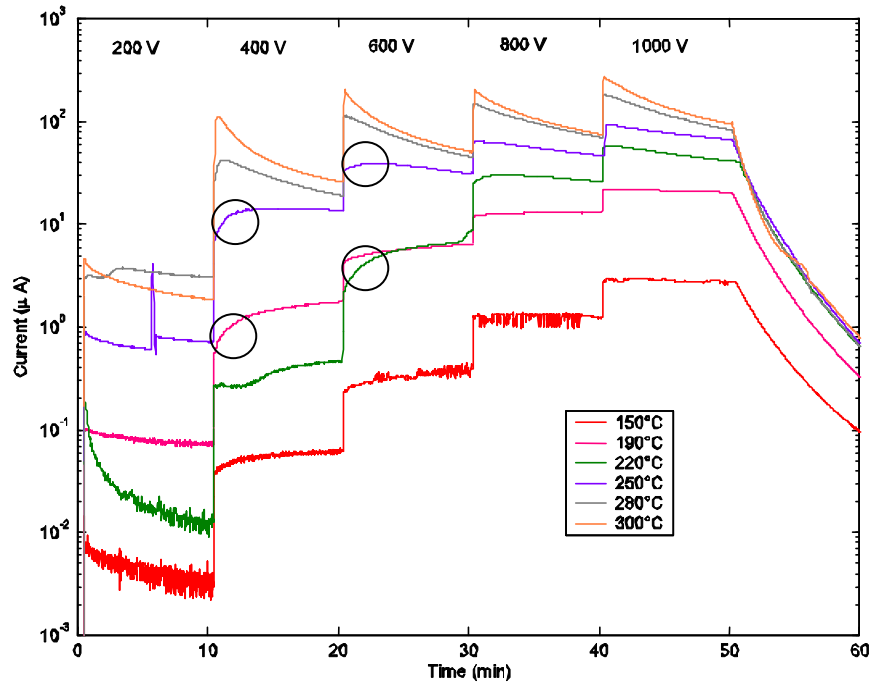


Figure 4.16: Current as a function of time in samples with spherical silver nanoparticles. Samples were treated by steps of 0.2kV (10min) up to 1kV. Treatment temperatures: 300°C, 280°C, 250°C, 220°C, 190°C and 150°C.

On the other hand, as soon as the threshold for ionization of the silver clusters is exceeded, electrons move towards the anode and silver ions, which are ejected from the ionized clusters due to strong Coulomb forces, drift away in the depth. Since silver clusters in regions of high filling factor (close to the surface in our samples) are ionized first, the dissolution proceeds “layer-by-layer” from the top surface. It has to be pointed out that both release of silver ions and injection of H_3O^+ or H^+ from atmosphere (at the anode) should be taken into account for a more complete description of the ion depletion process.

On the other hand, incomplete bleaching for the applied voltage of 1kV across the sample at 280°C can be explained by, and is believed to be due to, the presence of nanoparticles which are located deeper in the depth with smaller filling factor, where the local electric field strength is not high enough to cause their dissolution.

As the voltage is increased, the electric field increases in strength and extends deeper in the sample. As it was said before application of $\sim 3\text{kV}$ across the polydisperse-type I-original samples is enough for complete bleaching of the treated area.

The actual field distribution depends on ion depletion and metal cluster distribution in a non-trivial way. Thus, both the higher local field strength and the extension of field distribution contribute to dissolve those silver particles which remain deeper in the glass. The increase of d , thickness of the bleached layer, with temperature (see Eq. 4.1), on the other hand, is consistent with the thermally activated nature of the ion migration process.

4.3 Summary

In this chapter, at first, the effect of an intense DC electric field applied to glass samples containing silver nanoparticles in a thin surface layer of a few micrometers was investigated and discussed. It was shown that at elevated temperature of about $\sim 280^\circ\text{C}$, and using samples with sufficiently high silver volume fill factor, the silver clusters can be destructed completely into Ag ions, which are being dissolved in the glass matrix and diffuse into deeper layers of the sample.

It can obviously be argued that the presented phenomenon is of general interest in the physics of nanocomposite materials. Beyond the already interesting capability to make the glass totally transparent under large areas (restricted only by the size of the anode used) with sharp edges, the underlying physical mechanism is potentially promising for the control of structural, and hence optical properties of metal-doped nanocomposite materials, as will be shown in the following chapters.

In the second part of this chapter dynamics and evolution of the EFAD of spherical silver nanoparticles with exponential profile of volume filling factor of the nanoparticles in glass matrix, as a function of time, voltage and temperature was investigated. The optical extinction band due to nanoparticles' SPR, around 415nm, was measured and Maxwell-Garnett theory was used to fit the extinction spectra. Fitting allowed us to determine the evolution of the thickness of the near-surface layer where nanoparticles' volume filling factor has dropped to zero as a result of bleaching process.

At 280°C , bleaching started with voltage as low as 0.2kV and saturated with time after about one hour. It was found that voltage of at least 1kV and temperature higher than 200°C is required in order to obtain significant and uniform bleaching in the treated area. The results discussed in terms of the underlying electric field assisted dissolution of embedded metal nanoparticles. It was also shown that the dynamics of dissolution is different for treatment at temperatures lower than 280°C , opening up the possibility of gaining control over the dissolution process.

Indeed the nanoparticles' dissolution process was found to be controllable through an appropriate choice of voltage, time and temperature. This feature of the EFAD process will be explored in the following for manipulation of optical properties of silver-doped nanocomposite glass.

Chapter 5: DC Electric field-assisted formation of percolated silver nanolayers inside glass: Observations

5.1.1 Introduction

In the previous chapters it was shown that how a combination of a DC electric field and moderately elevated temperatures to a silver-doped nanocomposite glass could lead to dissolution of the silver nanoparticles in the glass matrix. From a macroscopic point of view, this effect was called “electric field-assisted dissolution” (EFAD). The phenomenon was physically interpreted in terms of ionization of the metal nanoclusters followed by the removal of ions from the clusters and their drift in the depth of the glass substrate.

Here, by using the EFAD technique, it is shown that how the conditions can be selected for which a buried layer of percolated silver clusters is formed several hundred nanometers below the glass surface, giving rise to almost arbitrary colours observable in reflection due to light interference. More generally, it is discussed how this technique could allow engineering of the optical properties of the material via gaining control over the spatial distribution of silver in the glass.

5.1.2 Experimental

For the experiments described in this chapter polydisperse type I-original samples (see chapter 3) were used. The electric-field assisted dissolution of Ag nanoparticles, as described in detail in chapter 4, was done by pressing two electrodes (7mm×9mm size) on the sample surfaces, the anode facing the layer containing nanoparticles. Then the sample was heated to a temperature of ~250°C, and a DC voltage was applied. For the main results presented here, once again the voltage was increased in steps of 0.2 kV to a maximum value of 1 kV within a total time of 50 min, keeping the current below 200 μ A at any time; finally the voltage was disconnected and the temperature was reduced down to the ambient temperature.

5.1.2 Results and synopsis of observations

As it was described earlier the experimental procedure explained in the previous section leads to nearly complete bleaching of the area under the anode. As an example, Fig. 5.1 gives microscopic pictures of a bleached sample; the two pictures, presenting exactly the same sample area (where a corner of the anode was placed), were recorded in reflection (Fig. 5a) and transmission mode (Fig. 5b) of the

microscope (see the figure caption), respectively. In reflection mode the border region shows a rainbow-like pattern consisting of a sequence of several blue, green and red rings. In transmission mode (Fig. 5b), following the same path from untreated (location O) to treated area (location 6) of the sample, no rainbow pattern is observed, but only a gradual change of color from dark brown to faint yellow. The latter colors can be understood by the SP absorption of the silver nanoparticles being present in the sample initially, and their destruction by the dissolution process, governed by the strength of the electric field which quite obviously decreases with increasing distance from the anode edge. The remaining light yellow color within the bleached area indicates that a small amount of silver nanoparticles remains non-dissolved in the depth of the sample where the filling factor of nanoparticles is very low. This incomplete bleaching, as already observed and discussed, is due to the limited applied voltage of 1 kV. An important point here to note is that the bleaching extends slightly outside the electrode area (where the rainbow like pattern is observed).

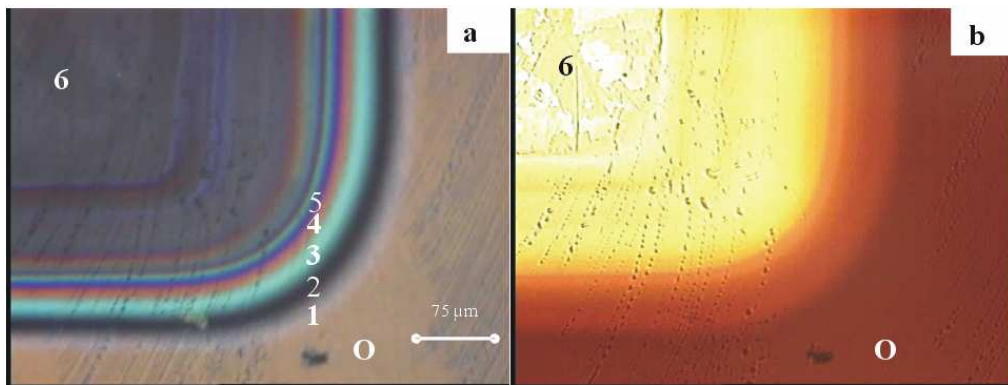


Figure 5.1: Photographs of the segment of the anodic surface of silver nanoparticles containing glass sample after treatment at 1kV, 250°C. Photographs were taken using a microscope spectrophotometer [MPM 800 D/UV, Zeiss] equipped with CCD camera in: (a) reflection and (b) transmission mode. Numbers (2-5) refer to locations where reflection spectra were measured (see Fig. 5.2).

To get an idea about the physical origin of the rainbow pattern, reflection spectra at different positions within the border region were recorded using a microscope spectrophotometer [MPM 800 D/UV, Zeiss], using a rectangular diaphragm of $1\mu\text{m}\times 10\mu\text{m}$. The results are shown in Fig. 5.2, where the individual spectra are labeled along with the numbering of the locations as shown in Fig. 5.1a: at position 2 (in the first, dark blue ring) there is a rather high reflectivity of $R\approx 22\%$ at 380nm wavelength, but quite low reflectivity throughout most of the visible range; in contrast, the broad green ring (no. 3) exhibits a broad band of high reflectivity with a peak of $R\approx 24\%$ at 521 nm. The color of the next, red ring (no. 4) is obviously determined by the broad band of reflectivity around 633nm with $R_{\text{max}}\approx 23\%$, and finally the bright blue ring (no. 5) is characterized by the band around 459nm with maximum reflectivity of $R\approx 17\%$.

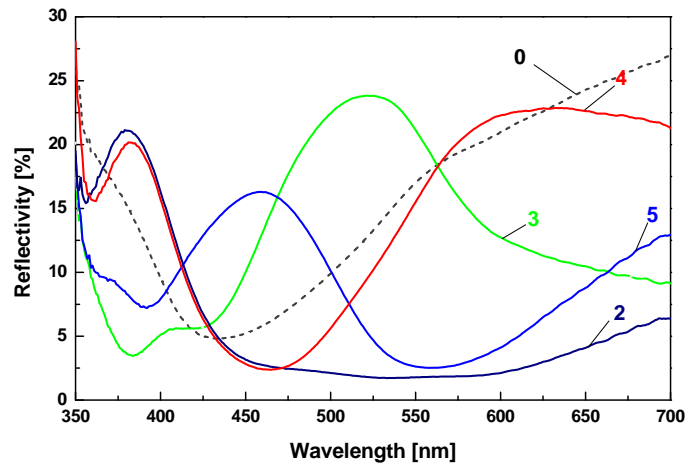


Figure 5.2: Reflection spectra measured at different locations on the sample surface using a microscope spectrophotometer [MPM 800 D/UV, Zeiss]. The reflection spectra are numbered according to different locations shown in fig. 6.1a. For more information refer to the text.

The most reasonable explanation for these spectra (and the whole rainbow pattern) is to assume that, during the dissolution process, an interface with considerable reflectivity in a variable depth of typically a few hundreds of nanometers has been produced and that the depth of the interface depends on the experimental conditions. At this rate the wavelength-dependent constructive or destructive interference between the light reflected at this layer and the light reflected at the sample surface would be the source of reflection spectra, and the different colors would be due to different depths of the interface.

In fact a very simple experiment was performed to check the plausibility of this assumption: if the colors are really due to interference, the rainbow pattern must change dramatically when the phase change by π upon reflection at the sample surface is cancelled by a highly refractive contact liquid dispersed on the sample surface. And in fact, a thin film of CH_2J_2 ($n = 1.74$) provided a dramatic change of the colors observed (Fig. 5.3), whereas a thin film of water ($n = 1.33$), not shown, did not change the pattern at all, only its brightness decreases considerably. The latter is compatible with the decreased reflectivity at the interface sample – liquid, as compared to the interface sample – air.

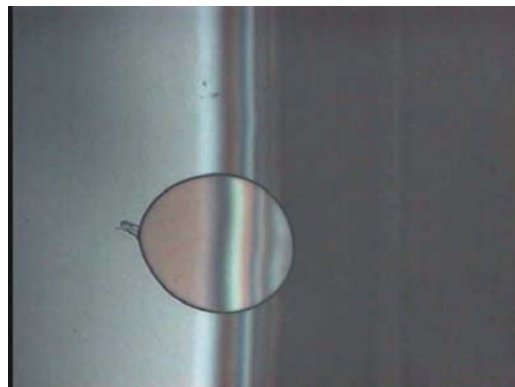


Figure 5.3: A photograph of segment of the sample with CH_2J_2 ($n=1.74$) on. During the experiment an area with small bubble was captured where a dramatic change of the observed pattern can be clearly seen.

While the idea of interference appears to be correct, the nature of the “interferometer” has to be clarified. In particular the following question has to be answered: which type of reflective layer is being produced during the electric field and heat treatment? For this purpose we studied the nanostructural changes in the samples using SEM. Fig. 5.4 shows the border region between modified (left-hand side) and unmodified (right-hand side) regions of a sample which was cleaved along a line crossing these regions; note the different length scales of top view (Fig. 5.4a) and side view (Fig. 5.4b). For both pictures the SEM signal refers to an electron penetration depth of ~ 100 nm, and silver particles appear as white spots.

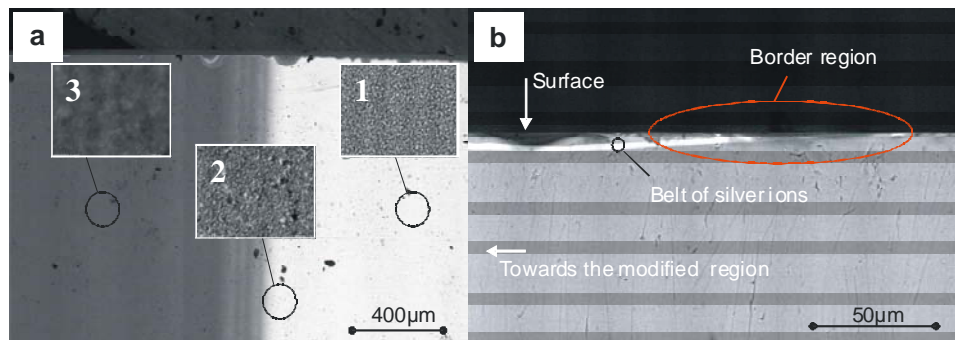


Figure 5.4: a) SEM picture of the surface of the sample taken in back scattered electron (BSE) regime (top view). Insets 1, 2 and 3 refer to locations in untreated region (location O in Fig. 5.1a), border region (location 1 in Fig. 5.1a) and modified region (location 6 in Fig. 5.1a), respectively. b) SEM picture of the cross section of the sample.

In the top view of Fig. 5.4a and the insets, which were taken at higher magnification, it is clearly seen that the originally very high concentration of silver nanoparticles close to the surface (inset-1) starts to decrease in the very border region (inset-2), until in the bleached area no remaining silver nanoparticles can be identified any more (inset-3).

The side view in Fig. 5.4b shows that in the treated area the nanoparticles were destroyed not only in the near surface region, but in the depth of the sample as well. Moreover, a shiny belt can be observed at a depth of approximately $5\mu\text{m}$ from the surface, the distance of this belt to the surface decreasing towards the border region. Silver ions, which were ejected from the nanoparticles during the dissolution process and drifted away in the depth, are at the origin of this belt, which could act as a buried reflective layer because of the depth gradient of ion concentration. In the second part of this chapter this aspect will be discussed in detail.

Fig. 5.5 gives the definitive proof of the interferential origin of the observed phenomenon and exhibits the nature of the buried reflective layer: in the central part of the microscope pictures of the original rainbow area (left, narrow part) and of the same region after the removal of a number of very thin surface layers by etching of the sample in 12% HF acid are shown. Clearly the rainbow pattern has changed dramatically due to the removal of surface layers. At the position indicated by white circles (green ring, location 3 in Fig. 5.1a) the sample was carefully examined by SEM before etching and after each etching step. At an etched depth of approximately

400nm a layer containing densely-packed percolated silver islands was observed (Fig. 5.5a).

Etching of a slightly deeper layer revealed that the silver filling factor is still very high in the depth (Fig. 5.5b). For comparison Fig. 5.5c shows the SEM picture taken from the very surface of the examined green region before etching, demonstrating again that the Ag particles close to the surface have been completely destroyed there. As it will be discussed later, this buried layer of densely-packed percolated silver clusters should, in principle, provide the reflectivity needed to observe, via interference, the rainbow colors in the border region.

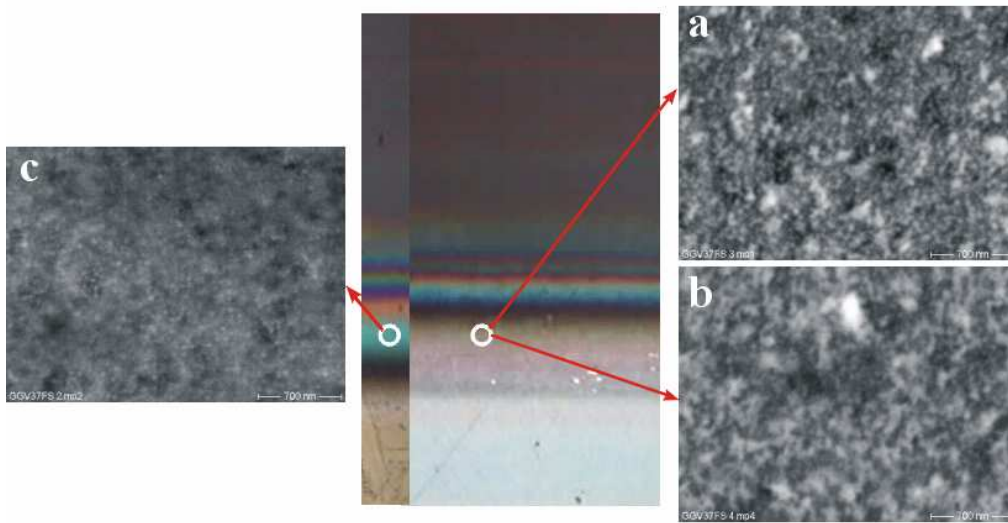


Figure 5.5: SEM pictures taken from the location of the first green ring (location 3 in fig. 5.1a). Pictures a and b were taken after successive etching of the sample surface up to depths of approximately 400nm. Picture c is presented for comparison and shows the surface of the sample before etching. The picture in the middle shows a segment of the border region of the sample before and after etching.

To the best of the author's knowledge, there is no closed description for the optical properties of percolated silver films up to now. Thus the brief discussion here is restricted to a plausibility check of the interface reflectivity. Generally speaking, percolated silver films represent an intermediate state between the limits (i) isolated nanoparticles and (ii) compact metallic film. The latter has, in case of silver, high reflectivity ($R > 95\%$) throughout the visible range, caused by a very low refractive index ($n \approx 0.05$) and strong absorption. Owing to the pertinent low penetration depth of typically 10 nm, silver films can be described by their bulk properties – e.g., maximum reflectivity – already for film thickness of ≈ 20 nm and above [5.6]. However, as it was described earlier (see chapter 2 and 3), the optical properties of isolated metal nanoparticles, representing the other limit, can often, up to quite high metal content, reasonably well be described using Maxwell-Garnett theory [5.1-5.4]. Based on this description, the complex refractive index of a composite medium with dielectric constant $\epsilon_{eff}(\omega)$ can be expressed as:

$$n_{eff}(\omega) = \sqrt{\epsilon_{eff}(\omega)}. \quad (5.1)$$

Using Eqs. (2.10), (3.3), (3.4) and the parameters $\epsilon_h = 2.3$, $\omega_p = 9.2$ eV, $\gamma = 0.5$ eV, $\epsilon_b = 4.2$, (see chapter 2 and 3), the optical constants $n(\omega)$, $k(\omega)$ of glass with spherical silver nanoparticles were calculated as a function of the volume filling factor of metal clusters in the glass matrix. Finally, Fresnel's formulae were applied to determine the reflectivity of an interface of the nanocomposite to the pure transparent matrix material (here glass with $n = 1.5$). The results of the calculation are shown in Fig. 5.6.

As it can easily be seen from Fig. 5.6, there is a strong dependence of reflectivity on the Ag filling factor, which influences both the real and imaginary parts of the effective refractive index of Maxwell-Garnett composite glass. At low filling factor ($f \leq 10^{-2}$) the reflectivity is negligible ($R_{\max} \approx 10^{-3}$), while at quite high filling factor of $f \approx 0.3$ the required reflectivity $R \geq 20\%$ is achieved throughout the visible range. However at such high filling factors the Maxwell Garnett model is no longer a very accurate description of the optical properties, in particular not for the case of early-stage percolation as observed for the buried layers in this work. So it makes no real sense to try to simulate the observed interference spectra on the basis of this too simple model, although some qualitative agreement can be achieved assuming depths of 100 to 400 nm for the buried layer.

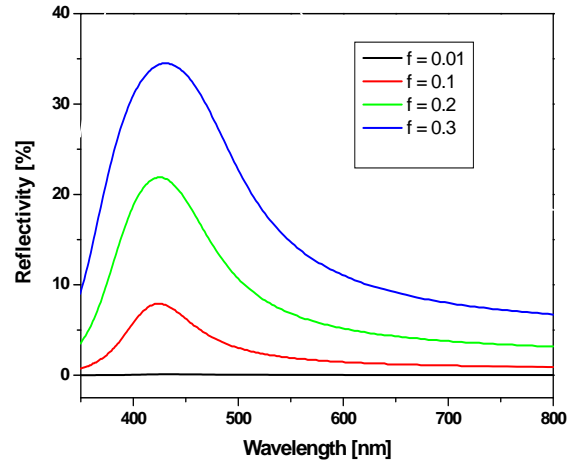


Figure 5.6: Calculated reflectivity for interface between Maxwell-Garnett silver in glass nanocomposite and neat glass, with fill factor f as parameter

On the other hand these simple considerations allow us to draw the important conclusion that already a rather thin layer of only a few tens of nanometers with relatively high silver content will definitely be able to provide the reflectivity needed to explain the reflection spectra observed by interference.

Based on the above observations the buried layer close to the border region is created due to the following mechanism: the combination of DC electric field and temperature at first induces destruction of silver nanoparticles at the upper layer close to the surface of the sample. Further treatment, i.e. increase of the applied voltage, results in the drift of silver cations in the depth of the sample, and simultaneously electrons are attracted towards the anode, in the opposite direction of the cation movement. So at some depth the electrons may neutralize the cations again, thereby increasing the silver concentration there, which can lead to percolation and production of a layer containing densely-packed percolated silver clusters. The threshold of the dissolution process depends strongly on the filling factor of the nanoclusters (See chapter 4).

Thus, the magnitude of the voltage applied to a sample with a gradient of the nanoparticle filling factor defines the distance between the surface and the buried layer of percolated silver clusters. This layer, finally, acquires a reflectivity that is high enough to observe interference of light reflected at the sample surface and at the buried layer. Since, in the border region the applied electric field – and thus the depth of this reflective layer – is non-uniform, rainbow-like patterns can be observed there.

At this point the obvious question occurs whether similar experiments are possible, in which the experimental parameters such as electric field, temperature and processing time are chosen so that a larger homogeneous area of interference is produced, and hence a uniformly colored region. For this purpose some preliminary experiments were conducted, where DC voltages of 200 V, 400 V, and 600 V were applied at $\sim 250^{\circ}\text{C}$ in one step, for a total time of 30 min; electrodes with an area of $1\text{ mm}\times 2\text{ mm}$ were used. Due to imperfect contact (See chapter 4) not the whole regions under the electrodes were homogeneously colored, but at least areas with dimensions of several $100\ \mu\text{m}$ were produced which appear predominately in blue, green and red. In Fig. 5.7 two pictures show the edges of the green and red regions produced.

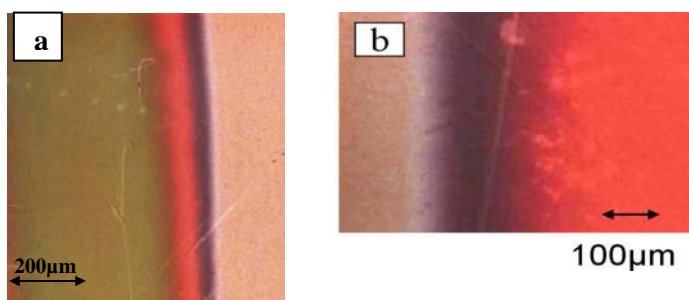


Figure 5.7: Preliminary results showing large-area coloration through electric-field-assisted production of a buried percolated silver layer; processing at (a) 400V and (b) 600V.

For further analysis a sample which was exhibited large green area (Fig. 5.7a) was cleaved and its cross section was then subjected to SEM examination. Fig. 5.8a shows the results. The buried layer responsible for the green colour in this sample can be identified. The distance between this layer and surface of the sample was estimated from the SEM to be $\sim 500\text{nm}$. For comparison Fig. 5.8b shows the cross section of untreated (original) region of the sample (polydisperse type I-original).

Once again it can be clearly seen that the described treatment results in dissolution of silver nanoparticles starting from the very surface of the sample and down to a particular depth (here $\sim 480\text{nm}$) depending on the magnitude of the applied voltage.

The last remark which has to be pointed out is that the size of the produced monochromatic area in each case was only limited by the size of the electrodes used providing that there is a good contact between the sample and anode. This obviously requires good quality of both surface of the sample and the electrodes used. This requirement is in fact put an upper limit on scalability of the described technique.

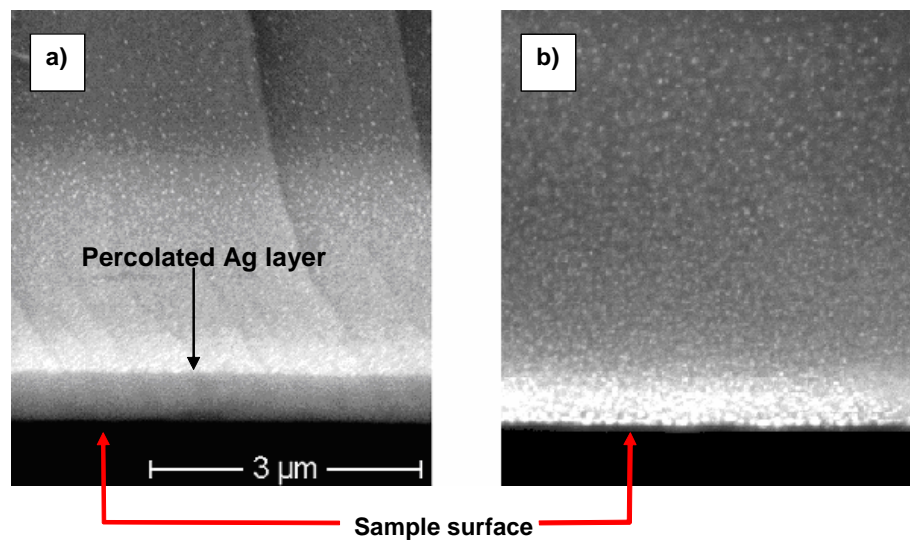


Figure 5.8: a) SEM picture taken from the cross section of the sample exhibiting large green area. b) Shows the cross section of the original (untreated) area of the same sample.

Now that the main experimental achievements were presented and a synopsis of the results was given, it is the time to introduce a more accurate model for description of the interference spectra.

5.2 DC Electric field-assisted formation of percolated silver nanolayers inside glass: Characterizations

5.2.1 Introduction

Here, following the results presented in the previous part, the optical characterization of silver-doped glasses subjected to electric field-assisted dissolution of nanoparticles is presented. The characterization is performed by means of fitting of the spectrophotometric measurements.* The optical properties of the investigated samples are described in terms of the interference between the light reflected from the glass surface and the light reflected from a silver-containing layer formed in the depths of the glass.

The analysis of the data reveals the porosity of the glass in the region where nanoparticles are dissolved, that can be attributed to the presence of residual nanopores. The procedure starts by employing a simple model to represent the physical structure of the samples. The complexity of the model then increases until a satisfactory description of the experimental data is achieved. This approach allows determining the critical parameters that control the optical properties of the buried silver-containing layer as well as the glass region where the nanoparticles are dissolved.

5.2.1 Model

As it was said earlier, due to the changes in the structural properties of the samples, the coloration observed in reflection can be easily understood in terms of interference between the light reflected from the glass surface and the light reflected from the buried silver-containing layer. Depending on the intensity of the applied electric field, this layer will be formed at different depths, changing the interference condition of maxima and minima and giving place to a different coloration. Thus, in the border region, due to the gradient of the electric field intensity, there will be a depth-gradient of the silver-containing layer, originating a continuous variation of the coloration (rainbow-like pattern). Partial bleaching of the sample, as was discussed earlier, can be attributed to the fading of the associated surface plasmon absorption due to the dissolution of nanoparticles. The aim at this point is to find a physical model for the treated regions that can explain the observed coloration. The reliability of the model will be checked by fitting the measured reflectance spectra, since the

* Fitting of the experimentally measured spectra were performed by Dr. Sancho-Parramon using NKDSsoftware [5.7].

measured transmission is very low due to the surface plasmon absorption of the remaining nanoparticles and hence does not provide significant quantitative information.

In order to simulate the measured reflectance spectra, it is necessary to determine the reflectivity of the buried silver-containing layer and therefore it is indispensable to establish an appropriate model for the description of its optical constants. A widely exercised approach for modelling the optical properties of composite media is via the effective medium theories, namely Maxwell-Garnett theory (MGT) and Bruggeman effective medium approximation (BEMA). Since the optical behaviour observed in the reflectance spectra is dominated by interferential effects, in order to reproduce the experimental data it is necessary to use calculations for the propagation of light in stratified media.

For the calculations general-purpose software for the optical characterization of multilayer stacks, namely NKDSsoftware [5.7], is used. This software allows defining a multilayer structure where each layer is described by few parameters: typically, its thickness and a variable number of parameters accounting for the dispersion of the optical constants of the layer material. In this way, the optical behaviour of the sample is completely represented with a set of parameters, whose optimal value can be found by the minimisation of the ξ^2 merit function defined as:

$$\xi^2(P_1, P_2, \dots, P_{N_p}) = \frac{1}{n_{meas} - N_p - 1} \sum_{i=1}^{n_{meas}} \left[\frac{y_i - y(x_i; P_1, P_2, \dots, P_{N_p})}{\sigma_i} \right]^2, \quad (5.2)$$

where n_{meas} is the number of measured points, y_i are the experimental data measured at the wavelength x_i , and σ_i are the associated experimental measurement errors. P_1, P_2, \dots, P_{N_p} are the N_p parameters defining the sample and $y(x_i, \dots, P_1, P_2, \dots, P_{N_p})$ are the data calculated with standard algorithms for computing the optical properties of multilayer structures [5.8, 5.9].

The software presents some particular features, as the possibility to use different effective medium approximations for representing layers made up of mixtures of materials. It also allows accounting for in-depth inhomogeneity of the refractive index within the layers, assuming different mathematical profiles for the variation of the refractive index through the layer thickness.

5.2.2 Characterization of the large coloured areas

In this Section the results of modelling of the optical properties of the regions where the electrodes were placed are presented. The attention is focused on a sample where the green colour in reflection was observed (Fig. 5.7a). As previously mentioned, the SEM cross view of the treated area (Fig. 5.8a) evidenced dissolution of the silver nanoparticles in a region of approximately 500 nm and formation of a thin buried silver-containing layer at this depth. The presence of none-dissolved nanoparticles at deeper regions of the glass can also be observed.

According to the SEM picture, the simplest multilayer model that could describe the optical behaviour of the sample would be a 2-layer structure: a glass surface layer where nanoparticles were dissolved and the buried silver-containing layer. The rest

of the glass would only play the role of substrate, thick enough to neglect interferential effects. Fig. 5.9 shows a schematic diagram of the model.

In order to describe the glass surface layer and the glass substrate, their optical constants are fixed to those found in literature for soda-lime glass. At this stage the effect of the none-dissolved nanoparticles in the glass substrate are neglected due to the very low filling factor. It was assumed that the buried silver-containing layer is a mixture of glass and silver (with optical constants for the silver taken from the literature [5.10]) and its optical constants is modelled using the effective medium theories. Thus, the first model requires a total of 3 parameters: the thickness of the glass surface layer (d_{glass}), the thickness of the buried silver-containing layer ($d_{Ag-glass}$) and the filling factor of silver in the buried silver-containing layer (f_{Ag}).

If the MGT is used to represent the optical properties of the buried silver containing layer, the achieved fitting of the data reaches a value of the merit function of $\chi^2=16.8$, with the following values of the optimized parameters: $d_{glass} = 546$ nm, $d_{Ag-glass} = 83$ nm and $f_{Ag} = 0.05$. However, if the BEMA is used, a significantly better fitting is obtained ($\chi^2=5.4$) with the parameter values $d_{glass} = 547$ nm, $d_{Ag-glass} = 29$ nm and $f_{Ag} = 0.14$. Figure 5.10 contains the fit achieved using the BEMA for the buried silver-containing layer (See red line).

A simple observation of the simulation obtained with the previous modelling reveals that the discrepancies between the computation and the experimental data are mainly found in the values of the maxima and minima of the spectra, while the position of the fringes is well tuned. Typically, such discrepancies are related to an in-depth inhomogeneity of the refractive index of the layers [5.11]. In chapter 4 a plausible explanation proposed which could describe such inhomogeneity, plain-view SEM pictures of the modified area suggested the presence of hole-like structures in the region where nanoparticles were dissolved (Fig. 4.5).

In this way, this region may have a notable porosity that would lower the refractive index of the glass. However, since the pores would be originated by the dissolution of nanoparticles and nanoparticles were embedded at a distance of a few tens of nanometer from the glass surface, the very surface of the glass would be compact. In this case, a more realistic model for the sample would be represented by a 3-layer structure on a glass substrate: a very thin layer of compact glass, a porous glass layer (where the nanoparticles were embedded in the initial sample), and the buried silver-containing layer. Fig. 5.11 shows a schematic diagram of the model.



Figure 5.9: Schematic diagram of the 2-layer model.

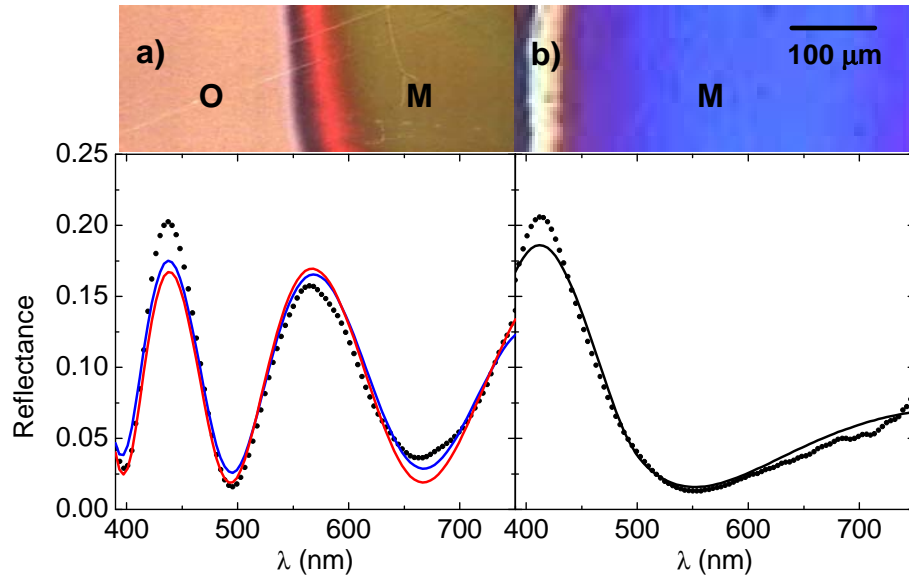


Figure 5.10: **a)** Measured reflectance spectra of the area showing a green coloration (dots) together with the fits assuming: i) a 2-layer model (Fig. 5.9): glass layer and BEMA silver-containing glass layer (red line) and ii) a 3-layer model (Fig. 5.11): glass layer, homogeneous porous glass layer and BEMA silver containing layer (blue solid line). **b)** Measured reflectance spectra of the area showing a blue coloration (dots) together with the fit assuming a 3-layer model: glass layer, inhomogeneous porous glass layer with a pore concentration equal to the original distribution of silver nanoparticles and BEMA silver containing layer (solid line).

The optical constants of the porous layer can be represented using effective medium approaches, considering a mixture of glass and voids. Furthermore, we shall primarily assume that the concentration of pores will be the same as the concentration of silver nanoparticles in the untreated sample. As far as the silver filling factor near the surface varies approximately as (see Fig. 3.1b):

$$f(x) = 0.7 - 0.6x, \quad (5.3)$$

where x is the glass depth in microns.

The thickness-dependence of the refractive-index of this layer is implemented dividing the layer in a fixed number of sub-layers of equal thickness. Each sub-layer is modelled with the BEMA, with a pore concentration calculated according Eq. 5.3. Now the model of the sample requires 4 parameters: the thicknesses of the 3 considered layers (d_{glass} , $d_{porous-glass}$, $d_{Ag-glass}$) and the filling factor of silver in the buried layer (f_{Ag}). This model enables a significant improvement of the description of the data, as the merit function reduces to 3.92. The values of the optimized parameters are: $d_{glass}=30$ nm, $d_{porous-glass}=619$ nm, $d_{Ag-glass}=28$ nm and $f_{Ag} = 0.1$. Similar results are achieved if the MGT is employed. This is due to the fact that glass and voids both have relatively similar optical constants (specially, compared to the difference between the optical constants of silver and glass) both theories lead to similar results [5.12].

Even though a significant improvement in the description of the data was obtained, our primer assumption that the porosity in the treated sample exactly follows the filling factor distribution of silver nanoparticles in the untreated sample may be rough; as it neglects the possible collapse of the pores once the silver is dissolved.

In this sense, it seems necessary to check if another value of the pore concentration can lead to a significantly better data fitting. For this reason, we shall now consider the pore concentration as another parameter which has to be optimized. In order to avoid an excessive number of parameters, a constant homogeneous concentration of pores through the layer where nanoparticles are dissolved, is assumed. This parameter is defined by the pore concentration f_{pores} .

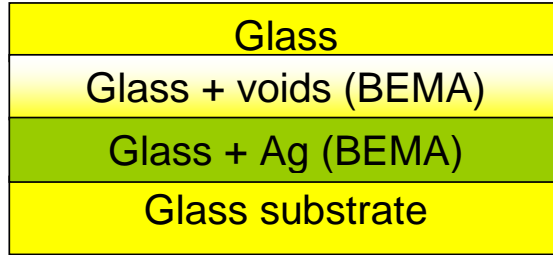


Figure 5.11: Schematic diagram of the 3-layer model.

Therefore, a total of 5 parameters will define the sample (d_{glass} , $d_{porous-glass}$, $d_{Ag-glass}$, f_{Ag} , f_{pores}). Using this modelling, a slight improvement of the data is reached ($\chi^2=3.2$), with the parameter values: $d_{glass} = 39$ nm, $d_{porous-glass} = 570$ nm, $d_{Ag-glass} = 23$ nm, $f_{Ag} = 0.1$, $f_{pores} = 0.29$. This concentration of pores is lower than the average concentration of silver in the original sample in the same thickness (~ 0.5). The fitting of the data using this model is shown in Fig. 5.10a by blue line.

In order to assess the validity of the model, it was also applied to the sample where a blue coloration was observed via application of 0.2kV). Once more it was assumed that the pore concentration follows the original distribution of silver nanoparticles. A good fitting of the data is obtained, with a value of the merit function of 1.3. The value of the optimized parameters is $d_{glass} = 39$ nm, $d_{porous-glass} = 279$ nm, $d_{Ag-glass} = 19$ nm and $f_{Ag} = 0.02$.

Fig. 5.10b shows the reflectance spectra for this sample, evidencing the good agreement between the simulation and the experimental data. Similarly to the analysis of the green coloured sample, it was also checked if another value of the pore concentration could lead to a better fitting of the data. With the pore concentration as a free parameter, the merit function decreases only to 1.29, with the parameter values $d_{glass} = 42$ nm, $d_{porous-glass} = 272$ nm, $d_{Ag-glass} = 17$ nm, $f_{Ag} = 0.01$, $f_{pores} = 0.67$. In this case, the pore concentration is closer to the average filling factor of silver in the original sample in the same thickness (~ 0.6).

A summary to what was said so far would contain the assessment on the initial qualitative explanation for the observed coloration of the treated samples: the interference between the light reflected at the glass surface and the light reflected in a thin layer containing silver. Such layer can be well modelled as a mixture of glass and silver within the BEMA, rather than with the MGT. Furthermore, the refinement of the data fitting reveals the presence of pores that was already suggested by previous SEM observations which seems to be originated via the dissolution processes

5.2.3 Characterization of the border region

Here the aim is to extend the obtained model to the border region of the sample where the rainbow-like pattern was observed. It is done due to the fact that the phenomenon has the same physical origin. The reflection spectra presented in Fig. 5.2 were fitted using the model consisting of 3 layers (compact glass layer, porous glass layer, silver containing layer). It is assumed that the porous layer is homogeneous, and the pore concentration as a parameter which has to be optimized. Furthermore, it is impose that the compact glass layer will have the same thickness for the fitting of all the spectra, allowing a reduction of the total number of necessary parameters.

The results of the data fitting using this modelling are summarised in Table 5.1. While the description of the light blue and red spectra is quite good, the fits for the green and dark blue spectra are rather unsatisfactory, as indicated by the obtained values of the merit function. The fittings of these locations become even worse if in order to simulate the distribution of pores in the rainbow area the original distribution of silver is considered.

The most suitable explanation for the failure of the model in describing of the two last spectra is that they are taken in the regions very close to the untreated area. Therefore, one can expect that the effective DC electric field is significantly lower than under the electrodes area and that the depth of the buried silver-containing layer should be smaller. In this case, there might be a strong influence of the none-dissolved nanoparticles, situated beneath the buried layer and in the depth of the glass.

Spectra	d_{glass} (nm)	$d_{\text{porous-glass}}$ (nm)	f_{pores}	$d_{\text{Ag-glass}}$ (nm)	f_{Ag}	ξ^2
Light blue (4)		238	0.1	27	0.11	1.17
Red (3)	44	198	0.54	34	0.09	0.97
Green (2)		137	0.46	60	0.04	6.80
Dark blue (1)		25	0	35	0.2	3.4

Table 5.1: Value of the optimised parameters resulting from the reflectance fitting of the different locations of the border region area using a 3-layer model (glass layer, porous glass layer, BEMA silver containing layer).

In fact, the SEM pictures of the border region of the sample have already revealed the presence of none-dissolved nanoparticles (See Fig. 5.4a). To account for these remaining nanoparticles, it is assumed that beneath the buried layer there is a gradient of silver nanoparticles, with a filling factor that decreases linearly from a maximum value f_L to zero within a certain thickness $d_{\text{Ag-nano}}$:

$$f(x) = -\frac{f_L}{d_{\text{Ag-nano}}}x + f_L. \quad (5.4)$$

According to the initial distribution of the nanoparticles, an exponential variation of the silver filling factor would be more appropriate; however the linear model is simpler and would allow us to check easily the role of the remaining none-dissolved nanoparticles.

Thus, the model for the border region will consist now on a 4-layer structure: the surface glass layer, the porous glass layer, the buried silver-containing layer and the layer with a linear filling-factor gradient of remaining none-dissolved nanoparticles. A schematic diagram of this model is presented in Fig. 5.12.

The gradient of this layer is implemented by dividing the layer in a fixed number of sub-layers of equal thickness and calculating the filling factor of silver nanoparticles for each sub-layer according to Eq. 5.4. However, now the effective optical constants of the sub-layers are calculated using the MGT, since it is more appropriate for the topology of none-dissolved nanoparticles. In this model two more parameters which both have to be optimised are introduced: the thickness of the layer containing none-dissolved nanoparticles ($d_{Ag-nano}$) and its maximum filling factor (f_L).

With this model, the fittings of the green and dark blue spectra are significantly improved, as listed in Table 5.2, together with the value of the optimized parameters. The fits of the spectra of the rainbow-like region are shown in Fig. 5.13. It has to be pointed out that the remaining none-dissolved nanoparticles do not have significant weight neither in the other spectra of the border region or in the coloration of the treated areas.

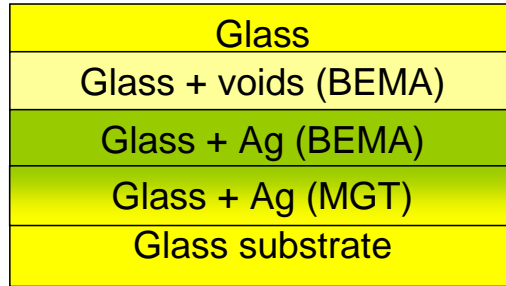


Figure 5.12: A schematic representation of the 4-layer model.

Spectra	d_{glass} (nm)	$d_{porous-glass}$ (nm)	f_{pores}	$d_{Ag-glass}$ (nm)	f_{Ag}	$d_{Ag-nano}$ (nm)	f_L	ξ^2
Light blue (4)	45	242	0.12	25	0.10	-	$<10^{-5}$	1.15
Red (3)		191	0.48	38	0.08	-	$<10^{-5}$	0.96
Green (2)		124	0.53	41	0.02	768	0.09	0.80
Dark blue (1)		14	0.78	0	0	690	0.12	1.85

Table 5.2: Value of the optimised parameters resulting from the reflectance fitting of the different locations of the border region using a 4-layer model (glass layer, porous glass layer, BEMA silver containing layer and inhomogeneous MGT layer with silver nanoparticles).

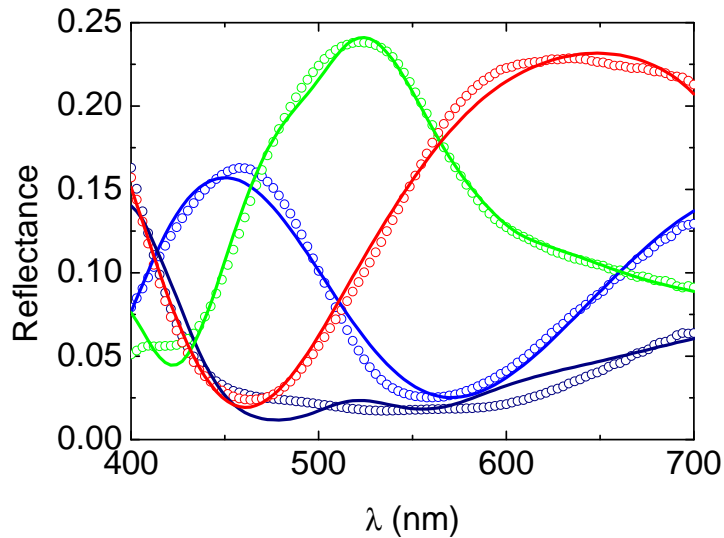


Figure 5.13: Measured reflectance spectra of the different locations of the border region (dots) together with the fits assuming a 4-layer model: glass layer, homogeneous porous glass layer, BEMA silver containing layer and inhomogeneous MGT layer with silver nanoparticles (solid line). The different locations in the Figure are indicated by different colors.

5.3 Discussion

The use of interferential calculations for the description of the experimental measurements is very satisfactory, assessing the qualitative explanations proposed earlier to describe the modification of the optical properties of the samples. Thus, the buried silver-containing layer seems to be responsible for the observed phenomenon. It is found that the buried silver-containing layer is better described within the frame of the BEMA than the MGT. It was assumed that such layer is formed by the aggregation of silver ions in heterogeneous clusters from the dissolved silver nanoparticles, with a possible interconnection among clusters (percolation), and hence the picture agrees better with the BEMA assumptions than with the MGT. From a numerical point of view, the BEMA provides the buried layer with a rather high absorption (and thus, reflectivity) through the whole visible spectral range (as we observe experimentally), while the MGT can only give a significant reflectivity in a narrow region around the surface plasmon resonance (centred approximately at 400 nm). The comparison between the MGT and BEMA is only shown for the simplest model (the 2-layer model consisting of a compact glass layer and the buried silver containing layer), but as it was checked for all the other tested models the BEMA gives significantly better fittings than the MGT, with merit functions approximately 3 times smaller.

The depth of the buried silver-containing layer resulting from the fittings (given by the sum of the parameters d_{glass} and $d_{porous-glass}$) is in a fair agreement with the values determined by SEM for the sample exhibiting green coloration (~ 500 nm, with a resolution of several tens of nanometers). The depth of this layer for the sample exhibiting blue coloration is smaller; around 300 nm what can be expected due to the applied DC voltage was lower for this sample. The thickness of the buried layer can not be well estimated from the SEM pictures, indicating that it should have a value around a few tens of nanometers, what agrees with the obtained values for all the

tested models. The thickness and the silver concentration of the buried layer is lower for the blue coloured sample than for the green one, as can be expected from the experimental conditions: the lower the applied voltage, the lower the total amount of silver that will be dissolved and form part of the buried layer.

In any case, the filling factor of silver in this layer seems to be low if compared with the high concentration of silver that is suggested by the SEM images. The values found by the data fitting refer exclusively to metallic silver (i.e: silver with a “metallic” optical behaviour). The dissolution of nanoparticles is produced via the ionization of silver and therefore the silver that is present in the buried layer could be mainly in the form of cations, undistinguishable from metallic silver by SEM. Silver cations do not play an important role in the optical properties of glass in the visible spectral range [5.13]. Hence, it can be assumed that the presence of the silver ions do not substantially modify the optical constants of the glass, especially if compared with the effect of metallic silver.

In fact, the required concentration of silver which has to be achieved in order to observe the reflectance can be roughly estimated from the following expression [5.14]:

$$R = \frac{R_1 + R_2 + 2\sqrt{R_1 R_2}}{1 + R_1 R_2 + 2\sqrt{R_1 R_2}}. \quad (5.5)$$

This equation relates the maximum reflectivity (R) of a single dielectric layer on an absorbing (metallic) substrate, being R_1 and R_2 the reflectivity of the air-dielectric and dielectric-metal interfaces, respectively. Thus, assuming a refractive index of 1.5 for the glass, in order to obtain a value of $R = 20\%$ (maximum values observed in the experimental spectra), a value of $R_2 \sim 10\%$ is required. This value can be achieved in the visible spectral range with a silver filling factor of $\sim 10\%$ using the effective medium theories. Since the refractive index of the glass is actually lower due to the porosity, the filling factor of silver can be even lower to reach the same value of R .

The refinement of the data fitting reveals that the glass beneath the surface should have a lower refractive index that can be explained by the presence of nanopores originated by the dissolution of silver nanoparticles. The assumption that the distribution of pores follows the filling factor distribution of silver nanoparticles in the original sample enabled us to achieve a fairly good description of the data. By considering a different pore concentration only led to a slightly better fitting for measurements of the green coloured sample. This particular result suggests a lower pore concentration. This could be understood in terms of a partial collapsing of pores. This phenomenon may depend on the treatment conditions, since no improvement was achieved in the case of the blue coloured sample. More complex mathematical models for the distribution of pores were also tested; however, they only led either to the same results or to physically meaningless results. In any case, the confirmation of the presence and distribution of pores will be the subject of future research.

The extension of the model to the description of the optical behaviour of the border region is partially satisfactory. While the spectra of the border region closer to the treated area can be successfully fitted, the model scarcely describes the spectra

measured in locations close to the untreated area. However, if the contribution of the remaining none-dissolved nanoparticles is taken into account (through a linear gradient of filling factor of nanoparticles in the depth of the glass), the measured spectra can be remarkably reproduced. It has to be pointed out that the contribution of the gradient of none-dissolved nanoparticles was not able to improve the fitting of the light blue and red spectra of the border regions. Actually, looking at the value of the parameters, one can observe that the gradient starts at a maximum value of 12% of Ag nanoparticles for the dark blue spectra and at 9% for the green one. Therefore, we can expect that it would have even lower values for the spectra of the border region taken closer to the treated area and, consequently, a very weak weight in the reflectance spectra.

From the value of the optimised parameters (Tab. 5.2), it can be established that the depth of the buried silver-containing layer diminishes as the spectra correspond to locations approaching to the untreated area. This result can be expected from the lowering of intensity of the DC electric field in the border region. The concentration of pores also increases in the same direction, suggesting that the pores are inhomogeneously distributed and mainly concentrated in a region very close to the surface, as expected from the distribution of silver in the original sample. Nevertheless, the considered value for the pore concentration is lower than the average filling factor of silver in the original sample, once again indicating the possibility of a partial collapse of pores after the dissolution of silver. The total amount of silver in the buried layer (estimated by the product of layer thickness and silver concentration) decreases for the spectra closer to the untreated area. This behaviour suggests that the buried silver layer can be hardly defined for the locations close to the untreated area. In fact, for the dark blue spectra, the presence of this layer is overlooked by the optimisation procedure. Therefore, the interference effects in the border region closer to the untreated area seem to be originated by the remaining none-dissolved nanoparticles, rather than by the buried silver-containing layer.

A typical problem in the optical characterization of materials is the use of a large number of parameters that can lead to numerically good solutions but lacking of physical sense. Here the procedure started with a very simple model and test more complex models in successive steps, according to the information provided by the structural characterization of the sample. The improvement in the modelling is evaluated by the reduction of the values of the merit function. In this way, the possible use of an excessive number of parameters that do not allow a noteworthy improvement in the description of the experimental data was avoided.

5.4 Summary

In the first part of this chapter by applying an intense DC electric field at $\leq 250^{\circ}\text{C}$ to a glass containing silver nanoparticles in a thin surface layer of a few microns, a buried layer of percolated silver clusters with modified optical properties was produced. The buried layer was located in the border region between the treated and untreated regions of the sample. Reflection of light from the buried layer and its interference with the light reflected from the surface of the glass is thought to be responsible for the observed rainbow-like pattern.

Scaling of this technique via varying the applied voltage resulted in production of large areas which show homogeneous colors in reflection. In each case the distance between the produced buried layer and the surface of the sample was strongly dependent on the magnitude of the voltage applied. Once again reflection of light from the buried layer and its interference with the light reflected from the surface of the glass is believed to be responsible for the observed spectra in each case.

In the second part fitting of the measured spectra revealed that the observed optical behaviour can indeed be successfully explained in terms of interferential calculations. Furthermore, the fitting procedure allows establishing what parameters determine the coloration. Thus, the buried layer seems to have a thickness of a few tens of nanometers, with a 10% content of metallic silver that can be well described within the BEMA. The fitting of the data also suggests the presence of pores beneath the glass surface that can be formed by the dissolution of silver nanoparticles. The coloration observed in the border region can also be explained with this model, although the interferences for the spectra measured in locations closer to the untreated area originate from the light reflected by the region with none-dissolved nanoparticles in the depth of the glass.

Further thorough studies of the threshold and intermediate conditions as well as dynamics of the process are needed; this will be a subject of future work. What is clear, however, is the potential offered by this simple technique to produce, based on metal-doped nanocomposite glasses, devices with a need for wavelength selection.

Chapter 6: Metallodielectric 2D structures made by DC electric field microstructuring of nanocomposite glasses

6.1 Introduction

During the experiments presented in chapter 4, it was found that the EFAD technique allows producing micrometer-scale optical structures, as it is shown by the dark horizontal lines on the right-hand side of Fig. 6.1. The image is the reproduction of a microscope picture; the left part gives a $10\mu\text{m}$ scale photographed with the same magnification. The dark lines, which clearly have a thickness of $\leq 1\mu\text{m}$ were produced by simply making scratches in the steel anode with a diamond marker before the EFAD procedure, and then pressing the electrode with the scratched side on the glass surface containing silver particles. After the treatment, the whole area under the anode was transparent, with the exception of the scratches, where obviously the Ag particles have not been destructed.

This result served as a main hint and source of encouragement to conduct series of experiments towards capability study of the EFAD technique for fine optical structuring in the silver-doped nanocomposite glasses. This chapter is in fact devoted to these studies.

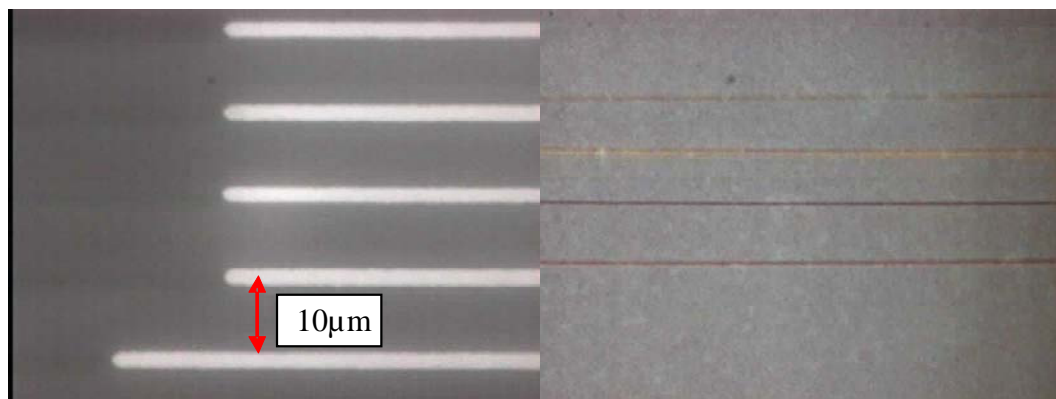


Figure 6.1: Microscopic photography of sub-micrometer lines made by EFAD using an electrode scratched with a diamond marker (right-hand side); left-hand side: calibrated length scale with same magnification.

6.2 Experimental

The polydisperse type I-original samples (see chapter 3) were used for all of the experiments described here. Experiments were performed by equipping the samples with two electrodes pressed on the surfaces, the anode facing the layer containing nanoparticles. While plain steel electrodes (10mm×10mm), served as cathode, as anode structured electrodes were used. Samples were then placed in oven and heated to a temperature of ~250°C; then a DC voltage of 0.6 kV (in steps of 0.2 kV) was applied in each case. The total time of treatment of each sample was approximately 30min. Finally voltage disconnected and temperature reduced down to the ambient temperature.

For the experiments described in this chapter four different structured electrodes were used: a) *macroporous silicon*, b) *nanoporous silicon*, c) *microline electrode* and d) *nanoline electrode*.

- a) *Macroporous silicon*: macroporous silicon was grown via a photoelectrochemical etching process of lithographically prestructured <100> oriented n-type silicon wafer. The front side of the wafer was in contact with hydrofluoric acid (HF; cHF=5wt.%; T=10°C) whereas the backside was illuminated generating electron-hole pairs. An external anodic bias consumes the electrons and the electron holes diffuse through the whole wafer to silicon electrolyte interface promoting the silicon dissolution there. The pores with very flat surfaces and high aspect ratios grow straight along the <001> direction of the silicon single crystal. Excellent reviews of the preparation technique can be found in Ref. 6.1 and 6.2. The structured anode (15mm×15mm) used here had a squared lattice of pores (holes) with a lattice constant of 2µm and wall thickness of ~1µm and was sputtered with 10nm chromium film. The sputtering of chromium film prevented silicon-glass anodic bonding during the experiment [6.3, 6.4]. Fig. 6.2a shows a photo of a segment of this electrode taken in transmission mode of a microscope spectrophotometer [MPM 800 D/UV, Zeiss] equipped with a CCD camera, while Fig. 6.2b shows a SEM view of the electrode.
- b) *Nanoporous silicon*: preparation technique of the nanoporous silicon was the same as the microporous silicon. However, here the lattice constant was 500nm and once again the electrode was sputtered with 10nm chromium film.
- c) *Microline electrode*: microline electrode was simply a metal-substrate grating with 125lines/mm. Fig. 6.2c shows a photo of a segment of this electrode taken in transmission mode of the microscope spectrophotometer.
- d) *Nanoline electrode*: nanoline electrode was simply a metal-substrate grating with 1250lines/mm.

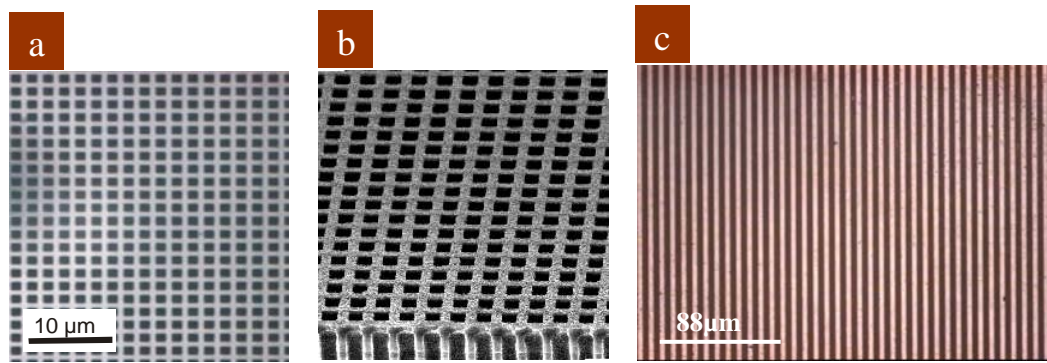


Figure 6.2: a) Photo of a segment of the macroporous silicon used as anode for structuring, and b) SEM picture of the electrode. c) A segment of the metal-substrate grating with 125 lines/mm (the so-called microline electrode) which also was used as anode for line structuring.

6.3 Results and Discussion

Lattice structuring

First series of experiments on structuring was performed using the microporous silicon (Fig. 6.2a and b) as an anode. After treatment and removing the electrodes, it was found that the exact pattern of the electrode was mirrored on the sample. Fig. 6.3a and b show a segment of a sample after treatment. The photos were taken in reflection and transmission modes of the microscope spectrophotometer, respectively. Clearly the pattern of the anode was exactly mirrored on the sample in a way that the contact regions have been bleached considerably as a result of dissolution of silver nanoparticles in the glass matrix, while the spots beneath the holes of the macroporous silicon anode remained unchanged.

The structured area on the sample was then examined using scanning near field optical microscope (SNOM) equipped with a laser diode at $635(\pm 15)$ nm. Fig. 6.3c and d represent the results of the SNOM examination. From the topography picture (Fig. 6.3b) it was concluded that the created structures are embedded and that the height difference between the structured and non-structured areas is in the order of ~ 20 nm.

The overall conclusions from visual impression as well as the SNOM observations were then fully confirmed by scanning electron microscope (SEM) examinations. Figure 6.3e represents the top-view SEM picture from a segment of the structured region. The picture was taken using backscattered electron mode of the SEM. The SEM signal presumably stems from the upper ~ 100 nm layer and hence the light areas indicate silver close to the sample surface. Cleaving the sample and analyzing a cross-section of the structured area using SEM revealed the information on the spatial distribution of the silver nanoparticles. Figure 6.3f shows that the structuring processes resulted in silver depletion regions below the contact areas. As it can be seen from the figure, the interface between the silver rich and depleted regions has approximately the shape of a circle segment, with a maximum distance from the surface of ~ 500 nm.

The results obtained here can be understood considering the material presented in previous chapters, namely that the threshold voltage for the EFAD process is inversely proportional to the filling factor of the nanoparticles, and that for the applied voltages below 1kV there are intermediate stages where the particles are already dissolved in the uppermost layer of the sample with highest filling factor.

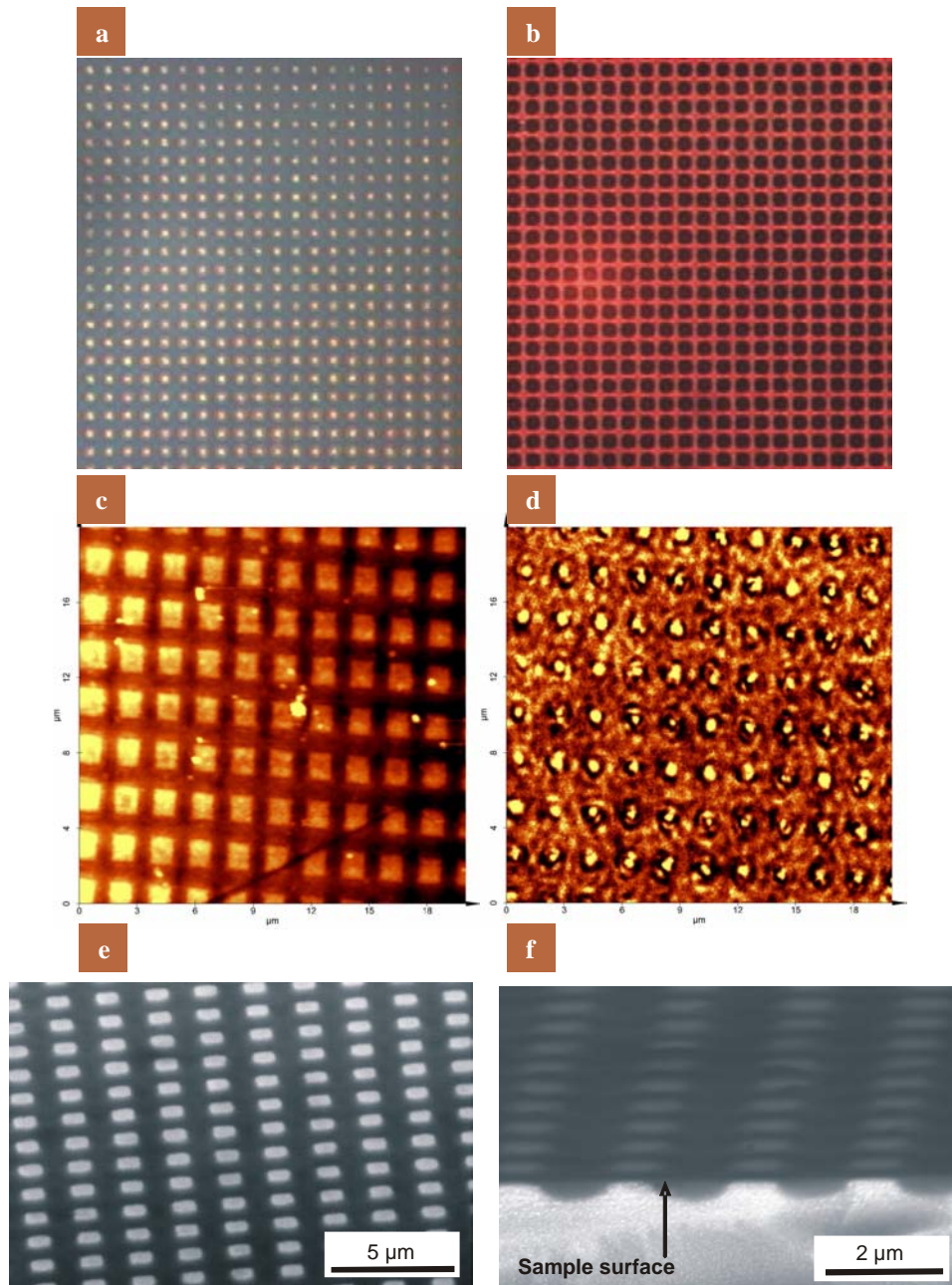


Figure 6.3: Optical, SNOM and SEM images of the metallodielectric structures produced using the macroporous Si electrode with lattice constant of $2\mu\text{m}$. **a and b)** Microscopic images of the structured area taken in reflection and transmission, respectively. **c and d)** SNOM pictures showing topography and intensity profiles of a segment of the structured area on the sample, respectively. The structures appeared as shiny spots in the intensity profile. **e)** SEM picture of the sample after treatment, white indicates silver close to surface. **f)** SEM picture of cross section of the structured area.

According to the situation as such the drift of silver ions away from the surface is stopped due to the formation of a buried, percolated silver layer in a depth of a few hundred nanometres (see chapter 5). As it was found previously in this intermediate situations the distance between the sample surface and the buried layer is defined by the final magnitude of the voltage applied. Creation of the buried layer due to the dissolution process in combination with the presence of a fill factor gradient then results in the standing profile (upward shape) of the structures rather than a downward profile, which one would expect intuitively if total dissolution of silver particles below the walls of the silicon electrode would have occurred.

Optical properties of the composite glass are strongly affected by dissolution process and redistribution of the silver content. Indeed, as it has previously been demonstrated using the Maxwell-Garnett theory, the absorption coefficient as well as the refractive index of the medium strongly depends on the filling factor of the silver nanoparticles (see chapter 3). This fact defines the alteration of the transmission spectra of the original sample presented in Fig. 6.4. As it can be seen, transmittance of the sample subjected to the structuring via EFAD technique raises in the spectral range of 500-700nm. This can be explained by dissolution of the nanoparticles near the surface and hence fading and slight blue shift of the surface plasmon.

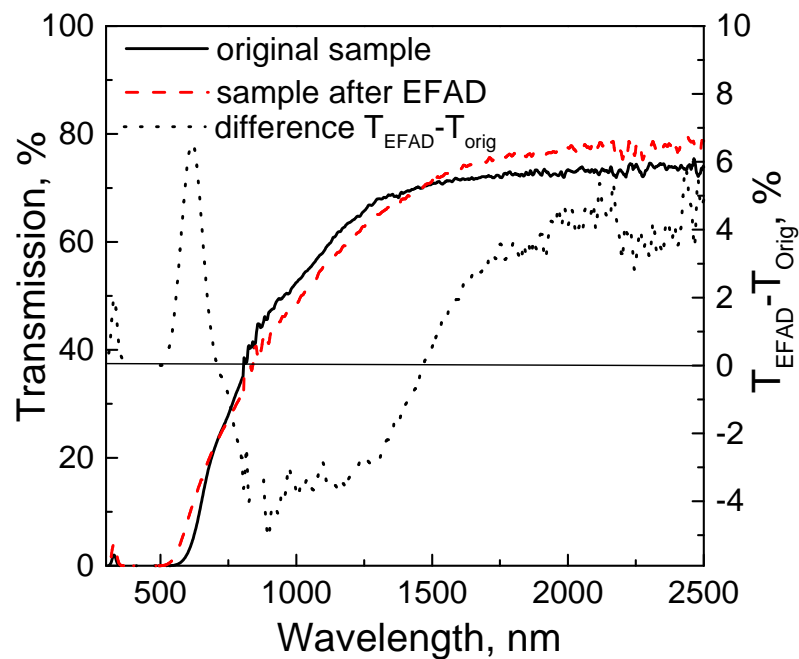


Figure 6.4: Transmission spectra of the original (line) and structured sample (dash line). The spectra are recorder using an UV-visible-NIR spectrometer and a 2mm diameter aperture. For the sake of clarity the differential spectrum is also represented (dots), and shows the change in transmission throughout the experimentally measured region.

Dissolution and hence decrease in filling factor is also responsible for the increase of the transmittance in the 2 micron spectral region. (Decrease in filling factor results in subsequent decrease in refractive index which in turn would result in decrease of the surface reflectivity. This decrease of refractive index could be due to the presence of the residual nanopores, see chapter 5). However, induced losses in the spectral range from 700nm to 1.5 μ m are believed to be due to the diffraction from the generated periodical structure; the pertinent diffraction pattern can be easily observed.

A rough estimation based on the experimentally measured spectra gives a maximum diffraction losses of $\sim 5\%$ of the incident light intensity around $\lambda = 1000$ nm at normal incidence. At wavelengths larger than the structure period ($\lambda \geq 2$ μ m) no diffraction losses were observed, i.e. throughout the transparency range of the glass (up to $\lambda \sim 5$ μ m) the transmission of the structured area is only slightly higher than that of the original sample (measured by FTIR spectroscopy, not shown).

Photonics properties (if any) of the produced metallodielectric structures should be most pronounced for light traveling along the sample surface. This is qualitatively demonstrated by the angular dependences of transmission at $\lambda = 1047$ nm (obtained using a Nd:YLF laser). The results are presented in Fig. 6.5. Whereas the original sample for P-polarization shows a transmission maximum at a Brewster angle of $\sim 65^\circ$ (suggesting refractive index of $n > 2$), no such maximum is observed in the structured region; instead, transmission is decreased by up to 30% around $\theta = 70^\circ$ as compared to the result of the original sample. This effect can apparently be attributed to the in-plane component of light propagation increasing towards larger incidence angles. The detailed study of the photonic features (e.g. band gap) of the presented 2D structures is out of the scope of this work and apparently is the main aspect of future works. In particular the possibility of improvement of the depth profile, a feature which is essential for production of photonic crystals using this technique, will be addressed. Our recent investigations confirm that it is indeed possible to gain control over the depth profile by varying the process parameters.

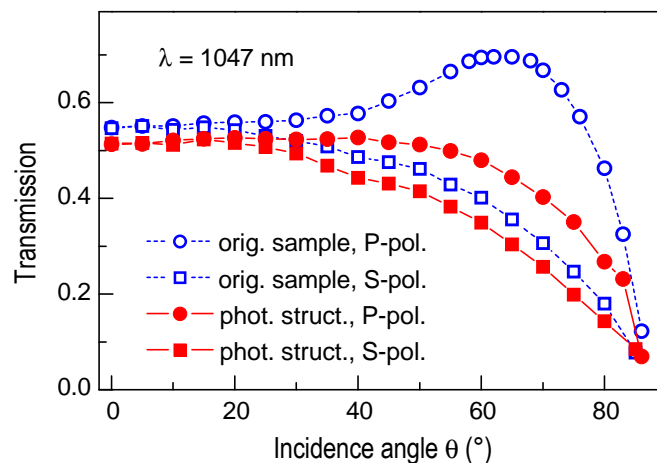


Figure 6.5: Incidence angle dependence of the sample transmission. Transmission for P- and S-polarized light of $\lambda = 1047$ nm of original sample and structured sample area, as a function of incidence angle θ .

Before leaving this part it is worth mentioning the possibility of joining the features presented in the previous chapter that is production of a silver containing buried layer, along with the 2D structuring presented here. Fig. 6.6-(a) presents a SEM picture of cleaved-end of the structured sample. A shiny belt of silver ions, very similar to the one shown in Fig. 5.4-(b), can be clearly seen. Significance of production of the buried layer and the interference pattern as a result of that is then shown in Figures 6.6-(b) and (c), where microscopic pictures of a segment of the border region are recorded in reflection (Fig. 6.6-(b)) and transmission (Fig. 6.6-(c)).

Once again, in reflection mode the border region shows a rainbow-like pattern consisting of a sequence of blue, green and red rings (for comparison see Fig. 5.1). In transmission mode (Fig. 6.6-(c)), however, following the same path from untreated (location O in both Fig. 6.6-(b) and (c)) towards the structured area of the sample, no rainbow pattern is observed, but only a gradual change of color from dark red to faint red. The observation of colors was once again attributed to the reflection of light from the buried layer and its interference with the light reflected from the surface of the sample.

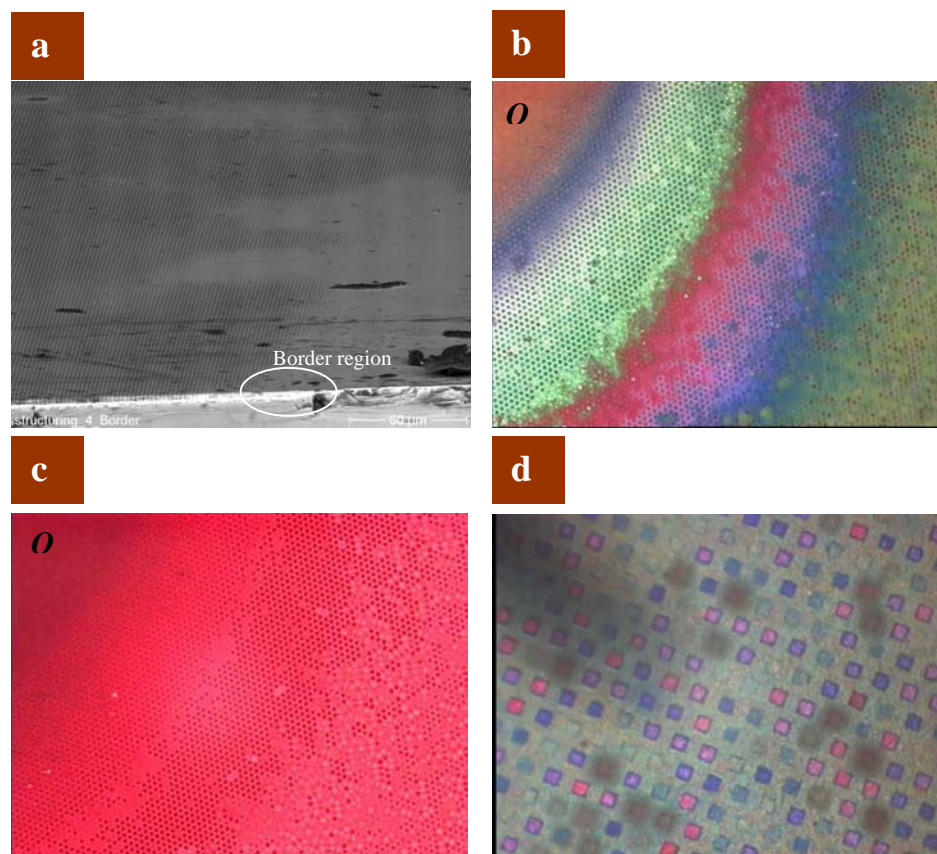


Figure 6.6: **a)** SEM picture of the cross section of the structured sample. **b)** and **c)** Photographs of the segment of the border region of the structured sample. Photographs were taken using a microscope spectrophotometer [MPM 800 D/UV, Zeiss] equipped with CCD camera in: **(b)** reflection and **(c)** transmission modes. **d)** Production of structures representing different colors. The photo is taken in reflection mode of the microscope. For structuring experiments presented here macroporous silicon with lattice constant of $3\mu\text{m}$ is used.

A peculiar feature offered here is the possibility for production of structures which each can exhibit different colours in reflection. An example of this is presented in Fig. 6.6-(d). It is believed that the intentionally provided inhomogenous contact between the electrode and sample is responsible for this observation. This irregular contact between the electrode and sample led to the production of structures at different depth from the surface of the sample. It is believed that interference is responsible for the observed coloration.

Down scaling

Second structuring attempts involved usage of another template consisting of hexagonally arranged pores in silicon with a lattice constant of 500 nm (nonporous silicon). All other experimental conditions were identical to the experiment described above. Figures 6.4-(a) and (b) show SEM pictures (top view) of two regions of the structured areas of the sample after treatment. Apparently even these submicron structures of typically ~ 300 nm in size are reproduced quite well on the silver-glass nanocomposite. Due to the small size of the structures, however, the individual distribution of nanoparticles within the non-dissolved spots becomes important, obviously limiting the regularity of the pattern.

The granular shape of the edges within the produced structures should also have consequences for their optical properties; however these studies have not been performed here. Another important question to be answered is if for submicron structures, as demonstrated here, effective medium theories are still applicable, or if the spots consisting of only a few nanoparticles reveal very special optical properties which have to be discussed in terms of Mie theory including interaction of the individual particles. This is also an upper limit for the down scaling ability of the presented technique, in the sense that the resolution of the structuring process is limited by the size and density of the individual particles.

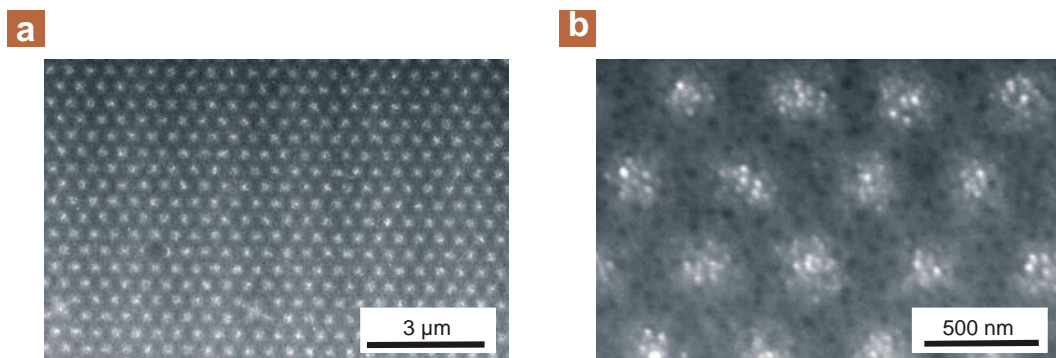


Figure 6.6: a and b) SEM pictures showing top view of the submicron structures produced by the EFAD technique using nanoporous Si as electrode (lattice constant ~ 500 nm).

Line structuring

For the sake of complicity, here the results of production of large areas (20mm \times 20mm) of 2D embedded lines made of densely-packed silver nanoparticles with $\sim 4\mu\text{m}$ as well as 400nm in width and each up to $\sim 5\text{mm}$ in length are presented.

The experimental conditions as well as the physics of the process are identical to the previous discussed material and thus I concentrate on the results only. The only difference is that here microline and nanoline electrodes are employed as anode.

The preliminary experiment was performed on a polydisperse-type II sample using microline electrode with 125lines/mm as anode (Fig. 6.2b). Fig 6.7 shows the results after treatment. As it can be seen the whole area beneath the anode is transparent, with the exception of the metallic lines where there was no contact between the sample and anode, and thus the silver particles has not been destroyed during the EFAD process. Fig. 6.8 shows a segment of the sample after treatment taken in the transmission mode of the microscope spectrophotometer. Once again the structured area was also perfectly working as a diffractive optical element both in transmission and reflection (not shown).

The sample was then subjected to SEM examination (Fig. 6.9). The SEM picture revealed that the region beneath the gaps remained unchanged, whereas the regions in contact with the metallic lines on the anode became optically transparent, obviously as a result of the dissolution process. The width of each structured line was measured to be $\sim 4\mu\text{m}$. Fig. 6.9 also contains an enlarged area of one of the lines. As it can be clearly seen each line is consist of a densely-packed orderly-orientated ellipsoidal silver nanoparticles. Thus, indeed the dichroitic properties of the sample preserved (see chapter 3).

More information on the produced structures was then gained by analyse of cross section of the structured area using SEM. The results are shown in Fig. 6.10 and 6.11. The arrows in both pictures are showing the surface of the sample, where the anode was placed. As it can be seen the structured lines are in fact embedded and once again a shiny belt of silver ions can be clearly seen where the dissolution of silver nanoparticles took place. The depletion depth was estimated from SEM to be $\sim 600\text{nm}$. The over all destruction, dissolution and structuring mechanism is believed to be the same as explained earlier.

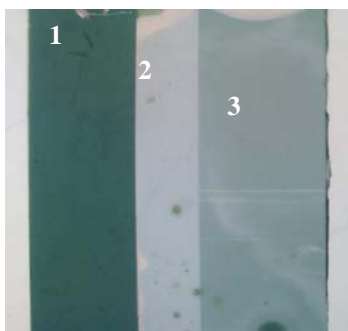


Figure 6.7: Photograph of the sample after structuring. Numbers show: 1) original (untreated), 2) transparent and 3) structured regions of the sample.

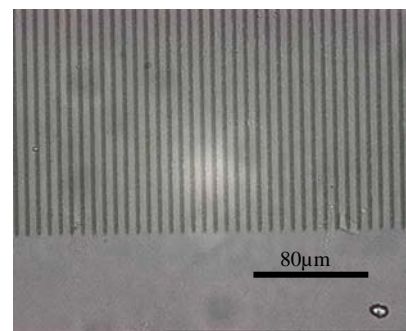


Figure 6.8: Segment of the sample after treatment. The result was a area with embedded structures with 125 metallic lines/mm. Here area with the light grey colour show the transparent region after the treatment whiles the structured metallic lines are shown in dark grey.

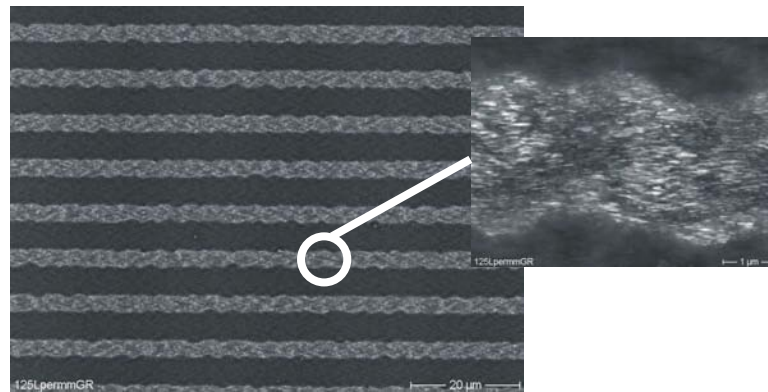


Figure 6.9: SEM picture of a segment of the structured area. The inset shows an enlarged part of one of the structured lines.

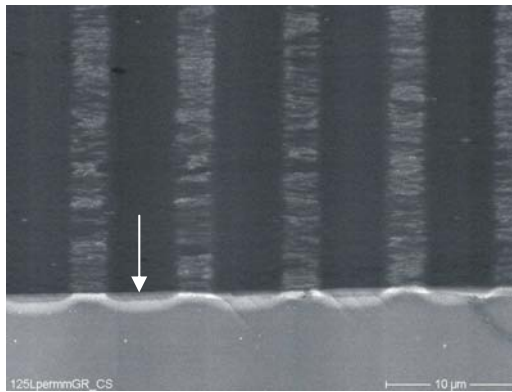


Figure 6.10: SEM picture of the cross section of the structured area. The arrow shows the surface of the sample where the anode was placed.

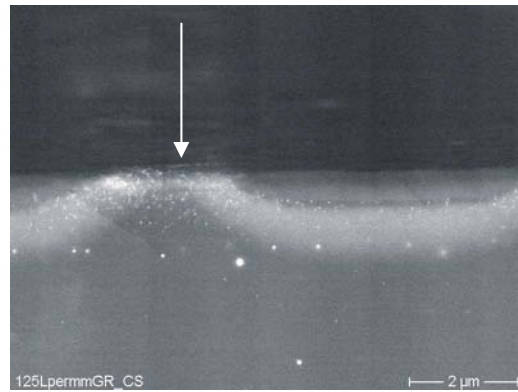


Figure 6.11: SEM picture of the same area as shown in Fig. 6.10 with one of the lines enlarged. The arrow once again shows the surface of the sample.

Scalability of the technique was examined using a polydisperse type I –original sample and the nanoline electrode (1250lines/mm) as anode. All other experimental parameters including the applied voltage and time of the treatment were identical to the previous experiments. Fig. 6.12 shows the result of structuring. As it can be seen embedded lines of densely-packed spherical silver nanoparticles were easily produced. The width of each structured line was estimated to be ~400nm.

One final remark is that the sizes of the structured areas were only limited by the size of the structured electrodes used, here 15mm×15mm.

Figure 6.12: SEM image of the type I-original sample structured employing the nanoline electrode. The width of each structured line was estimated from SEM to be ~400nm. The length of each line was a few mm. The overall structured area was only restricted by the size of the anode.



6.4 Summary

In this chapter, a novel, easy-to-implement, and powerful technique for engineering optical properties of metal-doped nanocomposite glass via gaining control over spatial distribution of the metallic inclusions is described. In particular, 2-D structuring, down to submicron size in glass containing silver nanoparticles, was demonstrated. The presented technique is based on the phenomenon of D.C. electric field-assisted dissolution (EFAD) of metallic nanoparticles in glass matrix. This technique is potentially useful for production of diffractive optical elements, channel waveguides, submicron optical structures suitable for plasmonic applications as well as metallodielectric photonic crystals working in the visible wavelength range, all in metal-doped nanocomposite glasses.

Chapter 7: Conclusions and Future Directions

This chapter not only summarises the work described in the preceding experimental chapters, but also tries to give an indication of the direction some future work might take. The investigations have involved the study of the physical mechanism behind the DC electric field-assisted dissolution (EFAD) of silver nanoparticles in glass matrix as well as dedicated to the applications of the EFAD technique.

This chapter is split into two main sections, dealing with each of the chapters on the experimental work in turn and then discussing the possible future directions. All that remains to be given afterwards apart from the author's curriculum vitae (CV) and list of publications and contributions for both conferences and journals, is a brief introduction to thermal poling of glass, a technique which is very similar to the one used here for achieving the EFAD of silver nanoparticles and a final remark on the evolution of the EFAD.

Summary of the research

The research presented here is the result of an investigation into a new approach for modification and manipulation of optical as well as structural properties of silver-doped nanocomposite glass. The strategy described here was based on seeking a technologically simple and economically attractive approach for gaining comprehensive control over spatial distribution of the silver nanoparticles within the glass matrix. This was achieved by applying a combination of an intense direct current (DC) electric field and moderately elevated temperatures to the material. This resulted in destruction and dissolution of the silver nanoparticles in the glass matrix in the form of silver ions. Thus, results of an attempt to explain the dissolution phenomenon and investigate its potential applications was constructed the thesis.

At first the research was dedicated to the spatial features and dynamics of the dissolution process. For this purpose glass samples with embedded spherical and elongated silver nanoparticles with either exponential (type I) or step (type II) gradient of volume filling factor of the metallic inclusions were used. Application of strong DC electric field (~1kV) and temperature (~280°C) to the type I (type II) sample resulted in partial (total) bleaching of the optical absorption band that is associated with the surface plasmon resonance of silver nanoparticles in glass host. From a macroscopic point of view the phenomena was denominated as "electric field assisted dissolution" (EFAD) and physically interpreted in terms of the ionisation of the silver nanoclusters followed by the removal of silver ions from the clusters and their drift in the depth of the glass matrix, under the combined action of the applied DC electric field and temperature.

Afterwards the possibility to structure a buried layer of percolated silver clusters in the type I samples was explored. The results allowed us to claim the ability to engineer optical properties of the material via gaining control over spatial distribution of silver in the glass. The astonishing visual effects of the phenomena were investigated, modelled in detail and discussed.

Fine optical structuring in nanocomposite materials using the EFAD technique was then subject of the further investigation. Using this technique micron and submicron size structures in the type I as well as type II samples were easily produced. The physics of the process as well as outlooks of this application of the EFAD technique were discussed.

Future Directions

Beyond the already interesting capability of the EFAD technique to make the glass containing embedded silver nanoparticles locally, under micrometric areas with sharp edges, totally and/or partially transparent, there are several other very promising applications of the work presented in this thesis.

Although a lot of research should yet be conducted towards better understanding of the underlying physical mechanism of the EFAD phenomenon, here mostly the potential applications of this effect are considered as to possible future works.

a) DC electric field-assisted production of channel waveguides in silver-doped nanocomposite glass

This becomes fairly evident by simply taking another look at the predictions of Maxwell-Garnett theory presented in chapter 3, where it was shown that by controlling the filling factor of the metallic inclusions in metal-doped nanocomposite glass it should be possible to engineer a metal containing layer with desired optical properties. This, in fact, is what offered by the EFAD technique, namely gaining control over spatial distribution of the metallic inclusions.

Therefore, change in refractive index as a result of increase and/or decrease in filling factor of the metallic inclusions can serve to easily produce various waveguide structures, channel waveguides, in the compound materials.

b) DC electric field-assisted 3D structuring in silver-doped nanocomposite glass

From the thermal-poling of glass it is well-known that sodium ions can be redistributed within the glass matrix under the combined action of a D.C. electric field and elevated temperatures. Also silver ions can also be redistributed within ion-exchange glass by the application of an electric field. If such modification be done before particle formation, in principle, arbitrary 3D optical structures can be produced by using the EFAD technique.

c) DC electric field-assisted ion implantation in glass

Ion implantation is another promising aspect of application of the EFAD technique. Preliminary experiments conducted in our group show that it is possible to implement silver ions in soda-lime glass substrate using this technique. This was done by simply covering one side of the soda-lime glass substrate by Ag past, equipping the glass with two pressed contact electrodes so that anode facing the side with Ag past, and placing the sample in an oven. Application of 1kV at elevated temperatures was enough to implement large amount of silver ions to the glass

substrate. This was confirmed after the experiment by annealing the glass in an air atmosphere inside an oven. The annealing resulted in aggregation of the implanted silver ions and creation of the silver nanoparticles in the near surface region ($\sim 1\mu\text{m}$) of the sample, as appearance of surface plasmon band around 430nm in the extinction spectrum of the sample testified later (Fig. 7.1-red spectrum). The size of the produced nanoparticles was estimated from the width of the SP band to be $\sim 5\text{-}10\text{nm}$ (see chapter 2, Fig. 2.4). Annealing of the same sample longer times resulted in production of larger silver nanoparticles. The estimated value for their size is $40\text{-}50\text{nm}$. In this case the peak of the SP band was approximately around 420nm (Fig. 7.1-black spectrum).

This could be an alternative way to prepare metal-doped nanocomposite glasses as to the classical ion-exchange technique [7.1] and ion beam [7.5]. However, this obviously requires further throughout study of the process.

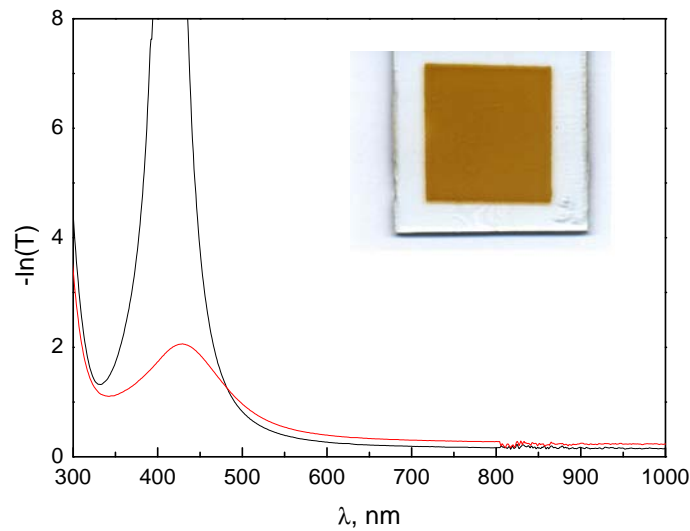


Figure 7.1: Extinction spectra of the samples prepared via DC electric field assisted ion implantation in the glass. The red spectrum belongs to the sample after short time annealing while the black spectrum represents the spectrum of the same sample after longer annealing times. Inset is a photo of the sample exhibiting the red extinction spectrum.

d) DC electric field-assisted submicron optical structuring in glass for surface plasmon subwavelength optics

Perhaps one of the most attractive aspects of surface plasmons (SPs) is the way they help to concentrate and channel light using subwavelength structures. This could lead to miniaturisation of photonics circuits to much smaller length scales than currently achieved [7.2, 7.3].

In principle, a properly structured circuit would first convert light into SPs, which in turn would propagate and be processed by logic elements, before being converted back into light. However, an attractive feature for any such circuit is that, when embedded in dielectric material, the circuit used for propagation of SPs can also be used to carry electrical signals. A newly born branch of photonics, called plasmonics, is dealing with feasibility study of using SPs for various applications in this field.

In the last experimental chapter it was shown that the EFAD technique allows to produce submicron embedded metallic lines in silver-doped nanocomposite glass. SEM analysis of the structures revealed that they consist of densely-packed nanoparticles. This makes the study of their plasmonic properties feasible. Research on this aspect of the work is currently under way in collaboration with our colleagues from the Queen's University of Belfast, U.K.

e) DC electric field-assisted production of metallo-dielectric photonic crystals

I would like to finish this chapter and in fact the thesis by giving some outlooks on using the EFAD technique for production of metallo-glass photonic crystal. Photonic crystal is a periodic structure of more than two dielectrics whose size is in the order of wavelength. They function as a photon equivalent of semiconductors. In other words, they can control the existence of photons with certain wavelength and polarisation by their so-called "photonic bandgap" or in brief PBG. PBGs in turn are ranges of frequencies in which photons can not enter photonic crystals as long as certain conditions are met. A great deal of information can nowadays be found in the literature, and in particular in Ref. [7.4], on the operational mechanism and physics of photonic crystals.

However, metals can also be used as the ingredient for photonics crystals. These sort of photonic crystals are commonly known as metallo-dielectric photonic crystals (MDPC). Metallic photonic crystals have not been investigated as much as their semiconductor counterparts, due to their high absorption which is quite critical for these devices. However, they offer a number of advantages over other dielectric-based photonic crystals such as: a) Metal components can be used for writing of future optoelectronics integrated circuits, b) PBG of MDPC can be more robust to disorders of their structures, c) High temperature operation with MDPC may be possible, d) Metals exhibit stronger nonlinearity than other optical material, e) SPs in metal components can be existed and finally but most importantly metals are more reflective than for instance semiconductors over a wide range of wavelength. Thus, MDPC will tend to exhibit pronounced PBGs with fewer layers than semiconductor-based photonic crystals. Thus the advantages of metals can be used to produce photonic crystals with unique properties.

Indeed, MDPCs have been already proposed as possible candidates for creation of PBGs in the optical spectral range [7.5-7.8]. In this context silver-doped nanocomposite materials can be used as a based material for production of MDPCs. The EFAD technique, in this case in combination with laser-assisted techniques, can be used for structuring in these materials, and hence production of silver-dielectric photonic crystal would be possible.

References

Chapter 1

- 1.1 U. Kreibig, M. Vollmer, *Optical Properties of Metal Clusters* (Springer, Berlin, 1995).
- 1.2 V. M. Shalaev, *Optical Properties of Nanostructured Random Media* (Springer, Berlin, 2002).
- 1.3 K. L. Kelly, E. Coronado, L.L. Zhao, G.C. Schatz, *J. Phys. Chem. B* **107**, 668 (2003).
- 1.4 R. Jin, Y. C. Cao, E. Hao, G. S. Merraux, G. C. Schatz, C. A. Mirkin, *Nature* **425**, 487 (2003).
- 1.5 M. S. Gudiksen, L. J. Lauhon, J. Wang, D. C. Smith, C. M. Lieber, *Nature* **415**, 617 (2002).
- 1.6 P. Chakaraborty, *J. Mat. Sci.* **33**, 2235 (1998).
- 1.7 F. Gonella, P. Mazzoldi, *Handbook of Nanostructured Materials and Nanotechnology*, Vol. 4., p. 81ff. (Academic Press, San Diego, 2000).
- 1.8 G. Seifert, M. Kaempfe, K.-J. Berg, H. Graener, *Appl. Phys. B.* **73**, 355 (2001).
- 1.9 J. R. Krenn, *Nature Mater.* **2**, 210 (2003).
- 1.10 S. A. Maier, P. R. G. Kik, H. A. Atwater, S. Meltzer, E. Harel, B. Koel, A. G. Requicha, *Nature Mater.* **2**, 229 (2003).
- 1.11 K.-J. Berg, A. Berger, H. Hofmeister, *Z. Phys. D* **20**, 309 (1991).
- 1.12 A. Miotelo, G. DeMarchi, G. Mattei, P. Mazzoldi, A. Quaranta, *Appl. Phys. A* **70**, 415 (2000).
- 1.13 R. Borek, K.-J. Berg, G. Berg, *Glastech. Ber. Glass Sci. Technol.* **71**, 352 (1998).
- 1.14 M. Kaempfe, T. Rainer, K.-J. Berg, G. Seifert, H. Graener, *Appl. Phys. Lett.* **74**, 1200 (1999).
- 1.15 G. Seifert, M. Kaempfe, K.-J. Berg, H. Graener, *Appl. Phys. B* **71**, 795 (2000).
- 1.16 M. Kaempfe, G. Seifert, K.-J. Berg, H. Hofmeister, H. Graener, *Eur. Phys. J. D* **16**, 237 (2001).
- 1.17 A. Podlipensky, A. Abdolvand, G. Seifert and H. Graener, *Appl. Phys. A* **80**, 1647 (2005).
- 1.18 T. Wenzel, J. Bosbach, A. Goldmann, F. Stietz, F. Träger, *Appl. Phys. B* **69**, 513 (1999).
- 1.19 F. Stietz, *Appl. Phys. A* **72**, 381 (2001).

- 1.20 H. Hofmeister, W. G. Drost, A. Berger, *NanoStruct. Mater.* **12**, 207 (1999).
- 1.21 See for example the following link: <http://www.codixx.de/>
- 1.22 M. A. McCord, M. J. Rooks, *Handbook of Microlithography, Micromachining and Microfabrication*, (ed. By P. Rai-Choudhury), 139-249. SPIE and The Institution of Electrical Engineering, Bellingham, WA.

Chapter 2

- 2.1 R. D. Guenther, *Modern Optics* (JOHN WILEY & SONS, 1990), Chapter 2.
- 2.2 H. Inouye, K. Tanaka, I. Tanahashi, K. Hirao, *J. Phys. Soc. Jpn.* **68**, 3810 (1999).
- 2.3 R. H. Ritchie, *Phys. Rev.* **106**, 874 (1957).
- 2.4 K.-J. Berg, A. Berger, H. Hofmeister, *Z. Phys. D* **20**, 309 (1991).
- 2.5 A. Miotelo, G. DeMarchi, G. Mattei, P. Mazzoldi, A. Quaranta, *Appl. Phys. A* **70**, 415 (2000).
- 2.6 W. H. Armisted, S. D. Stookey, *Science* **144**, 150 (1964).
- 2.7 H. Hofmeister, S. Thiel, M. Dubiel, E. Schurig, *Appl. Phys. Lett.* **70**, 1694 (1997).
- 2.8 J. Qui, M. Shirai, T. Nakaia, J. Si, X. Jiang, C. Zhu, K. Hirao, *Appl. Phys. Lett.* **81**, 3040 (2002).
- 2.9 K. Kaneko, H. Sun, X. Duan, S. Kawata, *Appl. Phys. Lett.* **83**, 1426 (2003).
- 2.10 M. Kaempfe, T. Rainer, K.-J. Berg, G. Seifert, H. Graener, *Appl. Phys. Lett.* **74**, 1200 (1999).
- 2.11 G. Seifert, M. Kaempfe, K.-J. Berg, H. Graener, *Appl. Phys. B* **71**, 795 (2000).
- 2.12 G. Seifert, M. Kaempfe, K.-J. Berg, H. Graener, *Appl. Phys. B.* **73**, 355 (2001).
- 2.13 M. Kaempfe, G. Seifert, K.-J. Berg, H. Hofmeister, H. Graener, *Eur. Phys. J. D* **16**, 237 (2001).
- 2.14 A.Kiesow, S. Strohkark, K. Leschner, A.Heilmann, A. Podlipensky, A. Abdolvand, G. Seifert, H.Graener, *Conference on nanometer scale science and technology (NANO-8), NS3-WeA7, Venice/Italy, 2004 (Invited)*.
- 2.15 A. Podlipensky, A. Abdolvand, G. Seifert and H. Graener, *Appl. Phys. A* **80**, 1647 (2005).
- 2.16 U. Kreibig, ,M. Vollmer, *Optical Properties of Metal Clusters* (Springer, Berlin, 1995).
- 2.17 V.M. Shalaev, *Optical Properties of Nanostructured Random Media* (Springer, Berlin, 2002).

References

- 2.18 J. C. Quail, H. J. Simon, *J. Appl. Phys.* **56**, 2589 (1984).
- 2.19 T. Y. F. Tsang, *Opt. Lett.* **21**, 245 (1996).
- 2.20 A. Podlipensky, J. Lange, G. Seifert, H. Graener, I. Cravetchi, *Opt. Lett.* **28**, 716 (2003).
- 2.21 A. Podlipensky, A. Abdolvand, J. Lange, G. Seifert, H. Graener, *10th International Microoptics Conference (MOC'04), L-36, September 1-3, Jena/Germany (2004)*.
- 2.22 S. M. Nie, S. R. Emery, *Science* **275**, 1102 (1997).
- 2.23 K. Kneipp, *Phys. Rev. Lett.* **78**, 1667 (1997).
- 2.24 J. Homola, S. S. Yee, G. Gauglitz, *Sensors Actuat. B* **54**, 3 (1999).
- 2.25 G. Mie, *Ann. Phys.* **25**, 377 (1908).
- 2.26 C. F. Bohren, D. R. Huffman, *Absorption and Scattering of light by Small Particles (Wiley Science Paperwork Series, New York 1998)*.
- 2.27 J. P. Marton, J. R. Lemon, *Phy. Rev. B* **4**, 271 (1971).
- 2.28 G. Xu, M. Tazawa, P. Jin, S. Nakao, *Appl. Phys. A* **78**, 1011 (2004).
- 2.29 V. A. Markel, L. S. Muratov, M. I. Stockman, T. F. George, *Phys. Rev. B* **43**, 8183 (1991).
- 2.30 V. A. Markel, V. Shalaev, E. B. Stechel, W. Kim, R. L. Armstrong, *Phys. Rev. B* **53**, 2425 (1998).
- 2.31 S. V. Karpov, A. L. Basko, A. K. Popov, V. V. Slabko, T. F. George, *Recent Research Developments in Optics 2*, pp. 427-463 (Research Signpost, Trivandrum, India, 2002).
- 2.32 B. Lamprecht, A. Leitner, F. G. Ausseneg, *Appl. Phys. B* **64**, 269 (1997).
- 2.33 N. Bloembergen, J. Nonlin. *Opt. Phys. Mater.* **6**, 377 (1997).
- 2.34 B. N. Chirkov, C. Momma, S. Nolte, F. Von Alvensleben, A. Tunnermann, *Appl. Phys. A* **63**, 109 (1996).
- 2.35 P. Pronko, S. Dutta, J. Squier, J. Rudd, G. Mourou, *Opt. Commun.* **114**, 106 (1995).
- 2.36 H. Misawa, Hong-Bo Sun, S. Juodkazis, M. Watanabe, S. Matsuo, *Proc. SPIE* **3933**, 246 (2000).
- 2.37 K. M. Davis, K. Miura, Naoki Sugimoto, Kazuyuki Hirao, *Opt. Lett.* **21**, 1729 (1996).
- 2.38 E. N. Glezer, E. Mazur, *Appl. Phys. Lett.* **71**, 882 (1997).
- 2.39 K. Miura, Jianrong Qiu, H. Inouye, T. Mitsuyu, K. Hirao, *Appl. Phys. Lett.* **71**, 3329 (1997).

References

- 2.40 D. Homoelle, S. Wielandy, Alexander L. Gaeta, N. F. Borrelli, Charlene Smith, *Opt. Lett.* **24**, 1311 (1999).
- 2.41 Jianrong Qiu, Congshan Zhu, Takayuki Nakaya, Jinhai Si , Kazuo Kojima, Fumito Ogura, Kazuyuki Hirao, *Appl. Phys. Lett.* **79**, 3567 (2001).
- 2.42 Kaoru Minoshima, Andrew M. Kowalevich, Ingmar Hartl, Erich P. Ippen, James G. Fujimoto, *Opt. Lett.* **26**, 1516 (2001).
- 2.43 Hong-Bo Sun, Ying Xu, Saulius Juodkazis, Kai Sun, Mitsuru Watanabe, Shigeki Matsuo, Hiroaki Misawa, Junji Nishii, *Opt. Lett.* **26**, 325 (2001).
- 2.44 K. Miura, Jianrong Qiu, S. Fujiwara, S. Sakaguchi, K. Hirao, *Appl. Phys. Lett.* **80**, 2263 (2002).
- 2.45 P. Grua, J. P. Morreeuw, H. Bercegol, G. Jonusauskas, F. Vallée, *Phys. Rev. B* **68**, 035424 (2003).
- 2.46 M. Kaempfe, *Doctoral Dissertation (PhD Thesis), Martin-Luther-University Halle-Wittenberg (2000)*.
- 2.47 A. Podlipensky, *Doctoral Dissertation (PhD Thesis), Martin-Luther-University Halle-Wittenberg (2005)*.
- 2.48 K.Y. Lo, J.T. Lue, *Phys. Rev. B* **51**, 2467 (1995).
- 2.49 K. Uchida, *et al.*, *JOSA B* **11**, 1267 (1994).
- 2.50 F. Korte, *et. al.*, *Appl. Phys. A* **77**, 229 (2003).
- 2.51 A. Durrant, *Quantum Physics of Matter (Institute of Physics, 2000), Chapter 2*.
- 2.52 J. D. Jackson, *Classical Electrodynamics (John Wiley and Sons, 1975)*.
- 2.53 A. Hilger, M. Tenfelde, U. Kreibig, *Appl. Phys. B* **73**, 361 (2001).
- 2.54 See for example the following link: <http://www.codixx.de/>
- 2.55 H. A. Lorentz, *The theory of electrons (Dover, New York, 1952)*.
- 2.56 P. K. L. Drude, *Theory of Optics (Dover, New York, 1959)*.
- 2.57 M. Bass, *Encyclopaedia of Physical Science and Technology 8 (Academic Press, New York, 1992)*.
- 2.58 F. Wooten, *Optical properties of solids (Academic Press, New York, 1972)*.
- 2.59 V. V. Kresin, *Physical Review B* **51**, 1844 (1995).
- 2.60 B. Lamprecht, A. Leitner, F. R. Aussenegg, *Appl. Phys. B* **64**, 269 (1997).

Chapter 3

- 3.1 K. J.- Berg, A. Berger, H. Hofmeister, *Z. Phys. D* **20**, 309 (1991).
- 3.2 H. Hofmeister, W. G. Drost, A. Berger, *Nanostruct. Mater.* **12**, 207 (1999).
- 3.3 R. Borek, K. –J. Berg, G. Berg, *Glass Sci. Technol.* **71**, 352 (1998).
- 3.4 See the following link: <http://www.codixx.de/>
- 3.5 U. Kreibig, M. Vollmer, *Optical Properties of Metal Clusters* (Springer, Berlin, 1995).
- 3.6 G. Mie, *Ann. Phys.* **25**, 377 (1908).
- 3.7 C. F. Bohren, D. R. Huffman, *Absorption and Scattering of light by Small Particles* (Wiley Science Paperwork Series, New York 1998).
- 3.8 V.M. Shalaev, *Optical Properties of Nanostructured Random Media* (Springer, Berlin, 2002).
- 3.9 J. P. Marton, J. R. Lemon, *Phy. Rev. B* **4**, 271 (1971).
- 3.10 G. Xu, M. Tazawa, P. Jin, S. Nakao, *Appl. Phys. A* **78**, 1011 (2004).
- 3.11 V. A. Markel, L. S. Muratov, M. I. Stockman, T. F. George, *Phys. Rev. B* **43**, 8183 (1991).
- 3.12 V. A. Markel, V. Shalaev, E. B. Stechel, W. Kim, R. L. Armstrong, *Phys. Rev. B* **53**, 2425 (1998).
- 3.13 S. V. Karpov, A. L. Basko, A. K. Popov, V. V. Slabko, T. F. George, *Recent Research Developments in Optics 2*, pp. 427-463 (Research Signpost, Trivandrum, India, 2002).
- 3.14 B. Lamprecht, A. Leitner, F. G. Ausseneg, *Appl. Phys. B* **64**, 269 (1997).
- 3.15 A. Podlipensky, A. Abdolvand, G. Seifert and H. Graener, *Appl. Phys. A* **80**, 1647 (2005).
- 3.16 S. Berthier, *Optique des milieux composites*, Polytechnica, Paris, 1993.
- 3.17 J. C. M. Garnett, *Philos. Trans. R. Soc. London* **205**, 237 (1906).
- 3.18 D. A. G. Bruggeman, *Ann. Phys.* **24**, 636 (1935).
- 3.19 J. I. Gittleman and B. Abeles, *Phys. Rev. B* **15**, 3273 (1977).

Chapter 4

- 4.1 K. –J. Berg, A. Berger, H. Hofmeister, *Z. Phys. D* **20**, 309 (1991).

References

- 4.2 R. Borek, K. -J. Berg, G. Berg, *Glass Sci. Technol.* **71**, 352 (1998).
- 4.3 See the following link: <http://www.codixx.de/>
- 4.4 M. Kaempfe, T. Reiner, K. J.- Berg, G. Seifert, H. Graener, *Appl. Phys. Lett.* **74**, 1200 (1999).
- 4.5 R. A. Myers, N. Mukherjee, S. R. J. Brueck, *Opt. Lett.* **16**, 1732 (1991).
- 4.6 P. G. Kazansky, A. Kamal, P. St. J. Russell, *Opt. Lett.* **18**, 693 (1993).
- 4.7 P.G. Kazansky, P. St. J. Russel, *Opt. Commun.* **110**, 611 (1994).
- 4.8 F. C. Garcia, I. C. S. Carvalho, E. Hering, W. Margulis, B. Lesche, *Appl. Phys.Lett.* **72**, 3252 (1998).
- 4.9 V. M. Shalaev, *Optical Properties of Nanostructured Random Media* (Springer, Berlin, 2002).
- 4.10 A. Heilmann, A. Kisow, M. Gruner, U. Kreibig, *Thin Solid Films* **175**, 343 (1999).
- 4.11 A. W. Snow, H. Wohltjen, *Chem. Mater.* **10**, 947 (1998).
- 4.12 R. C. Doty, H. Yu, C. K. Shih, B. A. Korgel, *J. Phys. Chem. B* **105**, 8291 (2001).
- 4.13 W. P. Wuelfing, R. W. Murray, *J. Phys. Chem. B* **106**, 3139 (2002).
- 4.14 S. Chen, *Anal. Chim. Acta* **29**, 496 (2003).
- 4.15 A. Kisow, J. E. Morris, C. Radehause, A. Heilmann, *J. Appl. Phys.* **94**, 6988 (2003).
- 4.16 S. Kirkpatrick, *Phys. Rev. Lett.* **27**, 1722 (1971).
- 4.17 B. J. Last, D. J. Thouless, *Phys. Rev. Lett.* **27**, 1719 (1971).
- 4.18 A. P. Sutton, R. W. Balluffi, *Interfaces in crystalline materials* (Oxford University Press: New York, 1995).
- 4.19 J. R. Shulman, W. D. Compton, *Color centers in solids*, (Pergamon Press: New York, 1962).
- 4.20 K. L. Kelly, E. Coronado, L. L. Zhao, G. C. Schatz, *J. Phys. Chem. B* **107**, 668 (2003).
- 4.21 L. E. Myers, *SUSSP Proceedings 52, Advances in Lasers and Applications, Edited by D. M. Finlayson, B. D. Sinclair and P. Osborne, 141-180* (1998).
- 4.22 A. Podlipensky, A. Abdolvand, G. Seifert and H. Graener, *Appl. Phys. A* **80**, 1647 (2005).
- 4.23 P. B. Johnson and R. W. Christy, *Physical Review B* **6**, 4370 (1972).

References

- 4.24 P. G. Kazansky, P. St. J. Russel, *Opt. Comm.* **110**, 611 (1994).
- 4.25 T. Yano, T. Nagano, J. Lee, S. Shibata, M. Yamane, *Sol. State Ionics Sol.* **150**, 281 (2002).
- 4.26 U. Kreibig, M. Vollmer, *Optical Properties of Metal Clusters* (Berlin: Springer, 1995).
- 4.27 P. Chakraborty, *J. Mat. Sci.* **33**, 2235 (1998).

Chapter 5

- 5.1 V. M. Shalaev, *Optical Properties of Nanostructured Random Media* (Springer, Berlin, 2002).
- 5.2 C. F. Bohren, D. R. Huffman, *Absorption and Scattering of light by Small Particles* (Wiley Science Paperwork Series, New York 1998).
- 5.3 G. Xu, M. Tazawa, P. Jin, S. Nakao, *Appl. Phys. A* **78**, 1011 (2004).
- 5.4 A. Podlipensky, A. Abdolvand, G. Seifert and H. Graener, *Appl. Phys. A* (published first online 25.11.2004).
- 5.5 S. E. Paje, J. Liopis, M. A. Villegas, J. M. Fernandez Navarro, *Appl. Phys. A* **63**, 431 (1996).
- 5.6 P. B. Johnson, R. W. Christy, *Phys. Rev. B* **6**, 4370 (1972).
- 5.7 S. Bosch, J. Ferré-Borrull, and J. Sancho-Parramon, *Solid State Elec.* **45**, 703 (2001). See also: <http://www.ub.edu/optmat>
- 5.8 P. H. Berning, *Physics of thin films* (Academic Press, New York, 1963), Vol. 1.
- 5.9 H. A. MacLeod, *Thin-film optical filters* (Adam Hilder Ltd. Bristol, 1986).
- 5.10 *SOPRA n & k Optical Database* (available at <http://www.sopra-sa.com/more/database.asp>).
- 5.11 J. P. Borgogno, B. Lazarides, and E. Pelletier, *Appl. Opt.* **21**, 4020 (1982).
- 5.12 W. Theiss, *Advances in Solid State Physics 33*, R. Helbig ed. Vieweg, Braunschweig, 1993.
- 5.13 S.E. Paje, J. Llopis, M. A. Villegas, and J. M. Fernandez Navarro, *Appl. Phys. A.* **63**, 431 (1996).
- 5.14 K. C. Park, *Appl. Opt.* **3**, 877 (1964).

Chapter 6

- 6.1 V. Lehmann, *J. Electrochem. Soc.* **140**, 2838 (1993).

- 6.2 See for example http://www.mpi-halle.mpg.de/~porous_m/
- 6.3 T. Rogers, J. Kowal, *Sensors and Actuators A* **46-47**, 113 (1995).
- 6.4 M. Despont, H. Gross, F. Arrouy, C. Stebler, U. Staufer, *Sensors and Actuators A* **55**, 219 (1996).

Chapter 7

- 7.1 K. -J. Berg, A. Berger, H. Hofmeister, *Z. Phys. D* **20**, 309 (1991).
- 7.2 J. Pendry, *Science* **285**, 1687 (1999).
- 7.3 B. Hecht, H. H. Bielefeldt, L. Novotny, Y. Inouye and D. W. Pohl, *Phys. Rev. Lett.* **77**, 1889 (1996).
- 7.4 J. D. Joannopoulos, R. D. Meade, J. N. Winn, *Photonic Crystals: Molding the Flow of Light*, (Princeton University Press, 1995).
- 7.5 A. Moroz, *Phys. Rev. Lett.* **83**, 5274 (1999).
- 7.6 E. Lidorikis, M. M. Sigalas, E. N. Economou, C. M. Soukoulis, *Phys. Rev. Lett.* **81**, 1405 (1998).
- 7.7 E. Lidorikis, M. M. Sigalas, E. N. Economou, C. M. Soukoulis, *Phys. Rev B* **61**, 13458 (2000).
- 7.8 C. Jin, X. Meng, B. Cheng, Z. Li, D. Zhang, *Phys. Rev. B* **63**, 195107 (2001).

Appendix A: Thermal poling of glass: a brief introduction

Silica glass is an amorphous material and possesses inversion symmetry on a macroscopic scale. Hence the vanishing second order nonlinearity (SON), χ^2 , makes it impossible to use this material for efficient second-order nonlinear processes. Nevertheless, in 1980s many researchers reported on photoinduced second harmonic generation (SHG) from optical fibres by launching of strong Infrared (IR) beams from Nd:YAG lasers [1-5]. These were the very first demonstrations of breaking the symmetry of an amorphous material such as glass.

Coherent photo-galvanic effect was identified as the cause of the photoinduced SHG, through which a spatially modulated static electric field along the fibre is established [6-10]. The electric field couples with third order nonlinearity (TON), χ^3 , of the glass and results in an effective χ^2 . The period of the self-organized electric field in the fibre alternates spatially to provide constructive interference through quasi-phase matching (QPM). The efficiency of the frequency doubling process was high enough to pump a dye laser with the green light produced by photoinduced SHG [3]. Following this demonstration a considerable research has been carried out in order to understand the fundamental physics behind the observed phenomenon and assess the compatibility of the new method with nonlinear crystals. Eventually, the efficiency of the photoinduced SHG was found to be limited by the low value of the nonlinearity, 10^{-3} pm/V, as well as by the length of the self-organized QPM-grating which cannot exceed 60-80 cm. (This was due to chromatic dispersion and phase modulation [4].) Efficiencies up to few percentages have been demonstrated [11-17], but unfortunately this figure did not make the photoinduced SHG attractive for real applications.

An important point in the search for an efficient glass-based second-order nonlinear material was the work of Myers *et. al.* in 1991 [18]. The authors observed that a permanent SON is induced in a fused-silica glass plate once heated to moderately elevated temperatures of 250°C-330°C with an applied voltage of about 3 kV -5 kV for 15 min with subsequent cooling to the ambient temperature with the voltage still applied. (This procedure is called the thermal poling of glass.) It has been suggested that a high electrostatic field E_{dc} , appearing in a thin depletion region near the anodic surface, is in fact responsible for the observed phenomenon, similarly to the explanation of the photoinduced SHG. Despite the vanishing χ^2 in glass, the coupling between the electro-static field E_{dc} and the intrinsic third-order nonlinearity of the glass resulted in observation of effective SON. According to Ref. [19] the SON and TON are related via the following equation:

$$\chi^2 = 3\chi^3 E_{dc} . \quad (\text{A.1})$$

This expression shows that the interaction between the TON and the electrostatic field produces the same effect as a SON on the optical field. For the strong field strength of $E_{dc} \sim 2 \times 10^9$ V/m [21,22], fairly close to the dielectric breakdown of fused silica, and taking into account that for silica the χ^3 is approximately equal to 2×10^{-22} m²/V² [20], the χ^2 in poled glass is expected to be ~ 1 pm/V. This value was indeed measured experimentally and is of the same order of magnitude as the nonlinear susceptibilities of some of the widely used nonlinear crystals for frequency doubling, such as KDP (~ 1 pm/V), BBO (~ 3.8 pm/V), and quartz (~ 0.6 pm/V) [23].

The mechanism that leads to the establishment of the SON in the glass has not yet fully understood. The origin of the electro-static field E_{dc} , responsible for χ^2 , has been subject of debate since 1990s, although poling had been studied before in the context of polymers [24, 25]. The application of high voltages to silica at elevated temperatures has been studied since 1970s, although not in the context of optics [26]. From these studies it was known that alkali ions such as Na⁺ and Li⁺, that are present in silica as impurities, are bonded to negatively charge non-bridging oxygen (NBO) sites, and may drift under the action of electric fields. It was also known, from the work of Myers' and co-workers [18], that the nonlinearity was located in a thin layer, typically in less than 10 μ m, beneath the surface of the glass plate that had been in contact with the anode electrode. As an explanation two mechanisms were proposed: either the nonlinearity was caused by orientation of bonds or by the creation of a space charge field, both leading to a DC electronic polarization [27, 28].

It has been suggested that the high temperature involved in the poling process increases the mobility of the impurities present in the glass, mainly alkali ions such as Na⁺. Therefore, upon the application of an electric field, the positively charged sodium ions drift towards the cathode where they are neutralized by injected electrons. Under the hypothesis of zero ionic conductivity at the anode (blocking electrode), during the migration ions leave a negatively charged depleted region behind themselves. The depleted region is located a few microns beneath the anodic surface. Due to the lack of mobile charges the depleted region has a much larger resistivity than the rest of the glass. Like in a voltage divider, the applied voltage tends to mainly drop across the more resistive depleted region. As a consequence, a large static electric field is established between the depleted layer and the anode. The process is schematically represented in Fig. A-1.

Kazansky *et. al.* distinguished between two possibilities that could arise at this stage [28]. In fact, either orientation of NBO bonds or glass ionization could take place under the action of the high electrostatic field. In the former hypothesis, the high temperature increases the mobility of the NBO dipoles, whereas the applied electric field forces them all to orient in the same direction. After cooling, the dipoles would be frozen in one direction, thus breaking the symmetry of the glass and accounting for the observed SON.

In the latter hypothesis, the static field is responsible for the ionization of the glass in the anodic region, leading to the creation of a positive charge layer that screens the external field and stops the process. When the sample is cooled down the ions are trapped in their positions. A high static electric field, between the positive layer and the negatively charged region, is then frozen in the glass once again breaking the centro-symmetric structure.

There are strong arguments against a significant contribution to the effective SON due to the orientation of dipoles in silica glass [29-33]. The theoretical models suggested for the poling process can be classified into two main groups, namely single carrier and multiple carrier models, namely single carrier model and multiple carrier model.

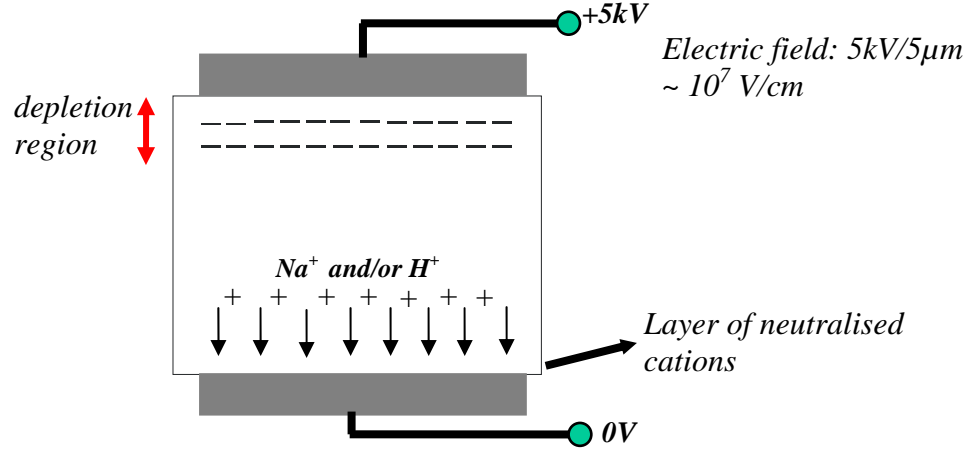


Figure A-1: A schematic representation of the thermal poling process.

As early as in 1953 researchers developed a model for the space charge build-up in alkali halide crystals [34]. The model can be easily adapted to the case of positive charge carriers. According to this model, Na^+ is assumed to be the only mobile charge carrier. The anode is assumed to act as a blocking electrode, and under these circumstances electrical neutrality requires an equal amount of fixed negative charges to be present in the glass, for instance negatively charged NBO. (The NBO sites are assumed to be immobile.)

At steady state the electric field is given by [34]:

$$E_{dc} = \frac{q_e N}{\epsilon} (d_{dep} - x) \quad 0 < x < d_{dep}, \quad (\text{A.2})$$

$$E_{dc} = 0 \quad x > d_{dep}, \quad (\text{A.3})$$

where d_{dep} is the thickness of the depleted region, q_e is the elementary charge, N is the fixed charge density associated with the NBO-hole centres and ϵ is the dielectric permittivity of glass. This simple model in fact is capable of describing all the essential features of thermal poling. During the migration of Na^+ , the charge front which separates the depletion region and the neutral region moves in the glass according to:

$$d(t) = d_{dep} \tanh\left(\frac{t}{2\tau}\right), \quad (\text{A.4})$$

where d_{dep} and τ in A.4 are given as following:

$$d_{dep} = \sqrt{\left(\frac{2\varepsilon V}{q_e N}\right)}; \quad \tau = \frac{d_{dep}}{2\mu E_0},$$

where μ is the effective mobility of sodium. The motion of the charge front can be measured by the current that flows through the glass, taking into account that d_{dep} is much smaller than the thickness of the glass; the current can be well approximated by [34]:

$$I(t) \approx \frac{I(0)}{\cosh^2(t/2\tau)}, \quad (\text{A.5})$$

Where the current at $t=0$ is given by: $I(0) = [Aq_e N d_{dep} / 2\tau]$, where A is the cross section of the electrode.

Using the following known values for fused silica of [35]: $\varepsilon = 3.8\varepsilon_0$; $N=2 \times 10^{22} \text{m}^{-3}$; $\mu_{Na^+} = 1 \times 10^{-15} \text{m}^2 \text{V}^{-1} \text{s}^{-1}$, the thickness of the depletion region can be calculated to be $\sim 9 \mu\text{m}$. The depletion region for a 1mm thick silica glass is formed on the time scale of ~ 20 min poled at 4 kV. This is ten times faster for a ten times thinner sample. The frozen electric field peaks at the surface in contact with the anode and its maximum value according to eq. A.2, is $\sim 10^9$ V/m which is very close to the value of the electrical breakdown in silica. It suggests that high field ionization stops the poling process, as envisaged in [29]. As a consequence the SON is also limited in silica to values of ~ 1 pm/V. The applied field mainly alters the time scale of the process and E_{dc} depends on the charge carrier concentration. From this simple model it is possible to infer that a glass sample having lower charge concentration will exhibit lower nonlinearity and a wider depletion region. These results were confirmed by the findings of researchers reported in [36-39].

Although the single carrier model describes the general features of the poling process reasonably well, it did not account for some of the experimental evidence. For instance two time scales was found by researchers during poling and de-poling current measurements [35]. This behaviour was attributed to the presence of a second charge carrier with much lower, \sim an orders of magnitude lower, mobility. In-diffusion of H^+ from the atmosphere, driven by the high electrostatic field, was thought to be taken place during the poling. Indeed the presence of a positive charge layer between the negatively charged depleted region and the anodic surface was revealed using a technique called “laser-induced pulse pressure (LIPP)” [31]. In [40] researchers pointed out the relevance of the poling atmosphere by performing poling in air or under vacuum (10^{-8} atm.). Samples poled in vacuum exhibit wider depletion regions and consequently lower nonlinearity compared to samples poled in air for the same time. It was speculated that $\text{H}^+/\text{H}_3\text{O}^+$ may in-diffuse from the atmosphere, while poling in air [35, 40]. LIPP measurements also showed a different charge distribution for poling in vacuum and air. A positive charge layer was revealed to be present also in the samples poled in vacuum. It was therefore thought that, in vacuum, glass ionization with liberation of e , must take place. The same phenomenon is probably occurring in air as well, but in that case in-diffusion of positive species from the atmosphere is believed to be the dominant mechanism.

Recently a study of the dynamics of thermal poling for different sample thicknesses was published, where researchers show the existence of an optimum poling time, ~10 min depending on the sample thickness, for which the achieved SON was maximized [41]. The decrease in SON for longer poling times cannot be explained by a single carrier model. In order to account for the new experimental findings new models have to be developed. In Ref. [35] two charge carriers with a very different mobility were considered. However, the same hypotheses as in Ref. [34] were used. Diffusion of ions has been considered by the authors in [42]. The models have shown good agreement with experimental results when applied to poling of a Suprasil silica glass. Other researchers have considered the ionization of the glass together with in-diffusion of H_3O^+ and H^+ from the atmosphere [43, 44]. The model predicts the existence of an *ionosphere* sandwiched between the positive charge layer and the negatively charged depletion region, in agreement with the findings of the researchers in [40].

Understanding of the physical mechanism behind the thermal poling is crucial for identification of the critical parameters affecting the process. Knowledge of this sort could lead towards engineering of the glass system and/or of the poling procedure for enhancing the induced second-order nonlinearity. However, much effort has still to be made towards the better understanding of the process. This can, for instance, be done by improving the characterization techniques and development of new methods for better accessing depletion region and obtaining information regarding its thickness, profile and dynamics.

References

- [1] Y. Fujii, B. Kawasaky, K. O. Hill, and D. C. Johnson, *Optics Letters*, vol. 5, p. 48 (1980).
- [2] Y. Sasaki and Y. Ohmori, *Applied Physics Letters*, vol. 39, p. 466 (1982).
- [3] U. Osterberg and W. Margulis, *Optics Letters*, vol. 11, p. 517 (1986).
- [4] R. H. Stolen and H. W. K. Tom, *Optics Letters*, vol. 13, p. 585 (1986).
- [5] M. C. Farries, P. St. J. Russell, M. E. Fermann, and D. N. Payne, *Electronics Letters*, vol. 23, p. 322 (1987).
- [6] E. M. Dianov, P. G. Kazansky, and D. Y. Stepanov, *Soviet Journal of Quantum Electronics*, vol. 19, p. 575 (1989).
- [7] E. M. Dianov, P. G. Kazansky, and D. Y. Stepanov, *Soviet Lightwave Communications*, vol. 1, p. 247 (1991).
- [8] E. M. Dianov, P. G. Kazansky, D. S. Starodubov, and D. Y. Stepanov, *Soviet Lightwave Communications*, vol. 2, p. 385 (1992).
- [9] E. M. Dianov, P. G. Kazansky, and D. Y. Stepanov, *Soviet Lightwave Communications*, vol. 3, p. 83 (1992).
- [10] V. Dominic and J. Feinberg, *Physical Review Letters*, vol. 73, p. 3446 (1993).

- [11] R. W. Terhune and D. A. Weinberger, *J. Opt. Soc. Am. B*, vol. 4, p. 661 (1987).
- [12] V. Mizrahi and U. Osterberg and C. Krautchik and G. E. Stegeman and J. E. Sipe and T. P. Morse, *Applied Physics Letters*, vol. 53, p. 557 (1988).
- [13] M. V. Bergot, M. C. Farries, M. E. Fermann, L. Li, L. J. Poyntz-Wright, P. St.J. Russell, and A. Smithson, *Optics Letters*, vol. 13, p. 592 (1988).
- [14] V. Mizrahi, Y. Hibino, and G. Stegeman, *Optics Communication*, vol. 78, p. 283 (1990).
- [15] A. Kamal, D. A. Weinberger, and W. H. Weber, *Optics Letters*, vol. 15, p. 613, (1990).
- [16] D. Anderson, V. Mizrahi, and J. E. Sipe, *Optics Letters*, vol. 16, p. 796, (1991).
- [17] D. M. Krol, D. J. DiGiovanni, W. Pleibel, and R. H. Stolen, *Optics Letters*, vol. 18, p. 1220, (1993).
- [18] R. A. Myers, N. Mukherjee, and S. R. J. Brueck, *Optics Letters*, vol. 16, p. 1732 (1991).
- [19] P. Butcher and D. Cotter, *The elements of nonlinear optics. Cambridge Uni. Press, 1990.*
- [20] R. Adair, L. L. Chase, and S. A. Payne, *J. Opt. Soc. Am. B*, vol. 4, p. 875 (1987).
- [21] T. G. Alley, S. R. J. Brueck, and R. A. Myers, *Journal of Non-Crystalline Solids*, vol. 242, pp. 165 (1998).
- [22] Y. Quiquempois, N. Godbout, and S. Lacroix, *Physical Review A*, vol. 65, p. 043816 (2002).
- [23] K. Hagimoto and A. Mito, *Applied Optics*, vol. 34, no. 36, pp. 8276 (1995).
- [24] K. D. Singer, J. E. Sohn, and S. J. Lalama, *Applied Physics Letters*, vol. 49, p. 248, (1986).
- [25] J. Zyss, ed., *Molecular Nonlinear Optics. Material Physics and Devices. Quantum Electronics - Principles and Applications, Academic Press Inc., 1994.*
- [26] D. E. Carlson, *Journal of the American Ceramic Society*, vol. 57, no. 7, p. 291 (1974).
- [27] N. Mukherjee, R. A. Myers, and S. R. J. Brueck, *J. Opt. Soc. Am. B*, vol. 11, no. 4, pp. 665 (1994).
- [28] P. G. Kazansky and P. St. J. Russell, *Optics Communication*, vol. 110, pp. 611 (1994).
- [29] R. Kashyap, G. J. Veldhuis, D. C. Rogers, and P. F. Mckee, *Applied Physics Letters*, vol. 64, no. 11, pp. 1332 (1994).
- [30]

- [31] T. G. Alley, S. R. J. Brueck, and M. Wiedenbeck, *J. of Applied Physics*, vol. 86, no. 12, pp. 6634 (1999).
- [32] P. G. Kazansky, A. R. Smith, and P. St. J. Russell, *Applied Physics Letters*, vol. 68, no. 2, pp. 269 (1996).
- [33] F. C. Garcia, I. C. S. Carvalho, W. Margulis, and B. Lesche, *Applied Physics Letters*, vol. 72, no. 25, pp. 3252 (1998).
- [34] B. Lesche, F. C. Garcia, E. N. Hering, W. Margulis, I. C. S. Carvalho, and F. Laurell, *Physical Review Letters*, vol. 78, no. 11, pp. 2172 (1997).
- [35] A. Von Hippel, E. P. Gross, J. G. Jelatis, and M. Geller, *Physical Review*, vol. 91, no. 3, pp. 568 (1953).
- [36] T. G. Alley, S. R. J. Brueck, and R. A. Myers, *Journal of Non-Crystalline Solids*, vol. 242, pp. 165 (1998).
- [37] Y. Quiquempois, G. Martinelli, P. Duth_era, P. Bernage, P. Niay, and M. Douay, *Optics Communications*, vol. 176, pp. 479 (2000).
- [38] A. Kameyama, A. Yokotani, and K. Kurosawa, *Journal of Applied Physics*, vol. 89, no. 9, pp. 4707 (2001).
- [39] T. M. Proctor and P. M. Sutton, *Journal of Chemical Physics*, vol. 30, no. 1, pp. 212 (1959).
- [40] Y. Quiquempois, N. Godbout, and S. Lacroix, *Physical Review A*, vol. 65, p. 043816 (2002).
- [41] V. Pruneri, F. Samoggia, G. Bonfrate, P. G. Kazansky, and G. M. Yang, *Applied Physics Letters*, vol. 74, no. 17, pp. 2423 (1999).
- [42] D. Faccio, V. Pruneri, and P. G. Kazansky, *Applied Physics Letters*, vol. 79, no. 17, pp. 2687 (2001).
- [43] N. Godbout and S. Lacroix, *Journal of Non-Crystalline Solids*, vol. 316, pp. 338 (2003).
- [44] X.-M. Liu, H.-Y. Zhang, Y.-L. Guo, X.-P. Zheng, and Y. Li, *Japanese Journal of Applied Physics*, vol. 40, pp. L807 (2001).
- [45] X.-M. Liu and M.-D. Zhang, *Japanese Journal of Applied Physics*, vol. 40, pp. 4069 (2001).

Appendix B: On the evolution of EFAD

This appendix is devoted to the importance of providing a good contact between the electrodes and samples and its role in evolution of the EFAD process. Essentially, in the context of the evolution of the EFAD process, the role of the glass-electrode contact can be considered if we recall that electrons tunnelling from ionised clusters have to be extracted at the anode. In order to gain a qualitative picture the following experiment was conducted. A 1mm thick polydisperse-type I-sample was equipped with two flat contact steel electrodes (6mm×9mm) so that the positive electrode was facing the nanoparticles containing layer. The sample was then placed inside the oven, and as explained in detail in 4.2, was subjected to the following treatment steps at ~280°C: 200 V -10 min (a), 200 V - 10 min (b); 200 V - 20 min (c); 200 V - 40 min (d); 400 V - 10 min (e); 600 V - 10 min (f) and 800 V - 10 min (h). Between each step of treatment, microscopic images of the sample were recorder. The results are shown in Fig. B-1.

As it can be seen, for treatment at 280°C, bleaching occurred with voltage as low as 0.2kV but did not cover the entire electrode area (Fig. B-1 a-d). Bleaching started in a central zone which covered approximately 13% of the total electrode area after 10min of treatment. It has to be pointed out that this zone was extended only slightly with increasing of the treatment time. After 10min treatment steps at 0.4kV (Fig. B-1 e) bleaching started near the electrode edges as well. However, it was only a treatment steps at 0.6kV and 0.8kV that the bleached zones in the middle and near the edges started to merge progressively (Fig. B-1 f and h, respectively). Finally, after 15min treatment step at 1kV, the entire area underneath the electrode was bleached (not shown here but for comparison see Fig. 4.7).

Mechanically contacted electrodes did not obviously provide a perfect uniform contact with the sample surface over the entire electrode area and the bleached zones were, hence, associated with tight contact. An evidence of this effect was found when the sample was probed in reflection from cathode side just after the poling step at 0.6kV while the anode stuck on glass surface due to electrostatic forces (Fig. B-1 g). Areas where tight contact was achieved were corresponded to bleached zones.

The present results show that physical contact (rather than ionised species from atmosphere [1]) is needed to extract electrons efficiently. The electrostatic force exerted on the sample is further enhanced due to ion migration during the treatment. This can be qualitatively estimated as the electrostatic force between two plane electrodes is given by:

$$F = 0.5\epsilon_0\epsilon_r^2SV^2L^{-2}, \quad (\text{B-1})$$

where S is the electrode surface, V is the applied voltage, L is the distance between electrodes and ϵ_r is the relative permittivity of glass sample sandwiched between the electrodes. When 1kV is applied to our sample at room temperature, the electrostatic force is as weak as $F=1.2\times 10^{-3}\text{N}$ (taking $S=54\text{mm}^2$, $L=1\text{mm}$ and $\epsilon_r=2.2$). At elevated temperatures, however, the applied voltage drops almost entirely across the ion-depleted layer [1]. This results in much stronger electrostatic force due to the decrease of the effective distance between the electrodes.

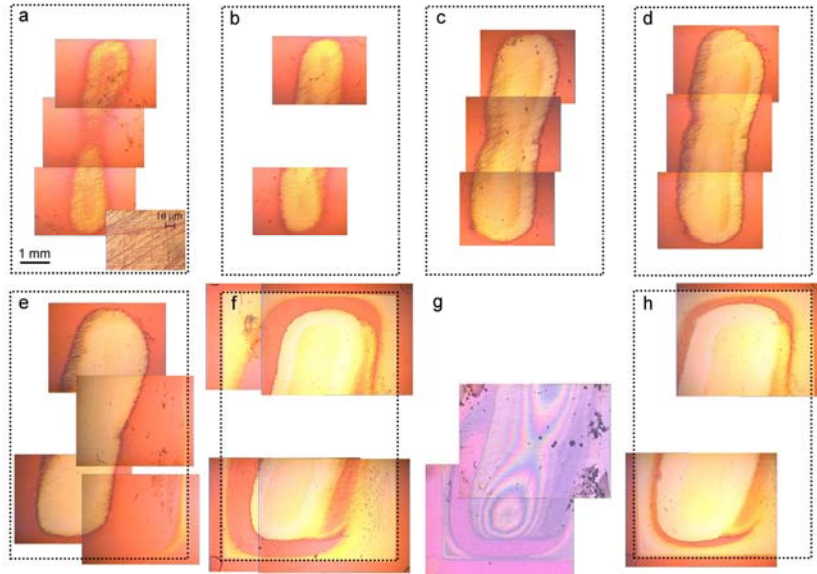


Figure B-1: Microscope images (in transmission) of the surface of the sample after successive treatment steps at $\sim 280^\circ\text{C}$ in the following sequence: 200 V -10 min (a), 200 V - 10 min (b); 200 V - 20 min (c); 200 V - 40 min (d); 400 V - 10 min (e); 600 V - 10 min (f) and 800 V - 10 min (h). Dotted rectangles represent the electrode ($6\times 9\text{mm}^2$). Zones where embedded silver nanoparticles have been dissolved appeared yellowish in the images. Microscope image (in reflection) taken from sample's cathode side while the anode stuck on glass surface is also shown (g). Images (a-h) were taken using $2\times$ objective. Zoomed inset image in (a) was taken using a $50\times$ objective.

An important point to consider is that for the experiments presented in the main body of the thesis flat *press* contact steel electrodes were used. While these electrodes considerably improve the homogeneity of the contact between the electrode and glass, but the overall contact is still far from perfect, as some jumps in the current evolutions were indicated (See for examples Fig. 4.12). The contact can be further improved by using a carbon ink layer between the electrodes and glass. However for the experiments described in the thesis this technique was not applied.

Reference

- [1] P. B. Johnson and R. W. Christy, *Physical Review B* **6**, 4370 (1972).

Curriculum Vitae of Amin Abdolvand

Brief Biography

Amin was born in Shiraz, Iran, on 14 April 1973. In 1993, he moved to Minsk, Belarus, for study. Since 1999, he holds a Diploma in Optical engineering and a MSc in engineering both from the Instrument making faculty, Belarus National Technical University (BNTU),¹ Minsk, Belarus, for investigation of spectroscopic and laser characteristics of rare-earth ions (Yb^{3+} , Ho^{3+} and Tm^{3+}) in new laser crystals: Yb, Ho: KGW and Yb, Tm: KGW, and demonstration of CW, passive Q-switching and self-frequency Raman conversion in Ytterbium-doped KGW, respectively. Both investigations were conducted under the supervision of Prof. Dr. N.V. Kuleshov at the International Laser Centre (ILC)², BNTU. The latter work led to the successful demonstrations of passive mode locking as well as thin disk laser operations on Yb-doped KGW and KYW crystals, while he was working as a researcher at the ILC.

From 2000 to 2003 he worked at the Optoelectronics Research Centre,³ University of Southampton,⁴ England, where he held a research scholarship provided by the Southampton University. In 2004 he was awarded an MPhil degree in fibre lasers from the University of Southampton for work on High-power two-micron fibre bulk hybrid lasers with Prof. Dr. W. A. Clarkson. As a part of this study he developed an ultra-efficient Ho:YAG laser end-pumped by a high-power tunable Tm-doped silica fibre laser.

Since fall 2003 he has been at the Department of Physics, Martin-Luther University Halle-Wittenberg,⁵ Germany, conducting research on modification of optical and structural properties of metallic nanoparticles embedded in various matrices using different techniques, from ultra-short laser pulses to DC electric field. In January 2006 he was awarded a Dr. rer. nat. degree in Physics for work on modification of optical and structural properties of glass containing silver nanoparticles via DC electric field and moderately elevated temperatures with Prof. Dr. H. Graener.

¹ Formerly called “Belarussian State Polytechnic Academy”. www.bntu.by

² www.ilc.by

³ www.orc.soton.ac.uk

⁴ www.soton.ac.uk

⁵ www.uni-halle.de

Publications in peer-reviewed journals and proceedings

1. **Metallo-dielectric 2D photonic structures made by DC electric field microstructuring of nanocomposite glasses**, A. Abdolvand, A. Podlipensky, S. Matthias, F. Syrowatka, U. Gösele, G. Seifert, H. Graener, *Advanced Materials*, vol.17(24), pp.2983-2987 (2005). Selected as cover picture.
2. **Modeling of the optical properties of silver-doped nanocomposite glass modified by electric field assisted dissolution of nanoparticles**, J. Sancho-Paramon, A. Abdolvand, A. Podlipensky, F. Syrowatka, G. Seifert, H. Graener, *Submitted* (2005).
3. **Effective medium models for metal-dielectric composites: an analysis based on the spectral density theory**, J. Sancho-Paramon, S. Bosch, A. Abdolvand, A. Podlipensky, G. Seifert, H. Graener, *Proceedings of SPIE Vol. 5963, p. 556-566 "Advances in Optical Thin Films II"; Claude Amra, Norbert Kaiser, H. Angus MacLeod, Eds. (2005).*
4. **Electric field-assisted formation of percolated silver nanolayers inside glass**, A. Abdolvand, A. Podlipensky, G. Seifert, H. Graener, O. Deparis, P. G. Kazansky, *Optics Express*, vol. 13(4), pp.1266-1274 (2005).
5. **Evolution of poling-assisted bleaching of metal-doped nanocomposite glass with poling conditions**, O. Deparis, P. G. Kazansky, A. Abdolvand, A. Podlipensky, G. Seifert, H. Graener, *Applied Physics Letters* vol. 86, 261109 (2005).
6. **Generation of wavelength-dependent, periodic line pattern in metal nanoparticle-containing polymer films by femtosecond laser irradiation**, A. Kiesow, S. Strohark, K. Löschner, A. Heilmann, A. Podlipensky, A. Abdolvand, G. Seifert, *Applied Physics Letters* vol. 86, 153111 (2005).
7. **Femtosecond laser assisted production of dichroitic 3D structures in composite glass containing Ag nanoparticles**, A. Podlipensky, A. Abdolvand, G. Seifert, H. Graener, *Applied Physics A*, vol. 80, pp. 1647 (2005).
8. **Production of 3D, dichroitic microstructures in nanocomposite glasses by femtosecond laser pulses**, G. Seifert, A. Podlipensky, A. Abdolvand, J. Lange, H. Graener, *Springer Series in Chemical Physics, Ultrafast Phenomena XIV, Eds.: T. Kobayashi, T. Okada, T. Kobayashi, K. Nelson, S. De Silvestri, pp.810 (Springer-Berlin 2005).*
9. **Dissolution of silver nanoparticles in glass through an intense DC electric field**, A. Podlipensky, A. Abdolvand, G. Seifert, H. Graener, O. Deparis, P. G. Kazansky, *Journal of Physical Chemistry B*, vol. 108(46), pp. 17699-17703(2004).
10. **Novel technique for engineering the structural and optical properties of metal-doped nanocomposite glasses**, O. Deparis, P. G. Kazansky, A. Abdolvand, A. Podlipensky, G. Seifert and H. Graener, *Proceedings of Symposium IEEE/LEOS/Benelux Chapter, S04P033, pp. 33-36 (2004).*
11. **Poling-assisted bleaching of metal-doped nanocomposite glass**, O. Deparis, P. G. Kazansky, A. Abdolvand, A. Podlipensky, G. Seifert, H. Graener, *Applied Physics Letters*, vol. 85(6), pp. 872-875 (2004).
12. **Efficient Ho:YAG laser pumped by a cladding-pumped tunable Tm:silica fiber laser**, D.Y. Shen, A. Abdolvand, L. J. Cooper and W.A. Clarkson, *Applied Physics B*, vol. 79(5), pp. 559-562 (2004).
13. **Passively Q-switched Er-Yb double clad fiber laser with Cr²⁺:ZnSe and Co²⁺:MgAl₂O₄ as a saturable absorber**, V. Philippov, A. Abdolvand, J. Nilsson, W.A. Clarkson, V.E. Kisel, V.G. Shcherbitsky, N.V. Kuleshov, V.I. Konstantinov, V.I. Levchenko, *SPIE Proceedings (Photonics West)*, vol. 5335-04 (2004).

14. **Ultra-efficient Ho:YAG laser end-pumped by a cladding-pumped Tm-doped silica fibre laser**, A. Abdolvand, D. Y. Shen, L. J. Cooper, R. B. Williams and W. A. Clarkson, *OSA Trends in Optics & Photonics*, vol. 83, pp.7-11 (2003).
15. **High power two-micron fiber lasers**, W.A. Clarkson, A. Abdolvand, D.Y. Shen, R.B. Hayward, L.J. Cooper, R.B. Williams and J. Nilsson, *SPIE Proceedings on Gas, Chemical Lasers & High Power Lasers*, vol. 5120, pp.482-489 (2003). *Invited.*
16. **High power Yb:KGW and Yb:KYW thin disk laser operation**, S. Erhard, J. Gao, A. Giesen, K. Contag, A.A. Lagatsky, A. Abdolvand, N.V. Kuleshov, J. Aus der Au, G.J. Spuhler, F. Brunner, R. Paschotta, U. Keller, *OSA Trends in Optics & Photonics*, vol. 56, pp. 333-336 (2001).
17. **Thin Disk Laser Operation and Spectroscopic Characterization of Yb-doped Sesquioxides and Potassium Tungstates**, M. Larionov, J. Gao, S. Erhard, A. Giesen, K. Contag, V. Peters, E. Mix, L. Fornasiero, K. Petermann, G. Huber, J. Aus der Au, G.J. Spühler, F. Brunner, R. Paschotta, U. Keller, A. A. Lagatsky, A. Abdolvand, N. V. Kuleshov, *OSA Trends in Optics and Photonics*, vol. 50, pp. 625-628 (2001).
18. **Passive Q-switching and self-frequency Raman conversion in diode-pumped Yb:KGd(WO₄)₂ laser**, A.A. Lagatsky, A. Abdolvand, N.V. Kuleshov, *Optics Letters*, vol.25 (9), pp.616-619 (2000).
19. **Diode-pumped femtosecond Yb:KGd(WO₄)₂ laser with 1.1 W average power**, F. Brunner, G.J. Spühler, J. Aus der Au, L. Krainer, F. Morier-Genoud, R. Paschotta, N. Lichtenstein, S. Weiss, C. Harder, A.A. Lagatsky, A. Abdolvand, N.V. Kuleshov, and U. Keller, *Optics Letters*, vol. 25(15), pp.1119-1121 (2000).
20. **Diode-pumped passively Q-switched Yb:KGW laser**, A. Lagatsky, A. Abdolvand, N.V. Kuleshov, *OSA Trends in Optics and Photonics*, vol. 43, pp.116-119 (2000).

Conference papers including invited and post-deadline talks

21. **Submicron, 2D, photonic structuring in metal-doped nanocomposite glass**, A. Abdolvand, A. Podlipensky, G. Seifert, F. Syrowatka, S. Matthias, H. Graener, *International Conference on Coherent and Nonlinear Optics ICONO/LAT, May 11-15 St. Petersburg/Russia (2005), ISK7. Postdeadline.*
22. **A new age for poling: The modification of optical properties of metal-glass nanocomposites**, O. Deparis, P. G. Kazansky, A. Abdolvand, A. Podlipensky, G. Seifert, H. Graener, *Conference of Bragg Gratings, Photosensitivity and Poling in Glass Waveguides (BGPP), July 4-9, Sydney/ Australia, CD-ROM, pp. 183-185 (2005).*
23. **Refractive index engineering in glass containing spherical silver nanoparticles using DC electric field**, A. Abdolvand, A. Podlipensky, G. Seifert, O. Deparis, P. G. Kazansky, H.Graener, *Conference on Lasers and Electro-Optics(CLEO)/Europe-EQEC/Munich/Germany, June 12-17 (2005), CE3-1.*
24. **Induced dichroism in soda-lime glass with spherical Ag nanoparticles via fs laser irradiation**, A. Podlipensky, A. Abdolvand, G. Seifert, H. Graener, *Conference on Lasers and Electro-Optics(CLEO)/Europe-EQEC/Munich/Germany, June 12-17 (2005), CE3-2.*
25. **Fine optical structuring in glass with embedded elliptical silver nanoparticles using dc electric field**, A. Abdolvand, A. Podlipensky, G. Seifert, H. Graener, *Conference on Lasers and Electro-Optics(CLEO)/Europe-EQEC/Munich/Germany, June 12-17 (2005), EI-2.*
26. **Anisotropic shape modification of Ag nanoparticles in glass by fs laser pulses: Effect of pulse intensity, wavelength and temperature**, A. Podlipensky, A. Abdolvand, G. Seifert, H. Graener, *International Conference on Coherent and Nonlinear Optics ICONO/LAT, May 11-15 St. Petersburg/Russia (2005), IWC3.*

27. **DC electric field-assisted dissolution of embedded silver nanoparticles in glass matrix: The phenomenon and its Application**, A. Abdolvand, A. Podlipensky, G. Seifert, O. Deparis, P. G. Kazansky, H. Graener, *International Conference on Coherent and Nonlinear Optics ICONO/LAT, May 11-15 St. Petersburg/Russia (2005), IThR5*.
28. **Wood's structures created in composite glass with Ag nanoparticles upon ns laser irradiation**, A. Podlipensky, A. Abdolvand, G. Seifert, H. Graener, *International Conference on Coherent and Nonlinear Optics ICONO/LAT, May 11-15 St. Petersburg/Russia (2005), IWK4*.
29. **Structuring of glass nanocomposites by DC electric field assisted dissolution of metal nanoparticles**, A. Abdolvand, A. Podlipensky, G. Seifert, H. Graener, *Innovation Forum Structuring of Glasses, February 14-15, Magdeburg/Germany (2005). Invited*
30. **Variable production of optical microstructures with femtosecond laser pulse signals in glass with nanoparticles**, A. Podlipensky, A. Abdolvand, G. Seifert, H. Graener, *Innovation Forum Structuring of Glasses, February 14-15, Magdeburg/Germany (2005). Invited*
31. **Micron and submicron structuring in silver-doped nanocomposite glass using DC electric field**, A. Abdolvand, A. Podlipensky, G. Seifert, S. Matthias, U. Gösele, H. Graener, *Innovation Forum Structuring of Glasses, February 14-15, Magdeburg/Germany (2005). Selected Poster*
32. **Mikro- und Nanostrukturierung der optischen Eigenschaften von metallpartikel-haltigen Gläsern**, G. Seifert, A. Podlipensky, A. Abdolvand, H. Graener, *Frühjahrstagung der Deutschen Physikalischen Gesellschaft, Verhandlungen DPG 69, DY 36.3 (2005)*.
33. **Laser-induced periodic structures in plasma polymer films with embedded metal nanoparticles**, K. Löschner, A. Kisow, A. Heilmann, A. Abdolvand, G. Seifert, *Frühjahrstagung der Deutschen Physikalischen Gesellschaft, Verhandlungen DPG 69, DS 24.23 (2005)*.
34. **Towards metallic microstructuring in nanocomposite glass**, A. Abdolvand, A. Podlipensky, G. Seifert, O. Deparis, P. G. Kazansky, and H. Graener, *Roman Baths Summer School on Advanced Glass-Based Nano-Photonics, July 12-16, Bath/United Kingdom (2004)*.
35. **Modification of optical properties of glass containing silver nanoparticles upon nanosecond laser irradiation**, A. Abdolvand, A. Podlipensky, G. Seifert, H. Graener, *10th International Microoptics Conference (MOC'04), L-37, September 1-3, Jena/Germany (2004)*.
36. **Femtosecond laser assisted rewriting 3D data storage in composite glass with Ag nanoparticles**, A. Podlipensky, A. Abdolvand, G. Seifert, H. Graener, *Roman Baths Summer School on Advanced Glass-Based Nano-Photonics, July 12-16, Bath/United Kingdom (2004)*.
37. **Rewriting 3D storage using fs laser induced modification of spherical Ag nanoparticles in glass**, A. Podlipensky, A. Abdolvand, G. Seifert, H. Graener, *Conference on Lasers and Electro-Optics(CLEO)/America, San Francisco/USA, Paper: CTuP55 (2004)*.
38. **Composite glass with elongated Ag nanoparticles as a nonlinear media for SHG**, A. Podlipensky, A. Abdolvand, J. Lange, G. Seifert, H. Graener, *10th International Microoptics Conference (MOC'04), L-36, September 1-3, Jena/Germany (2004)*.
39. **Line pattern in plasma polymer films with embedded gold and silver nanoparticles by irradiation with ultrashort laser pulses**, A. Kiesow, S. Strohark, K. Löschner, A. Heilmann, A. Podlipensky, A. Abdolvand, G. Seifert and H. Graener, *in Nanoparticles and Nanowire Building Blocks-Synthesis, Processing, Characterization and Theory, edited by Orest J. Glembocki and Charles E. Hunt (Mater. Res. Soc. Symp. Proc. 818, Warrendale, PA, 2004) M12.17*.
40. **Periodic structures in polymer thin film with embedded metal nanoparticles**, A. Kiesow, S. Strohark, K. Löschner, A. Heilmann, A. Podlipensky, A. Abdolvand, G. Seifert, H. Graener, *Conference on nanometer scale science and technology (NANO-8), NS3-WeA7, Venice/Italy (2004). Invited*

41. **Production of 3D, dichroitic microstructures in nanocomposite glasses by femtosecond laser pulses**, G. Seifert, A. Podlipensky, A. Abdolvand, J. Lange and H. Graener, *14th International Conference on Ultrafast Phenomena, Niigata/Japan, Paper: TuD5 (2004)*.
42. **Anisotropic optical properties of laser-treated polymer films with embedded metallic nanoparticles**, A. Kiesow, S. Strohkark, K. Löschner, A. Heilmann, A. Podlipensky, A. Abdolvand, G. Seifert, H. Graener, *7th International Conference on Nanostructured Materials (NANO 2004), Wiesbaden/Germany (2004)*.
43. **Passively Q-switched Tm-doped silica fiber laser**, J. K. Sahu, V. Philippov, J. Kim, C. Codemard, P. Dupriez, J. Nilsson, A. Abdolvand, N. V. Kuleshov, *Conference on Lasers and Electro-Optics(CLEO)/America, San Francisco/USA, Paper: CThGG (2004)*.
44. **High-power two-micron fiber-bulk hybrid laser**, A. Abdolvand, **MPhil Thesis, University of Southampton, England (2004)**.
45. **Highly efficient Ho:YAG laser pumped by a Tm-doped silica fibre laser**, A. Abdolvand, D.Y. Shen, L. J. Cooper, R.B. Williams and W.A. Clarkson, *Conference on Lasers and Electro-Optics(CLEO)/America, Maryland/USA, Paper: CThM38 (2003)*.
46. **Power scaling of cladding-pumped Tm-doped silica fibre lasers**, W.A. Clarkson, A. Abdolvand, V. Matera, T.M.J. Kendall, J. Nilsson, P.W. Turner and D.C. Hanna, *Conference on Lasers and Electro-Optics(CLEO)/Europe-EQEC/Munich/Germany, pp.141 (2001)*.
47. **High-power wavelength-combined cladding-pumped Tm-doped silica fibre lasers**, W.A. Clarkson, V. Matera, A. Abdolvand, T.M.J. Kendall, J. Nilsson, P.W. Turner, D.C. Hanna, *OSA TOPS, vol. 56, CWM2 (2001)*.
48. **Spectral beam combining of cladding-pumped Tm-doped silica fibre lasers**, W.A. Clarkson, A. Abdolvand, V. Matera, T.M.J. Kendall, D.C. Hanna, J. Nilsson and P.W. Turner, *Quantum Electronics & Photonics Conference(QEP-15)/Glasgow/UK, pp.13 (2001)*.
49. **High Power Yb:KGW and Yb:KYW Thin Disk Laser Operation**, S.Erhard, J.Gao, A.Giesen, K.Contag, A.A. Lagatsky, A. Abdolvand, N.V. Kuleshov, F. Brunner, J. Aus der Au , G.J. Spühler, R. Paschotta, U. Keller, *Conference on Lasers and Electro-Optics(CLEO)/America, Paper:CWF2 (2001)*.
50. **Tunable diode-pumped CW lasing of Yb:KGW and Yb:KYW: modeling and experiment**, A. Abdolvand, A.A. Lagatsky, N.V. Kuleshov, *First International Conference on Laser Optics for Young Scientists/St. Peterburg/Russia, pp. 120 (2000)*.
51. **Diode-pumped passively Q-switched Yb:KGW laser with V:YAG saturable absorber**, A. Lagatsky, A. Abdolvand, N.V. Kuleshov, *Conference on Lasers and Electro-Optics(CLEO)/Europe/Munich/Germany, Paper: CTuK36 (2000)*.
52. **1.1-W femtosecond diode-pumped Yb:KGD(WO₄)₂ laser**, F. Brunner, J. Aus der Au , G.J. Spühler, , L. Krainer, R. Paschotta, F. Morier-Genoud, U. Keller, N. Lichtenstein, S. Weiss, C. Harder, A. Lagatsky, A. Abdolvand, and N.V. Kuleshov, *Conference on Lasers and Electro-Optics(CLEO) /Europe/Munich/Germany, Paper: CMA2 (2000)*.
53. **Diode-pumped, passively Q-switched, self-frequency Raman converted Yb:KGW laser**, A. Lagatsky, A. Abdolvand, N.V. Kuleshov, *X Conference on Laser Optics/St. Peterburg/Russia, pp. 98 (2000)*.

Patent

"Verfahren zur Auflösung von Metallnanopartikeln in Dielektrika durch Einwirkung eines elektrischen Gleichfeldes", Patentanmeldung 10 2004 018 908 0, Anmeldetag 15.04.2004.

Acknowledgements

First of all, I would like to give my deepest possible acknowledgement to Professor Dr. Heinrich Graener, dean of the Physics Department, who also enthusiastically leads our group “Optics Group”. I thank you for giving me the opportunity to carry on this research and for your interest, ideas, enthusiasm and vital encouragement.

I must express my deepest gratitude to Priv.-Doz. Dr. Gerhard Seifert for support, encouragement and for providing me with freedom in research. I am also indebted to him for seeking financial support for this research, supporting official trips, and for arranging additional financial support for me while I was waiting for my degree from Southampton.

I would like to express my thanks to my best friend and colleague, Dr. Alexander Podlipensky, whom I know for many years now, and with whom I have worked once again in my life especially closely on another successful research project.

Many thanks are due to Dr. Jordi Sancho-Paramon for fruitful discussions on many aspects of the work and in particular on the rainbow effect.

Thanks must go to other staff of the optics group, especially Dr. Jens Lange for the technical support, and Frau Otten for help in preparing the samples. I am very grateful to them both.

Sincere thanks are due to Professor Dr. Peter G. Kazansky of Optoelectronics Research Centre, Southampton University, England, and Dr. Olivier Deparis of Faculté Polytechnique de Mons, Belgium, for fruitful co-operation at various aspects of the work, particularly measurements on dynamics. Especially I am very grateful to Peter for listening to some of the ideas and letting me to use his poling laboratory at the Southampton University.

Thanks must also go to Dr. G. Heine and Dip.Phys. A. Volke of CODIXX AG-Barleben, Germany, for providing polydisperse samples, and Dr. K.-J. Berg of MLU for providing monodisperse sample used for the studies, to Dip.Phys. F. Syrowatka of IWZ Materialwissenschaft, MLU-Halle, for help with the scanning electron microscopy (SEM) and to Dr. H. Hofmeister of Max Planck Institute of Microstructure Physics-Halle, for the transmission electron microscopy (TEM) pictures. Sincere thanks are due to Dr. Sven Matthias of Max Planck Institute of Microstructure Physics-Halle, for providing macroporous and nanoporous silicones used for structuring experiments and to workshop of the MLU for technical support.

Diverging from the technical path, I wish to express my gratefulness to those loved ones and close friends who were always there for me. Especially I would like to thank my wife, Natalie, and my daughter, Diana, for their love, support and encouragement.

Erklärung

Hiermit erkläre ich, daß ich diese Arbeit selbständig und ohne fremde Hilfe verfaßt, andere als die von mir angegebenen Quellen und Hilfsmittel nicht benutzt und die den benutzen Werken wörtlich oder inhaltlich entnommenen Stellen als solche kenntlich gemacht habe.

Amin Abdolvand.